GAS KINETIC STUDY OF MAGNETIC FIELD EFFECTS ON PLASMA PLUMES

A Thesis

by

FRANS HENDRIK EBERSOHN

Submitted to the Office of Graduate Studies of
Texas A&M University
in partial fulfillment of the requirements for the degree of

MASTER OF SCIENCE

Approved by:

Co-Chairs of Committee,	Sharath S. Girimaji
	David Staack
Committee Members,	Jacques Richard
	John V. Shebalin
Department Head,	Rodney Bowersox

December 2012

Major Subject: Aerospace Engineering

ABSTRACT

Plasma flow physics in magnetic nozzles must be clearly understood for optimal design of plasma propulsion devices. Toward that end, in this thesis we: i) perform an extensive literature survey of magnetic nozzle physics, ii) assess the validity of magnetohydrodynamics for studying magnetic nozzle physics, and iii) illustrate the effects of the Hall term in simple flows as well as in magnetic nozzle configurations through numerical experiments with the Magneto-Gas Kinetic Method (MGKM).

The crucial steps necessary for thrust generation in magnetic nozzles are energy conversion, plasma detachment, and momentum transfer. These three physical phenomena must be understood to optimize magnetic nozzle design. The operating dimensionless parameter ranges of six prominent experiments are considered and the corresponding mechanisms are discussed.

An order of magnitude analysis of the governing equations reveal: i) most magnetic nozzles under consideration operate at the edge of the continuum regime rendering continuum-based description and computation valid; ii) in the context of MHD framework, the generalized Ohm's law must be used to capture all of the relevant physics.

This work also continues the development of the Magneto Gas Kinetic Method (MGKM) computational tool. Validation of the solver is performed in shock-tube and Hartmann channel flows in the Hall physics regime. Comparison with theory and available data is made whenever possible.

Novel numerical experiments of magnetic nozzle plasma jets in the Hall regime are performed, confirming the theoretically predicted azimuthal rotation of the plasma jet due to Hall physics. The primary conclusion from this work is that the addi-

tion of the Hall effect generates helical structures in magnetic nozzle plasma flows. Preliminary results are encouraging for future magnetic nozzle studies and further challenges are identified.

DEDICATION

Ek toewy die tesis aan my familie, die Ebersohns en die Manse. Dankie vir al julle ondersteuning deur al die jare, sonner julle kon ek nie die werk doen nie.

ACKNOWLEDGEMENTS

I would like begin by thanking the members of my committee for their guidance and support. The first of these is Dr. Sharath Girimaji who was my advisor and the chair of my committee. His understanding of fluid dynamics and computational methods have been invaluable to this research. I have learned a great deal from him about both physics and being an engineer. I would also like to thank Dr. David Staack the co-chair of my committee from who I learned a great deal about the field of plasma physics. He provided a needed experimental perspective to my research and gave valuable research input and advice. I would also like to thank Dr. Jacques Richard for introducing me to the great fields of space propulsion and plasma physics and for his encouragement and guidance through the years. Lastly I would like to thank Dr. John Shebalin for becoming my mentor at NASA. I have not only learned a great deal about the field of plasma physics from him, but have also been taught about what to expect in the future of my career. He has given me extensive insight into what it takes to become an effective researcher and has illuminated the path for me to achieve this. My research would not have been possible without my committee and I strive to one day become experts in the field like them.

Next I would like to thank my family and friends for their support through all the years. I would like to thank my parents George and Karin Ebersohn who have enabled everything in my life through their selflessness and sacrifices. I would also like to thank my brother Abram Ebersohn for being my companion through all these years and those to come. I am also thankful to Margeaux Horne for her help in editing this manuscript, preparing my defense, and her support through the last few years. Finally I would like to thank all my other friends and family for their support.

This thesis and any success I have is a reflection of the support I get from my friends and family, and I am truly thankful.

I would also like to thank Ad Astra Rocket company for their collaboration with this research. I would especially like to thank Benjamin Longmier and Chris Olsen for the fruitful discussions on magnetic nozzle physics.

The last group I would like to thank are the fellow students in our research group. First I would like to thank Daniel Araya for our discussions on magnetohydrodynamics and his development of the numerical solver. I also want to thank Gaurav Kumar for his guidance in understanding the Gas Kinetic Method and helping me when I was lost in the theory. Jacob Cooper also deserves thanks for his helpful discussion on fluid dynamics and for being a great office-mate. Finally I would like to thank the rest of the Turbulence Research group for their help and support.

I would also like to thank the administrative people in the Aerospace Engineering department. Particularly I would like to thank Colleen Leatherman and Karen Knabe for helping me organize travel and guiding me through the graduation process.

Lastly, I would like to thank NASA for funding this research through a NASA Space Technology Research Fellowship with grant number NNX11AM98H. I would also like to thank the Texas A&M University Office of Graduate Studies for partially funding my Master's education.

NOMENCLATURE

ρ	Density
n	Number density
T	Temperature
p	Pressure
U	Center of mass velocity, potential energy
u	Macroscopic velocity
v	Velocity or kinetic velocity
m, M	Mass
e	Energy
J	Current density
B	Magnetic field
E	Electric field
Φ	Electric potential
r	Radius
λ	Mean free path
ω	Frequency
τ_{col}	Collision time
q	Charge
ν	Collision frequency
k	Boltzmann constant
μ_0	Permeability of free space
ϵ_0	Permitivity of free space
Ψ	Macroscopic variables

Subscripts

$\perp$	Perpendicular to magnetic field
$\parallel$	Parallel to magnetic field
0	Initial
I	Ion
E	Electric
e	Electron
H	Hydrodynamic (flow+internal)
p	Plasma or propellant
f	Flow characteristic
c	Cyclotron
k	Kinetic
ex	Exit
d	Delivered
D	Debye
n	Neutral
m	Magnetic
i, j, k	Indices
σ	Species

TABLE OF CONTENTS

LIST OF FIGURES

LIST OF TABLES

1. INTRODUCTION

1.1 Overview of Space Propulsion

Thus far the exploration of space has been driven primarily by the desire to learn more about the universe and stretch the reach of man incrementally further. The technology and scientific insight gained from these endeavors are numerous and essential to the modern world. Exploration is initially driven by curiosity and transitions into socioeconomic expansion.

The means by which we travel through space must be developed to advance space exploration. Among the current limitations of space travel are the time length of missions, the technology to keep man alive in space, and the cost of missions. Space propulsion methods are a key enabling technology which strive to eliminate these limitations. Developing propulsion technology can increase thrust and efficiency which decrease transit time, increase payload mass, and decrease mission cost. Space propulsion is therefore a crucial technology that can alleviate the design constraints of other technologies. Improving propulsion methods will also enable faster and further travel. NASA has defined efficient in-space propulsion as a space technology grand challenge to illustrate its importance to future space exploration.

Propulsion methods provide the force necessary to drive spacecraft and strive to maximize efficiency in order to maximize payload, minimize travel time, and minimize cost. The force produced by the propulsion method is defined as the thrust, T, while the efficiency of propellant use is characterized by the specific impulse, I_{sp}. Specific impulse is a measure of the exit velocity of ejected particles and is defined by the relation shown in Equation 1.1 in which g_0 is the acceleration due to gravity on the Earth's surface.

$$I_{sp} = \frac{v_{ex}}{g_0} \tag{1.1}$$

The force the spacecraft experiences is equal to the mass of the spacecraft multiplied by the change in velocity, shown in Equation 1.2.

$$T = M_{spacecraft}\frac{dv}{dt} \tag{1.2}$$

This thrust force comes as a result of the ejection of particles by the spacecraft which is characterized by the exit velocity of the particles multiplied by the flow rate of particles, shown in Equation 1.3.

$$T = -v_{ex}\frac{dm_p}{dt} \tag{1.3}$$

Solving this system of ordinary differential equations leads to the rocket equation. This equation represents the total change in velocity of the spacecraft experiences during a mission (Δv) as a function of I_{sp}, the final mass (m_f), and the initial mass (m_0).

$$\Delta v = g_0(I_{sp})ln\left(\frac{m_0}{m_f}\right) \tag{1.4}$$

The total change in velocity required is a mission specific value. Equation 1.4 demonstrates that when the I_{sp} is increased the required initial mass decreases exponentially for a mission requiring a given Δv and delivered mass. This implies a significant decrease in the required propellant. This equation also demonstrates that for a given Δv and initial mass, the final mass can be increased exponentially as I_{sp} is increased. Finally for a constant initial and final mass, it can be inferred that increasing I_{sp} linearly increases Δv. Therefore increasing the specific impulse

characterizes the efficiency of propellant use and should be maximized.

1.2 Space Propulsion Methods

A list of some of the currently being considered in-space propulsion methods for near term mission use is shown below along with a brief description of each.[33]

1. *Cold gas thrusters* consist simply of a pressurized tank of gas connected to a valve and a nozzle

2. *Solar sails* accelerate the spacecraft via collisions of photons with a deployed sail

3. *Nuclear thermal propulsion* heats propellant to high temperatures by a nuclear reactor and then expands the propellant through a nozzle

4. *Chemical propulsion* heats propellant by chemical reactions and then expands the high energy fluid through a nozzle

5. *Electric propulsion* can potentially generate thrust by many means: electrically heating propellant; electrostatically accelerating charged particles; or, manipulating the flow charged particles with electromagnetic fields

Electric propulsion is the primary focus of this study and consists of the following sub-fields.

1. *Electrostatic Propulsion* accelerates charged particles with electrostatic body forces

2. *Electrothermal Propulsion* heats a propellant gas electrically and expands it through a nozzle

3. *Electromagnetic Propulsion* produces thrust through the interaction of electromagnetic fields and an ionized propellant

Electrostatic propulsion devices include Hall thrusters and ion thrusters. Electrothermal propulsion devices include resistojets and arcjets. Finally, electromagnetic propulsion devices include magnetoplasmadynamic (MPD) thrusters and the VAriable Specific Impulse Magnetoplasma Rocket(VASIMR). Figures 1.1 and 1.2 show examples of some of Hall thrusters and VASIMR.

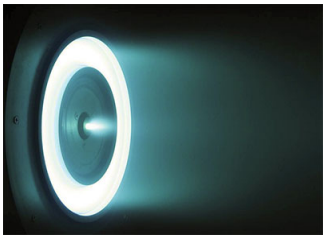

Figure 1.1: Hall thruster. Credit: PEPL

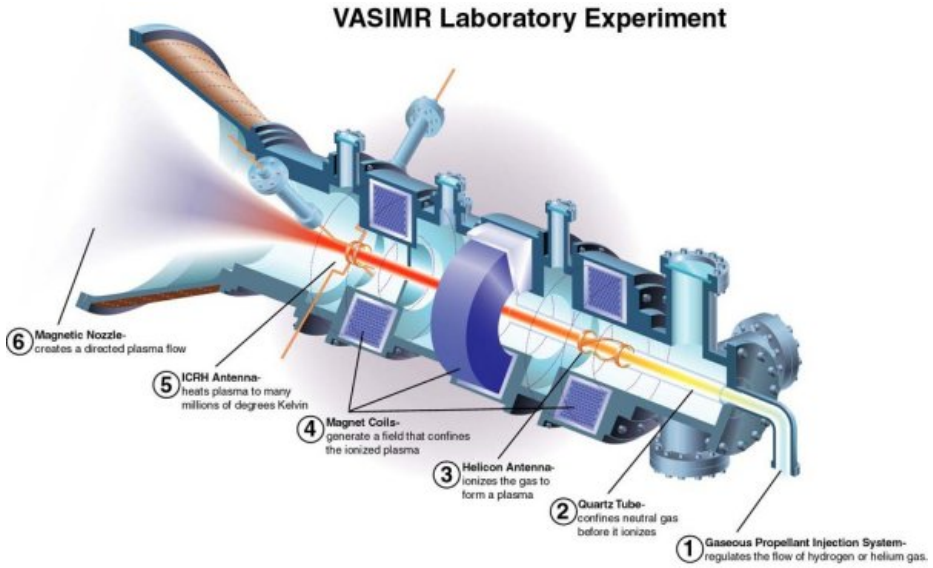

Figure 1.2: VASIMR Schematic [13]

Figure 1.3 shows the specific impulse and thrust regimes for some of the discussed propulsion methods. Chemical and nuclear thermal propulsion provide the greatest thrust, but have low specific impulse. Electric propulsion, particularly electrostatic and electromagnetic propulsion, have high specific impulse but much lower thrust. The firing time for chemical propulsion devices is normally several minutes, whereas electric propulsion devices may operate for months at a time. This demonstrates that the key difference between electric and chemical propulsion. Electric propulsion devices are extremely efficient with propellant use and operate over extended periods of time while chemical propulsion provides short, high thrust impulses. Electric propulsion systems are therefore more suited for long term space missions, but require a power source to operate.

This figure also shows contours of constant propulsive power. This propulsive power can be related to the power required for the system through efficiency factors. These contours demonstrate the approximate power regimes at which the different propulsion systems operate to produce the given specific impulse and thrust.

Electric propulsion devices which are currently in use fall primarily in the electrostatic thruster regime. Electromagnetic propulsion methods are the preferred choice for space application. The virtue of electromagnetic propulsion lies in the projected increased thrust that these systems can provide while maintaining high specific impulse. They strive to bridge the gap between current electrostatic propulsion devices and chemical propulsion by providing a propulsion method which is efficient and also produces thrust capable of performing maneuvers on shorter time scales than current electric propulsion systems.

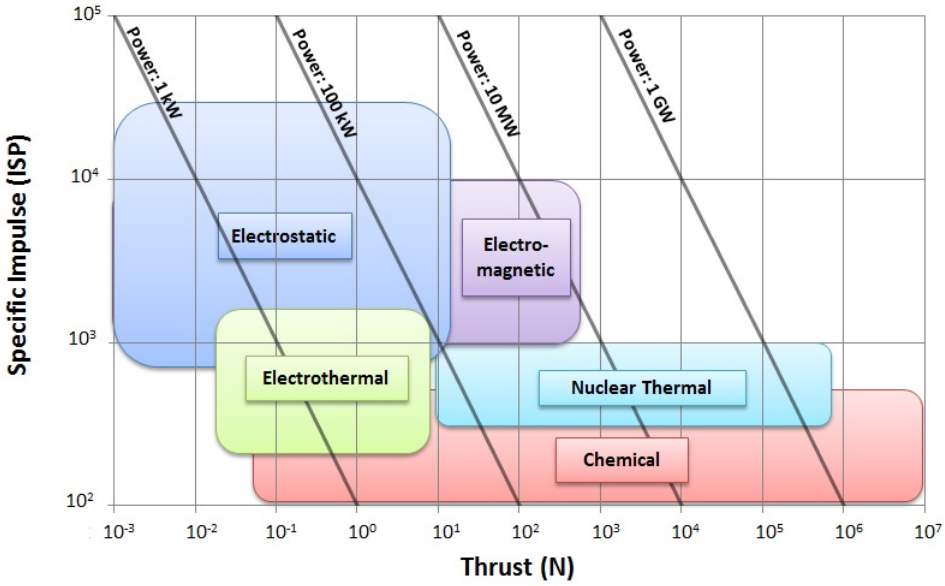

Figure 1.3: Thrust vs specific impulse of space propulsion methods

1.3 Magnetic Nozzle Problem

Electromagnetic propulsion devices currently being developed include a strong guiding field known as a magnetic nozzle to confine plasma flow and produce thrust. Among the devices that utilize magnetic nozzles are the VAriable Specic Impulse Magnetoplasma Rocket (VASIMR), magnetoplasmadynamic thrusters (MPDs), and helicon thrusters. Magnetic nozzles are functionally similar to De Laval nozzles; they operate by converting energy from other modes into uni-directional kinetic energy which will ultimately be harnessed for thrust. The virtue of magnetic nozzles lies in minimizing contact between the high temperature plasma and surfaces while also providing additional mechanisms for thrust generation by plasma-field interaction. The ability to vary the magnetic field topology also gives magnetic nozzles versatility which is not possible in De Laval nozzles. A comparison of the magnetic nozzle to the conventional De Laval nozzle is shown in Figure 1.4.

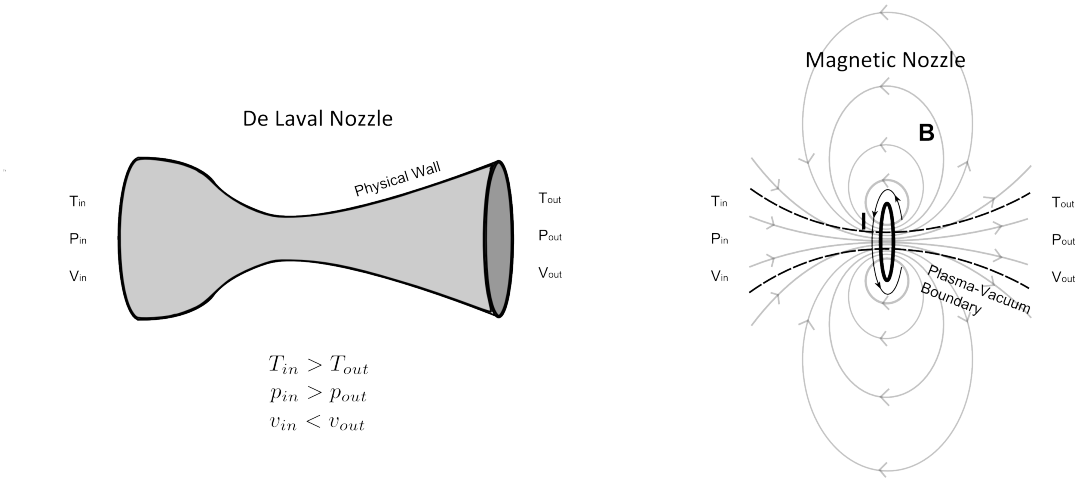

Figure 1.4: De Laval nozzle comparison with magnetic nozzle

Although similar in purpose, magnetic nozzles are inherently more complex due to the plasmadynamics resulting from plasma-field interactions. Three key steps are required to generate thrust in magnetic nozzles:

1. Conversion of magnetoplasma energy to directed kinetic energy
2. Efficient plasma detachment
3. Momentum transfer from plasma to spacecraft

These steps impose conflicting requirements – in the energy transfer phase, the magnetic field must confine the plasma whereas in the detachment stage the plasma must break free from the same field. This duality illustrates the challenge associated with magnetic nozzle design. The incumbent physical phenomena are an active research topic and must be understood to optimize magnetic nozzle design. The goal of this research is to study the physics of magnetic nozzles in order to optimize design for future space propulsion applications.

1.4 Solver Description

Theoretical and computational research have made significant progress in understanding the mechanisms of thrust generation in magnetic nozzles. Efforts to study plasma flows in magnetic nozzles have primarily sought time independent steady state solutions using the two fluid or ideal magnetohydrodynamics (MHD) methods while making a number of simplifying assumptions.[26, 34, 6, 10, 50, 39, 1, 40, 2, 41] These models generally focus on studying specific mechanisms for energy conversion, plasma detachment, or momentum transfer. This specialized study has significantly developed the understanding of the different facets of magnetic nozzle physics but questions still remain about the coupling of the different mechanisms and how they relate to experimental results. The goal of our research is not to examine a specific mechanism, but to study the system as a whole by performing fully 3D, time-dependent numerical experiments using an MHD solver known as the Magneto Gas Kinetic Method (MGKM).[22] Transient phenomena such a magnetic reconnection require time-dependent solvers. The long term goal is for the numerical experiments to be based on physical experimental setups[38, 13, 31, 64, 20, 63] and will allow the different physical mechanisms to couple with one another. The solver will strive to replicate experimental conditions and identify the dominant physics. Such computational capability when fully developed can be used to optimize magnetic nozzle design.

1.5 Research Contributions

This research is aimed toward contributing to the body of knowledge of magnetohydrodynamics through theoretical and computational studies. The various studies are outlined below:

1. An extensive literature survey that defines the regimes in which magnetic noz-

zles operate, determines the crucial physical phenomena of magnetic nozzles, and establishes the current state of magnetic nozzle physics

2. Order of magnitude analyses are done to determine the validity of magnetohydrodynamics for studying the magnetic nozzle problem and establish the type of magnetohydrodynamics solver necessary to capture all relevant physics

3. Further develop the Magneto-Gas Kinetic Method to incorporate Hall effect physics. The electron pressure term is also incorporated, but not extensively studied.

4. The effects of Hall physics are characterized in 1D, 2D, and 3D flows and the new numerical solver validated. Numerous of these cases studied are not well documented in literature.

5. The physics of the Hall effect in magnetic nozzle plasma flows is studied through numerical experiments

1.6 Outline of Thesis

The thesis begins with an introduction to the background physics necessary to study magnetic nozzles. The specific magnetic nozzle physics are discussed along with a literature review of previous work. The theory and development of the Magneto Gas Kinetic Method solver are then discussed. Validation results are then presented to confirm the accuracy of MGKM in the compressible and Hall physics regime. Finally preliminary jet results are presented which demonstrate the effects of the Hall term on magnetic nozzle flows.

2. PLASMA PHYSICS AND MAGNETOHYDRODYNAMICS

2.1 Introduction

Plasmas are abundant in the universe but are rare on Earth. The Aurora Borealis, lightning, and the sun are examples of plasma phenomena on our planet and in our solar system. Figure 2.1 shows an image of the Aurora Borealis. Despite the prevalence of plasma in the universe, an intuitive understanding of plasmadynamics is difficult to achieve due to the lack of physical interaction people have with them. Compared with the other states of matter, it is rare for people to touch, feel, or see the flow of plasmas.

Figure 2.1: Aurora Borealis. Credit: Aggie Balloon Club and Project Aether

Plasmas are often referred to as the fourth state of matter. They are formed when gases reach high enough temperatures at which a significant portion of the

gas is ionized and distinct species of positively charged ions, negatively charged electrons, and neutrals are present. The introduction of new species with differing charges significantly complicates the dynamics of plasma flows, coupling the fluid or particle dynamics equations with Maxwell's equations. Laboratory plasmas have temperatures which can reach up to one million Kelvin and have densities of about 10^{18} particles per meter cubed. Though they may be at high temperatures, only few collide with a surface and transfer heat to it. It is also of note that the electrons and ions can have separate temperatures. [14]

The purpose of this chapter is to give a brief overview of plasma physics and the resulting plasmadynamics equations. This chapter will begin with the overview of plasma physics which will cover basic electromagnetism and plasma physics. This will be followed by a section describing the kinetic theory description of plasma dynamics and will conclude with a derivation of the magnetohydrodynamics (MHD) equations.

2.2 Classical Electrodynamics

Classical electrodynamics is a branch of physics that describes the dynamics of particles due to the forces derived from the charges of the particles. The concept of charge and the forces between these charges is the most fundamental part of electromagnetic theory. The charge of a particle is a quantized amount determined by the amount of protons and electrons present. The charge of individual protons and electrons is a universal constant with protons holding positive charge and electrons holding negative charge. The nature of the forces between charges results in like charge repelling one another while opposite charges attract one another. This fundamental force is defined by the Coulomb's Law shown in Equation 2.1. In this equation q represents the charge of the particles and r the radial distance between

those particles.

$$\mathbf{F} = \frac{1}{4\pi\epsilon_0}\frac{q_1 q_2}{r^2}\hat{r} \tag{2.1}$$

From this force can be derived the fundamental field of classical electromagnetic theory known as the electric field. The electric field is used to describe the force a particle would experience in the presence of another particle. The equation for the electric field and the force due to the electric field is shown in Equations 2.2 and 2.3.

$$\mathbf{E} = \frac{1}{4\pi\epsilon_0}\frac{q}{r^2}\hat{r} \tag{2.2}$$

$$\mathbf{F} = q\mathbf{E} \tag{2.3}$$

The form of these equations allows the electric field to be described by a potential known as the electric potential, Φ. The electric potential can be found by integrating the electric field over any arbitrary path. The relationship between the electric field and the electric potential are shown in Equations 2.4 and 2.5.

$$\Phi = \int_c \mathbf{E} \cdot d\mathbf{l} \tag{2.4}$$

$$\mathbf{E} = -\nabla\Phi \tag{2.5}$$

The electric potential can then also be used to describe the potential energy U by multiplying by the charge of the particle. This is shown in Equation 2.6.

$$U_E = q\Phi \tag{2.6}$$

The motion of charged particles coupled with the finite speed of light results in the second fundamental field used to describe the dynamics of charged particles. This field created by the motion of charged particles is the magnetic field B and can be found through the Biot-Savart Law shown in Equation 2.7.

$$\mathbf{B} = \int \frac{\mu_0}{4\pi} \frac{I d\mathbf{l} \times \hat{r}}{r^2} \tag{2.7}$$

The force on a charged particle due to both of these fields is known as the Lorentz Force shown in Equation 2.8

$$\mathbf{F} = q(\mathbf{E} + \mathbf{v} \times \mathbf{B}) \tag{2.8}$$

The relationship between the electric and magnetic fields are found by further manipulation of the given equations describing these fields and result in what are known as Maxwell's equations. Maxwell's equations in a vacuum are shown in Equations 2.9 - 2.12. These equations have several forms, the forms shown are chosen because they are most applicable for the study of plasma physics. In these equations ρ_{charge} is the charge density and J is the current density which act as source terms for the electric and magnetic fields respectively.

$$\nabla \cdot \mathbf{E} = \frac{\rho_{charge}}{\epsilon_0} \tag{2.9}$$

$$\nabla \cdot \mathbf{B} = 0 \tag{2.10}$$

$$\nabla \times \mathbf{E} = -\frac{\partial \mathbf{B}}{\partial t} \tag{2.11}$$

$$\nabla \times \mathbf{B} = \mu_0 \mathbf{J} + \mu_0 \epsilon_0 \frac{\partial \mathbf{E}}{\partial t} \tag{2.12}$$

Manipulating Maxwell's equations can lead to insight into the nature of electromagnetic fields. Assuming a charge free space and manipulating some of these equations leads to the derivation of the wave equations for the electric and magnetic fields shown in Equations 2.13 and 2.14.

$$\frac{\partial^2 \mathbf{B}}{\partial t^2} = c^2 \nabla^2 \mathbf{B} \tag{2.13}$$

$$\frac{\partial^2 \mathbf{E}}{\partial t^2} = c^2 \nabla^2 \mathbf{E} \tag{2.14}$$

Combining the source equations (Equation 2.9 and 2.12) leads to an expression for the conservation of charge shown in Equation 2.15.

$$\frac{\partial \rho_{charge}}{\partial t} = \nabla \cdot \mathbf{J} \tag{2.15}$$

Multiplying Equations 2.11 by $\mathbf{B}$ and Equation 2.12 by $\mathbf{E}$ and manipulating these equations through vector Calculus leads to Equation 2.16 which describes the time evolution of the electromagnetic field energy.

$$\frac{\partial}{\partial t}\left(\frac{\mathbf{B}^2}{2\mu_0} + \frac{\epsilon_0 \mathbf{E}^2}{2}\right) = -\mathbf{E} \cdot \mathbf{J} - \nabla \cdot (\mathbf{E} \times \mathbf{B}) \tag{2.16}$$

This equation describes the change in the energy of the electromagnetic fields over time. The first term on the right hand side, $\mathbf{E} \cdot \mathbf{J}$, represents the energy exchanged between the fields and charged particles. As the fields lose energy, the particles gain energy. This term shows up with an opposite sign in the energy equation

for the particles. The last term in Equation 2.16 represents the convection of the electromagnetic fields and is characterized by the Poynting vector, $\mathbf{E} \times \mathbf{B}$.

2.3 Basic Plasma Physics Concepts

In thermodynamics of non-conducting fluids two parameters are used to characterize the state of a gas. Plasma physics complicates this by requiring a third fundamental parameter to characterize the plasma. Most often these fundamental parameters are the number density, n, the temperature of each species, T, and the magnetic field strength, B. [8]

By definition plasmas are quasineutral and exhibit collective behavior. [14] Quasineutrality implies that when concentrations of charge or external potentials arise in plasma, they are shielded out in a length, the Debye length, much smaller than the system dimension. This results from a phenomenon known as Debye shielding. Quasineutrality also leads to the assumption that the ion and electron densities are equal and have a common density known as the plasma density. The term collective behavior implies that plasmas have strong non-local effects due to the long range electromagnetic forces. Collective behavior also implies that there are enough particles so that Debye shielding can occur. These two definitions help define two of the conditions for an ionized gas to be a plasma. There is also a third condition which states that the interactions in plasma must be controlled by electromagnetic forces rather than hydrostatic forces. This third condition is defined by requiring the plasma oscillation frequency to be greater than the frequency of collisions with neutrals. These three conditions are summarized below in Equations 2.17 - 2.19. In these equations L_D is the Debye length and N_D is the number of particles in the Debye sphere. [14]

$$L_D \ll L \tag{2.17}$$

$$N_D \gg 1 \tag{2.18}$$

$$\omega_p \tau_{col,n} > 1 \tag{2.19}$$

The motion of the constituent particles in plasma is defined by the electromagnetic effects that ions and electrons have on one another as well as the effects of outside fields. Applied magnetic fields cause the charged particles to stream along and revolve around the magnetic field lines in a helical pattern. This is caused by the Lorentz Force and is characterized by the cyclotron frequency and the Larmor radius shown in Equations 2.20 and 2.21 respectively. In these equations $v_\perp$ indicates the velocity perpendicular to the magnetic field. Electrons having smaller mass, have much higher cyclotron frequencies and much smaller Larmor radii under the same conditions as the ions.

$$\omega_c = \frac{|q|\,|B|}{m} \tag{2.20}$$

$$r_L = \frac{v_\perp}{\omega_c} \tag{2.21}$$

Collisions in plasmas are more complex than in regular fluids due to the effect of the long range electromagnetic forces. In particular the collisions can be modeled in various ways, two of which are the Fokker-Planck Collision Operator and the Bhatnagar Gros Krook Collision Operator.

2.4 Dynamics of Plasmas

At the most basic level the Lorentz force tends to make charged particles flow along and orbit around magnetic field lines in a helical pattern. This behavior becomes significantly more complex with the addition of external forces and spatially or temporally varying electromagnetic fields. The motion is further complicated if the plasma is considered as a fluid consisting of numerous particles. In this section we will briefly discuss some basic particle and fluid motion associated with plasmas.

2.4.1 Single Particle Motion

The addition of external forces and varying fields significantly complicates the motion of charged particles. The drift of the guiding center of the particle orbit is used to describe the particle dynamics instead of the cyclical motion. For the sake of brevity the different types of drifts will not be discussed in detail, but are presented in Table 2.1 for future reference. [14]

General Force	$\mathbf{v} = \frac{1}{q}\frac{\mathbf{F}\times\mathbf{B}}{B^2}$
Electric Field	$\mathbf{v} = \frac{\mathbf{E}\times\mathbf{B}}{B^2}$
Non-Uniform Electric Field	$\mathbf{v} = \left(1 + \frac{1}{4}r_L^2\nabla^2\right)\frac{\mathbf{E}\times\mathbf{B}}{B^2}$
Gradient of Magnetic Field	$\mathbf{v} = \pm\frac{1}{2}v_\perp r_L\frac{\mathbf{B}\times\nabla\mathbf{B}}{B^2}$
Curvature of Field Lines	$\mathbf{v} = \frac{mv_\parallel^2}{1}\frac{\mathbf{R}_c\times\mathbf{B}}{R_c^2B^2}$
Polarization	$\mathbf{v} = \pm\frac{1}{\omega_c B}\frac{d\mathbf{E}}{dt}$

Table 2.1: Single particle guiding center drifts

Another important characteristic of single particle motion is the existence of adiabatic invariants. Adiabatic invariants are constants of motion that exist when a system undergoes slow changes. An adiabatic invariant that is of particular interest is the magnetic moment of a charged particle, μ_m. The magnetic moment of a particle is an adiabatic constant of motion if $\Delta B << B$ over a single period of cyclotron

motion. The conditions for adiabaticity may be represented by the relations shown in Equation 2.23. The most often used condition describes the ratio of the Larmor radius, $r_L = mv_\perp/(qB)$, to the characteristic length scale of the magnetic field change defined $1/|\frac{\nabla \mathbf{B}}{\mathbf{B}}|$.

$$\mu_m = \frac{mv_\perp^2}{2B} \tag{2.22}$$

$$\dot{B} \ll B\omega_c \quad or \quad \nabla_\parallel B \ll B\frac{v_\parallel}{\omega_c} \quad or \quad r_L\frac{\nabla_\perp B}{B} \ll 1 \tag{2.23}$$

The magnetic moment is a simplified representation of a more complex physics derivable from Lagrangian mechanics. [54]

2.4.2 Elementary Fluid Drifts

Plasmas may also be described as fluids in which numerous particle motions are represented by large scale macroscopic behavior. In the fluid description, plasmas will generally prefer to flow along magnetic field lines and not across them. This behavior is rooted in the single particle motions described in the previous section. Plasma can flow across magnetic field lines due to resistive diffusion and fluid drifts similar to some of the particle drifts. The basic types of fluid drift perpendicular to the field direction are shown in Equations 2.24 and 2.25.

$$v = \frac{\mathbf{E} \times \mathbf{B}}{B^2} \tag{2.24}$$

$$v = -\frac{\nabla p \times \mathbf{B}}{qnB^2} \tag{2.25}$$

Equation 2.24 is known as the $\mathbf{E} \times \mathbf{B}$ drift and Equation 2.25 is known as the

diamagnetic drift. It is also important to note that nonuniform magnetic fields do not result in fluid drifts. These drifts represent the fluid motion for each species perpendicular to the magnetic field.

2.5 Kinetic Theory Description of Plasmas

Kinetic theory is based primarily on the idea of the particle distribution function, $f = f(x_1, x_2, x_3, v_1, v_2, v_3, t)$. The distribution function is a function of physical space, velocity space, and time and is defined so that $f dx_1 dx_2 dx_3 dv_1 dv_2 dv_3$ gives the number of particles within physical space element $dx_1 dx_2 dx_3$ and the velocity space element $dv_1 dv_2 dv_3$. The distribution function can be thought of as representing the number of particles residing within a certain range of velocities, velocity space, inside a certain physical space at a given time. When this function is integrated over the entire velocity space, $n = \int_{-\infty}^{\infty} f \, dv_1 dv_2 dv_3$, n gives the particles per unit volume. The equilibrium distribution function, g, is the Maxwellian distribution function shown below which is defined so that integration yields the mass density of particles.

$$g = \rho\Big(\frac{\lambda}{\pi}\Big)^{\frac{N+3}{2}} e^{-\lambda[(\mathbf{v}-\mathbf{u})\cdot(\mathbf{v}-\mathbf{u})+\xi^2]} \tag{2.26}$$

In Equation 2.26 λ is a constant defined by $\frac{m}{2kT}$, v is the particle velocity, u is the macroscopic fluid velocity, N is the internal degrees of freedom, and ξ is an internal particle velocity. The particle velocity is composed of three independent variables v_1, v_2, and v_3. N represents the number of internal degrees of freedom (such as rotation and vibration) , it is different from normal degrees of freedom in that it does not include the translational degrees of freedom. The number of degrees of freedom is related to the ratio of specific heats γ by Equation 2.27. It is important to note that the convention chosen is that which is most convenient for later use in relation to the Gas Kinetic Method.

$$N = \frac{5 - 3\gamma}{\gamma - 1} \tag{2.27}$$

The parameter ξ is the component of internal particle velocity (from rotations, vibrations, etc) that has K total degrees of freedom. It is meant help to account for the total internal energy and varies between 1D - 3D flows because the translations which are not resolved in 1D and 2D flows become part of K. For 1D flow $K = N + 2$, 2D flow $K = N + 1$, and 3D flow $K = N$. Also note that for simplicity $\xi^2 = \xi_1^2 + \xi_2^2 + ... + \xi_K^2$

The relationship between the particle distribution function and the macroscopic variables is defined by the Equations 2.28 and 2.29.

$$\Psi = [\rho, \rho u_1, \rho u_2, \rho u_3, E]^T = \int_{-\infty}^{\infty} \psi f \, d\Xi \tag{2.28}$$

$$\psi = [1, v_1, v_2, v_3, \frac{1}{2}(v_1^2 + v_2^2 + v_3^2 + \xi^2)]^T \tag{2.29}$$

In Equation 2.28, ρ is the mass density, u is the macroscopic velocity, $E = \frac{1}{2}\rho(u_1^2 + u_2^2 + u_3^2 + \frac{N+3}{2\lambda})$ is the energy density (sum of kinetic and thermal energy densities). In Equation 2.28, $d\Xi = dv_1 dv_2 dv_3 d\xi$ is the volume element in phase space with $d\xi = d\xi_1 d\xi_2 ... d\xi_K$.

2.5.1 The Boltzmann Equation

The time evolution of the particle distribution function is described by the Bolzmann equation shown in Equation 2.30.

$$\frac{\partial f}{\partial t}+\left(\frac{\partial f}{\partial x_1}\frac{\partial x_1}{\partial t}+\frac{\partial f}{\partial x_2}\frac{\partial x_2}{\partial t}+\frac{\partial f}{\partial x_3}\frac{\partial x_3}{\partial t}\right)+\left(\frac{\partial f}{\partial v_1}\frac{\partial v_1}{\partial t}+\frac{\partial f}{\partial v_2}\frac{\partial v_2}{\partial t}+\frac{\partial f}{\partial v_3}\frac{\partial v_3}{\partial t}\right)=\left(\frac{\partial f}{\partial t}\right)_{col} \tag{2.30}$$

The right hand side operator is known as the collisional operator and acts on the equation similar to the way forces act on the Navier Stokes equation. To be more specific, the collisional operator represents how the fluid changes due to collisions of particles. Choosing how to represent this collisional operator is one of the primary unknowns in this equation. One of the simplest ways to represent this operator is by using the Bhatnagar-Gross-Krook (BGK) approximation. The BGK approximation is a first order linear approximation which when applied to the Boltzmann Equation gives the Bolzmann-BGK (BBGK) equation, shown in Equation 2.31, which will be used in the GKM solver.

$$\frac{\partial f}{\partial t}+\mathbf{v}\cdot\nabla f+\mathbf{a}\cdot\nabla_{\mathbf{v}}f=\frac{g-f}{\tau} \tag{2.31}$$

In this equation $\mathbf{a}$ is the particle acceleration, $\nabla f=\frac{\partial f}{\partial x_1}\hat{i}+\frac{\partial f}{\partial x_2}\hat{j}+\frac{\partial f}{\partial x_3}\hat{k}$ is the gradient of f in physical space, and $\nabla_{\mathbf{v}}f=\frac{\partial f}{\partial v_1}\hat{v}_i+\frac{\partial f}{\partial v_2}\hat{v}_j+\frac{\partial f}{\partial v_3}\hat{v}_k$ is the gradient of f in velocity space. The variable τ in this equation is known as the characteristic relaxation time and represents the time it take for a system to return to equilibrium after it has been disturbed. This equation is further simplified if there are no source terms or external forces leading to the form in Equation 2.32.

$$\frac{\partial f}{\partial t}+\mathbf{v}\cdot\nabla f=\frac{g-f}{\tau} \tag{2.32}$$

2.5.2 The Vlasov Equation

The Vlasov equation is a form of the Boltzmann equation which is more suited for studying the flow of plasmas. A collisionless Boltzmann equation is assumed which may take one of the following two forms in Equations 2.33 and 2.34.

$$\frac{\partial f}{\partial t} + \mathbf{v} \cdot \nabla f + \mathbf{a} \cdot \nabla_v f = 0 \tag{2.33}$$

$$\frac{\partial f}{\partial t} + \mathbf{v} \cdot \nabla f + \cdot \nabla_v (\mathbf{a} f) = 0 \tag{2.34}$$

The acceleration in these equations is replaced by the Lorentz force. The equation given in 2.33 suggests that for a particle moving in phase space the relation of Equation 2.35 is true. This implies that from the viewpoint of a particle the distribution function is constant in time if a collisionless Vlasov equation is assumed.

$$\frac{df}{dt} = \frac{\partial f}{\partial t} + \mathbf{v} \cdot \nabla f + \mathbf{a} \cdot \nabla_v f = 0 \tag{2.35}$$

2.5.3 Kinetic Theory and Conservation Equations

Moments of the Boltzmann and Vlasov equations are taken to obtain macroscopic conservation equations for non-conducting and conducting fluids. As we are discussing primarily plasma physics we will focus on the integration of the Vlasov equation with the added effect of collisions. This primarily follows the derivation of Bellan.[8] The equation for the individual species of a plasma including the effects of collisions is shown in Equation 2.36.

$$\frac{\partial f_\sigma}{\partial t} + \mathbf{v} \cdot \nabla f_\sigma + \mathbf{a} \cdot \nabla_v f_\sigma = \sum_\alpha C_{\sigma\alpha}(f_\sigma) \tag{2.36}$$

The effects of the collisions are constrained by the following relations:

1. Collisions can not change the total number of particles
2. Collisions between particles of the same species can not change the total momentum or energy of that species
3. Collisions between particles in different species can not change the total momentum or energy of the system

Taking the zeroth, first, and second moment of Equation 2.36 for each of the species and applying the collisional constraints leads to the continuity, conservation of momentum, and conservation of energy equations respectively for each species. The different species are coupled through the collision operator and the electromagnetic field. The resulting conservation equations are shown in Equations 2.37 - 2.39. [8]

$$\frac{\partial n_\sigma}{\partial t} + \nabla \cdot (n_\sigma \mathbf{u}_\sigma) = 0 \tag{2.37}$$

$$n_\sigma m_\sigma \frac{d\mathbf{u}_\sigma}{dt} = n_\sigma q_\sigma (\mathbf{E} + \mathbf{u}_\sigma \times \mathbf{B}) - \nabla p_\sigma - \mathbf{R}_{\sigma\alpha} \tag{2.38}$$

$$\frac{\partial}{\partial t}\left(\frac{Np_\sigma}{2} + \frac{m_\sigma n_\sigma u_\sigma^2}{2}\right) + \nabla \cdot \left(\mathbf{Q}_\sigma + \frac{2+N}{2} p_\sigma \mathbf{u}_\sigma + \frac{m_\sigma n_\sigma u_\sigma^2}{2}\mathbf{u}_\sigma\right) - q_\sigma n_\sigma \mathbf{u}_\sigma \cdot \mathbf{E} = -\left(\frac{\partial W}{\partial t}\right)_{E\sigma\alpha} \tag{2.39}$$

To arrive at these conservation equations the velocity field was assumed to be composed of a mean, $\mathbf{u}(\mathbf{x}, t)$, and a fluctuating part, $\mathbf{v'}(\mathbf{x}, t)$ which resulted in the relations shown in Equation 2.40 and 2.41. The parameter N in these equations is the dimension of the random velocity and is defined differently from that of Xu where N is the dimension of the internal degrees of freedom excluding the translational

motion. Equation 2.40 describes the pressure tensor of the individual species and Equation 2.41 describes the heat flux.

$$p_\sigma = \frac{m_\sigma}{N} \int \mathbf{v'} \cdot \mathbf{v'} f_\sigma d^N \mathbf{v'} \tag{2.40}$$

$$\mathbf{Q}_\sigma = \int \frac{m_\sigma \mathbf{v'}^2}{2} \mathbf{v'} f_\sigma d^N \mathbf{v} \tag{2.41}$$

The terms $R_{\sigma\alpha}$ and $\left(\frac{\partial W}{\partial t}\right)_{E\sigma\alpha}$ represent the effects of the collisions between the species and require transport relations to fully close the system of equations.

2.6 Magnetohydrodynamics

Magnetohydrodynamics (MHD) is a simplification of the multi-fluid equations in which the plasma is treated as a single fluid. New variables are needed for this treatment which are shown in Equations 2.42 - 2.44. These equations respectively represent the total mass density ρ, the center of mass velocity U, and the current density J.

$$\rho = \sum_\sigma m_\sigma n_\sigma \tag{2.42}$$

$$\mathbf{U} = \frac{1}{\rho} \sum_\sigma m_\sigma n_\sigma \mathbf{u}_\sigma \tag{2.43}$$

$$\mathbf{J} = \sum_\sigma n_\sigma q_\sigma \mathbf{u}_\sigma \tag{2.44}$$

The MHD equations are found by summing the multi-fluid conservation equations over all species and writing the equations in terms of the newly defined variables. The resulting MHD conservation equations are shown in Equations 2.45 - 2.47.

$$\frac{\partial \rho}{\partial t} + \nabla \cdot (\rho \mathbf{U}) = 0 \tag{2.45}$$

$$\frac{\partial (\rho \mathbf{U})}{\partial t} + \nabla \cdot \left[\rho \mathbf{U}\mathbf{U} + \underline{\underline{\tau}} + \underline{\underline{I}} p \right] = \mathbf{J} \times \mathbf{B} \tag{2.46}$$

$$\frac{\partial e}{\partial t} + \nabla \cdot \left[\mathbf{U}(e+p) - k \nabla T + \mathbf{U} \cdot \underline{\underline{\tau}} \right] = \mathbf{J} \cdot \mathbf{E} \tag{2.47}$$

In the these equations $\underline{\underline{\tau}}$ is the dissipative stress tensor and e is the hydrodynamic energy, $e = \rho U^2/2 + p/(\gamma - 1)$. The energy equation may also be rewritten in terms of an energy which includes the electromagnetic field energy, $e_{tot} = \rho U^2/2 + p/(\gamma - 1) + B^2/2\mu_0$, which is shown in 2.48.

$$\frac{\partial e_{tot}}{\partial t} + \nabla \cdot \left[\mathbf{U}(e+p) - k \nabla T + \mathbf{U} \cdot \underline{\underline{\tau}} + \frac{\mathbf{E} \times \mathbf{B}}{\mu_0} \right] = 0 \tag{2.48}$$

These conservation equations are not closed and require an additional equation relating $\mathbf{J}$ to $\mathbf{U}$. This equation is known as Ohm's law, Equation 2.49, and is derived form the electron equation of motion while making the assumption that the electron time scales are much faster than the any other time scales. It is also assumed that the electron mass is negligible. It is in the derivation of Ohm's law that the MHD equations are most dramatically separated from the two fluid equations of motion. In this equation η characterizes the resistivity of the plasma.

$$\mathbf{E} = -\mathbf{U} \times \mathbf{B} + \frac{1}{n_e q} \mathbf{J} \times \mathbf{B} - \frac{1}{n_e e} \nabla (n_e k T_e) + \eta \mathbf{J} \tag{2.49}$$

3. MAGNETIC NOZZLE PHYSICS

Magnetic nozzles are functionally similar to De Laval nozzles, they generate thrust by converting thermal energy or non-directional kinetic energy to directed kinetic energy. The comparison between De Laval nozzles and magnetic nozzles is shown in Figure 3.1. The virtues of magnetic nozzles lie in minimizing contact between the high temperature plasma and surfaces, providing additional mechanisms for thrust generation by plasma-field interaction, and enabling the ability to vary the magnetic field topology providing versatility which is not possible in De Laval nozzles.

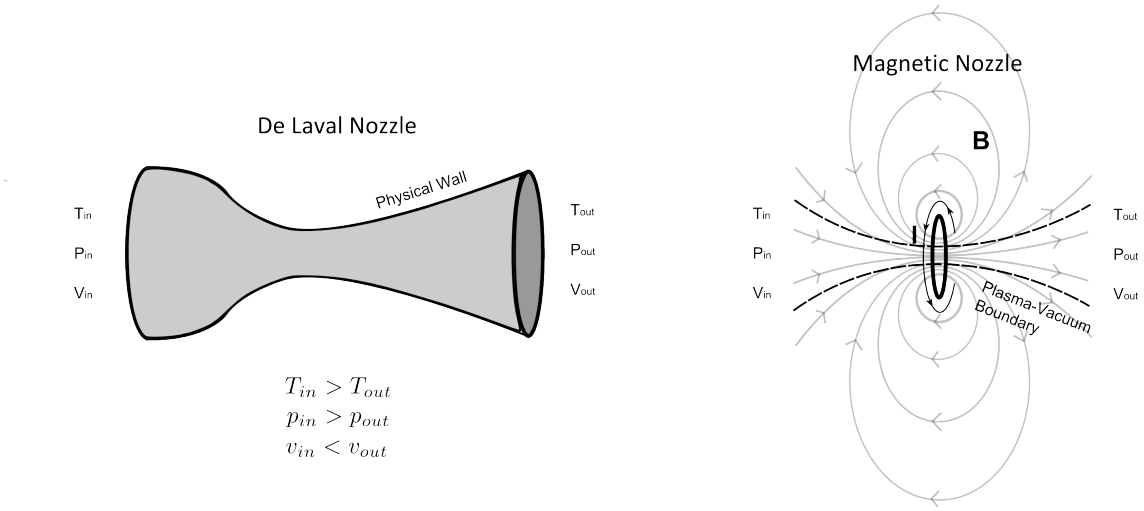

Figure 3.1: De Laval nozzle compared to magnetic nozzle

The physics of magnetic nozzle plasma flow is inherently complex, the magnetic fields must confine plasma to the correct configuration to produce kinetic energy while also ensuring efficient detachment from the closed applied magnetic field lines which tend to pull the plasma back to the spacecraft. Three key steps are required to produce thrust in magnetic nozzles:

1. Conversion of magnetoplasma energy to directed kinetic energy

2. Ensuring efficient plasma detachment

3. Transfer of momentum from the plasma to the spacecraft

These steps impose conflicting requirements of confinement and detachment which present the primary challenge in magnetic nozzle design. Although these processes are separated in the list above, they are intimately coupled with one another and must be understood to optimize magnetic nozzle design.

This chapter presents a literature survey of the crucial physics of plasma flow in magnetic nozzles.[23] Findings and advances on this topic will be consolidated, summarized, and analyzed to define the current status of magnetic nozzle theory while outlining areas in which additional work is required. The regimes in which the discussed magnetic nozzle physics are relevant will also be defined.

3.1 Energy Conversion Physics

An outline of magnetic nozzle energy exchange mechanisms and the respective modes between which energy is converted is shown below.

1. Conservation of magnetic moment adiabatic invariant: $v_\perp \rightarrow v_\parallel$

2. Electric field acceleration: $e_{electron} \rightarrow e_{ion}$

3. Directionalizing of thermal energy: $e_{thermal} \rightarrow e_{kinetic}$

4. Joule heating: $e_{field} \rightleftharpoons e_h$

The plasmadynamics of magnetic nozzles is a complex interplay of fluid dynamics and electromagnetism and although these mechanisms are considered separately in the following sections they are coupled. The separation of mechanisms is done in an attempt to provide physical insight on this complex system.

3.1.1 Conservation of Adiabatic Invariant

As stated previously, the magnetic moment of a particle, $\mu_m = \frac{mV_\perp^2}{2B}$, is an adiabatic invariant when $\Delta B << B$ over a single period of cyclotron motion. The conditions for adiabaticity may be represented by the relations shown in Equation 3.1 with the most often used condition describing the ratio of the Larmor radius, $r_L = mv_\perp/(qB)$, to the characteristic length scale of the magnetic field change defined $1/|\frac{\nabla B}{B}|$.

$$\dot{B} \ll B\omega_c \quad or \quad \nabla_\parallel B \ll B\frac{v_\parallel}{\omega_c} \quad or \quad r_L\frac{\nabla_\perp B}{B} \ll 1 \tag{3.1}$$

To further describe the adiabatic energy exchange a simplified energy equation for an isentropic, collisionless, and equipotential plasma is assumed.

$$K_{tot} = K_\perp + K_\parallel = \frac{mv_\perp^2}{2} + \frac{mv_\parallel^2}{2} = constant \tag{3.2}$$

From these conservation equations it is evident that a decrease in magnetic field strength results in an increase of velocity parallel to the magnetic field. This behavior is similar to the familiar physics of magnetic mirrors. Combining these equations results in the following relationship for the velocity parallel to the magnetic field.

$$v_\parallel = \sqrt{v_{tot}^2 - 2\mu_m B/m} \tag{3.3}$$

Additional insight can be gained by assuming a flow which is initially dominated by perpendicular velocity that gradually flows into a region with a very small magnetic field, $B \approx 0$. The downstream velocity for this flow is shown below and represents the complete conversion of energy associated with the magnetic moment to parallel kinetic energy.

$$v_{\parallel,max} = \sqrt{2\mu_m B_0/m} \tag{3.4}$$

The previous description is a simplified representation of complex physics which is presented by Nagatomo [47], Kosmahl [37], and Sercel[52]. The exchange of energy is driven by a force $F_\mu = -(\mu_m \hat{\mathbf{B}} \cdot \nabla)\mathbf{B}$ which may be simplified in the magnetic field direction to be $m\dot{v}_\parallel = -\mu_m \nabla_\parallel B$.

The VASIMR propulsion system generates energy primarily by this mechanism and has shown promising results.[13, 5, 30, 57, 43] Theoretical, computational, and experimental efforts have studied and demonstrated the thrust production capabilities of this mechanism.[47, 37, 52, 57, 43] It should also be noted that a study of single particle motion with Lagrangian mechanics leads to a more general conserved variable. [54]

3.1.2 Electric Field Acceleration

Electric field acceleration may be driven by the formation of ambipolar fields [42] or double layers[16, 63]. These plasma structures occur due to the high mobility of electrons compared to ions. This increased mobility is characterized by the thermal velocity, $v_{th} = \sqrt{k_B T/m}$. In expanding magnetic nozzles the mobile electrons establish an electron pressure gradient ahead of the slow ions. To maintain quasineutrality an electric field is established to accelerate ions to match the speed of the electrons. This results in an exchange of energy between the electron thermal velocity and the ion flow velocity. As the electrons continue trying to expand their thermal energy is converted to ion kinetic energy. Figure 3.2 shows a schematic of electric field acceleration.

Although both ambipolar acceleration and double layer acceleration are driven by similar physics they are distinctly different. Double layers are characterized by

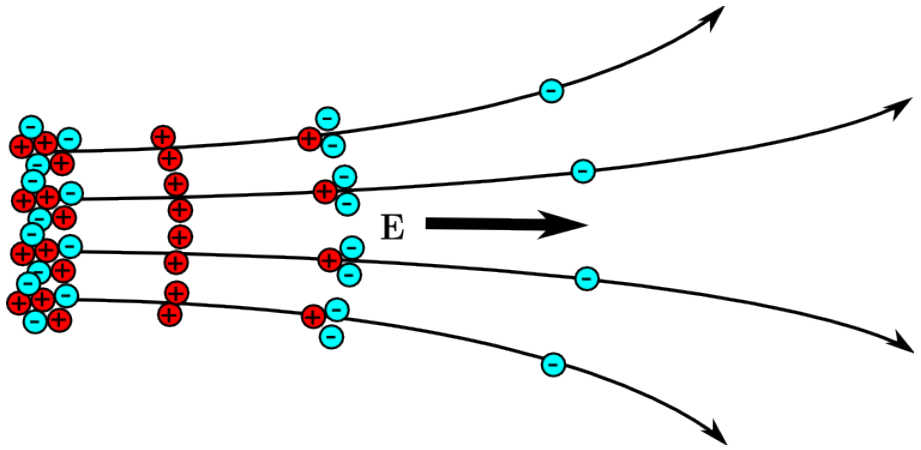

Figure 3.2: Electric field acceleration due to fast expanding electrons

a potential difference over a few Debye lengths while the potential difference for ambipolar effects may be on the order of the system's dimensions. Ambipolar acceleration has been studied computationally[7] and has shown encouraging results in experiments.[38, 42] Acceleration due to double layers has also been shown experimentally, but questions remain as to its feasibility as an acceleration mechanism.[16, 63]

3.1.3 Directionalizing Thermal Energy

Kinetic energy may be gained by directionalizing thermal energy. De Laval nozzles direct thermal motion into the axial direction through a converging-diverging physical wall. Magnetic nozzles do so by confining plasma to a desired geometry with a strong guiding field. The physics of energy conversion is based on hydrodynamics while the geometry of the magnetic nozzle is determined by plasma-field interaction. This implies that relationships based on hydrodynamics similar to those in De Laval nozzle analysis can be used to analyze this energy conversion if negligible losses occur in establishing the magnetic wall.

The most basic condition for confinement in relation to thermal forces is charac-

terized by the ratio of the fluid pressure to the magnetic pressure shown in Equation 3.5. When this relation is satisfied the magnetic pressure is stronger than the thermal pressure and confinement is possible but not guaranteed. Confinement of the plasma may also require the formation of a current layer at the plasma-vacuum boundary.[44, 62] Diffusive and convective processes may degrade the current layer and must be understood to characterize the losses due to non-ideal confinement.

$$\beta_P = \frac{nk_BT}{B^2/2\mu_0} < 1 \tag{3.5}$$

The physics of converting thermal energy to kinetic energy through the use of a magnetic nozzle has been demonstrated experimentally and computationally.[47, 38, 31, 32, 44] Kuriki [38] performed experiments and showed results which matched more closely with isentropic expansion models than with a magnetic moment conservation model. Kuriki [38] also suggests a magnetic nozzle Bernoulli's equation comprised of the ion and electron energy equations coupled by an electric potential. Although this gives physical insight, it does not provide a complete description of the numerous energy exchange mechanisms in magnetic nozzles. It should be clarified that for the discussed hydrodynamic energy conversion ion thermal energy is primarily converted to ion axial kinetic energy.

3.1.4 Joule Heating

Energy exchange can also occur between between the electromagnetic field and the hydrodynamic field as shown in a previous chapter. This exchange is best demonstrated by the MHD energy equation shown below:

$$\frac{\partial e_h}{\partial t} + \nabla \cdot \left[\mathbf{U}(e_h + p) - k\nabla T + \mathbf{U} \cdot \underline{\underline{\tau}}\right] = \mathbf{J} \cdot \mathbf{E} \tag{3.6}$$

The term on the right of Equation 5.28 represents the Joule heating and characterizes the energy gained by the fluid due to the energy lost by the electromagnetic field. This same term appears with an opposite sign in the energy equation for the electromagnetic field.

$$\frac{1}{2}\frac{\partial}{\partial t}\left(\epsilon_0 \mathbf{E}^2 + \frac{1}{\mu_0}\mathbf{B}^2\right) + \nabla \cdot \left[\frac{1}{\mu_0}\mathbf{E} \times \mathbf{B}\right] = -\mathbf{J} \cdot \mathbf{E} \tag{3.7}$$

The gain(loss) of energy by the fluid should be maximized(minimized). This relationship is complex and is coupled with the already mentioned methods.

3.2 Plasma Detachment

To generate thrust the directed kinetic energy must detach from the applied field. Plasma detachment mechanisms are critical to magnetic nozzle design because achieving efficient detachment minimizes losses due to electromagnetic drag forces and divergence of the plasma plume. Plasma detachment methods can be divided into three categories: collisional, collisionless, and magnetic reconnection detachment.

3.2.1 Collisional Detachment

Collisional detachment may be achieved through resistive diffusion across magnetic field lines[46, 66, 51] and recombination of the ions and electrons.[21, 15]

3.2.1.1 Resistive Diffusion

Resistive diffusion detachment is governed by the cross field diffusion of plasma.[46] Figure 3.3 gives a schematic of cross field diffusion. Resistive detachment exhibits conflicting requirements of initial confinement necessary for the correct nozzle geometry and eventual cross field diffusion to ensure detachment while minimizing resistive drag. Moses [46] defines conditions to ensure this duality is satisfied for resistive detachment in an adiabatically cooling plasma plume. It is suggested that a gradually

diverging magnetic field is preferred to ensure resistive detachment.

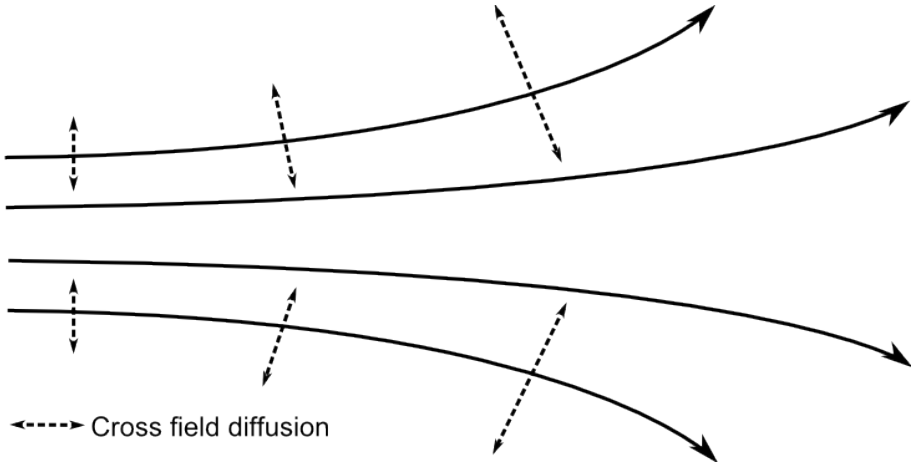

Figure 3.3: Resistive detachment due to cross field diffusion

The magnetic Reynolds number, $Re_m = UL/\eta$, is used to quantify the confinement of a plasma in a magnetic nozzle. For high values, $Re_m > 1000$, the resistive diffusion is negligible compared to convective effects and confinement is achieved. For intermediate values, $1 < Re_m < 1000$, diffusion is important and the plasma may move across magnetic field lines. High values of Re_m are required for confinement while intermediate to low numbers are required for detachment.[27, 51] It is important to note that although the magnetic Reynolds number provides insight on the diffusive behavior, quantitative comparisons should be done with caution due to the ambiguity of the scale length choice. Magnetic Reynolds numbers are best used for qualitative comparison and can only be used for quantitative comparison in systems which are physically and geometrically similar.

Predicting the extent at which plasma diffuses across a magnetic barrier has been studied and suggests that plasma may exhibit anomalous resistivity several orders of magnitude greater than predicted by classical plasma theory and Bohm diffusion.[11] The presence of anomalous resistivity should thus be considered for

computational studies. As a means to achieve detachment resistive diffusion has been largely considered as ineffective due to the adverse affects it would have on thrust production and likely divergent detachment that would occur.[2]

3.2.1.2 Recombination

Recombination achieves detachment by the formation of neutral particles which are no longer affected by the magnetic fields. Creation of neutrals is driven primarily by three body recombination in which two like charged particles and one unlike particle interact with one another forming a neutral and an energized particle. Figure 3.4 illustrates the recombination process. Recombination requires a sufficiently high electron-ion collision frequency, ν_{ei}, to be considered an effective means of detachment. Although initial analysis of recombination as a means for detachment are not encouraging, recombination rates can be increased by sharply decreasing magnetic field configurations or rapid cooling of electrons in the expanding nozzle. [21, 15]

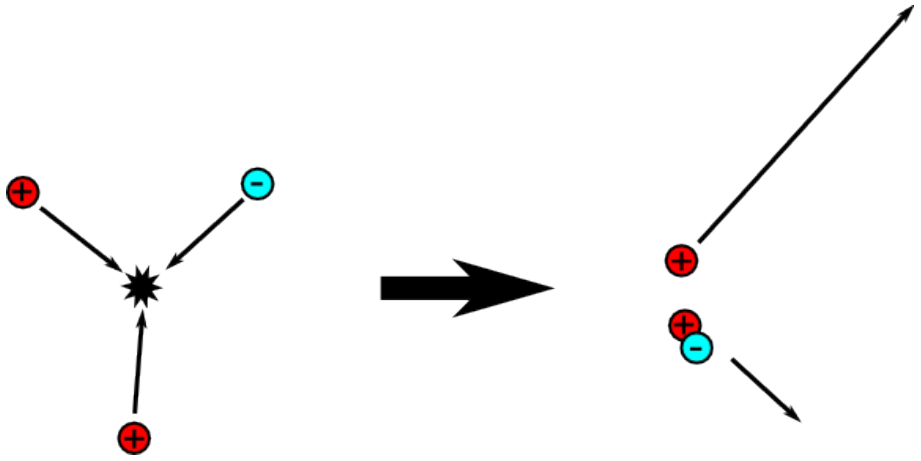

Figure 3.4: Schematic of recombination

3.2.2 Collisionless Detachment

Collisionless detachment has been the focus of most research. Among the considered means for achieving collisionless detachment are the loss of adiabicity, electron inertial effects, [30, 26, 34, 50, 40, 1, 2] and induced magnetic field effects[6, 10, 18, 19, 39, 64, 20, 1, 40, 2, 41].

3.2.2.1 Loss of Adiabaticity

Detachment due to the loss of adiabaticity occurs when the conditions of Equation 3.1 are violated and the plasma effectively becomes demagnetized. The third condition relating the Larmor radius of the particle to the characteristic length of magnetic field changes is the most often used to quantify detachment. Demagnetization implies that particles are no longer forced to have orbits which are bound to single field lines. This behavior can best be visualized by imagining a particle which starts an orbit around one field line but then during this orbit encounters a drastically different magnetic field which alters the previous orbit. Figure 3.5 graphically shows detachment due to the loss of adiabaticity.

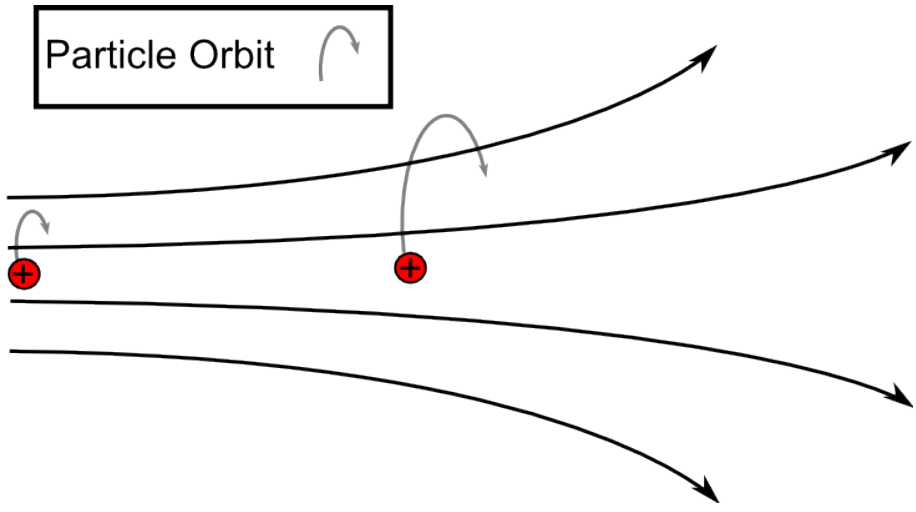

Figure 3.5: Loss of adiabaticity of plasma particles

Loss of adiabaticity is specific to each species with ions more likely to become demagnetized than electrons due to their significantly larger Larmor radii. Theory predicts that the loss of adiabaticity of ions alone does not ensure detachment due to the formation of electric fields between the bound electrons and the detached streaming ions.[26, 1, 2, 40, 45, 34] Detachment in this particular complex scenario is referred to as inertial detachment and will be discussed in the following section. Loss of adiabaticity describes a scenario for detachment of individual plasma species,[25] but only guarantees detachment for the plasma as whole when both species are demagnetized. [1, 2, 40, 45]

3.2.2.2 Inertial Detachment

As introduced in the previous section inertial detachment concerns the scenario when a only a single species becomes demagnetized and an electric field is established to maintain quasineutrality. Detachment of the plasma may still be achieved if the particles have enough inertia to overcome the retarding magnetic field forces. A hybrid Larmor radius based on a hybrid particle mass, $m_H = \sqrt{m_e M_I}$, is introduced to better examine this behavior. Detachment in this scenario can be imagined as the drift of a hybrid electron-ion particles. Figure 3.6 graphically shows the process of inertial detachment. The ratio of the magnetic inertia to the flow inertia is characterized by the non-dimensional parameter shown in Equation 3.8.[26, 34, 40]

$$G \approx \frac{eB_z}{m_e}\frac{eB_z}{M_i}\frac{r_0^2}{u_0^2} \tag{3.8}$$

Significant theoretical and computational study has been done to characterize the effectiveness of inertial detachment with some suggesting demagnetizaion based on the hybrid Larmor radius as an effective means for detachment[26, 34, 50, 41] and others suggesting only demagnetization of electrons effectively achieves detachment.[1,

2, 40, 45]

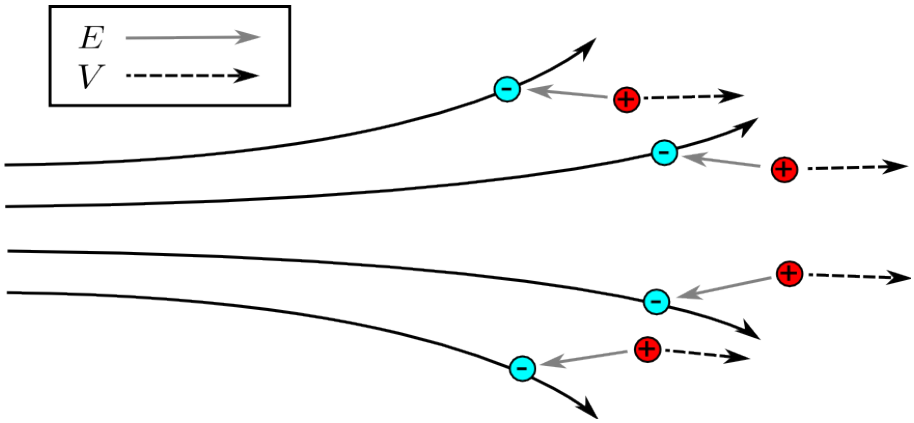

Figure 3.6: Inertial detachment of electron-ion pair

The condition for the detachment of the hybrid Larmor radius particle has been shown in a study by Little et al. to be $G^{-1/2}|\frac{\nabla B}{B}| = .5$. [41] It has also been shown that imposing an initial azimuthal velocity will significantly increase detachment efficiency and decrease nozzle divergence. [50] The analysis by Hooper[26] has been criticized by Ahedo [1] due to the simplifying assumptions made, particularly that of ambipolarity.

Contrary to some theoretical and computational results, some experiments have shown that significant detachment may occur even with only ion demagnetization.[60] Numerical simulations related to VASIMR have also shown detachment occurring due to ion demagnetization.[30] Detachment by inertial means is often referred to as the "lower limit" of detachment which can be enhanced by other detachment mechanisms.

3.2.2.3 Induced Field Detachment

Detachment through the use of induced magnetic fields is possible by stretching the magnetic field lines to infinity or by canceling out the applied fields, thereby

demagnetizing the plasma. Induced field detachment effectiveness can be studied by the currents which create these fields.

Magnetic field stretching occurs when the plasma kinetic energy exceeds the magnetic energy or equivalently when the plasma fluid velocity exceeds the Alfvén velocity. This is characterized by the non-dimensional parameter shown in Equation 3.9.

$$\beta_f = \frac{\rho u^2/2}{(B^2/2\mu_0)} > 1 \tag{3.9}$$

When this condition is satisfied the fluid is considered to be super-Alfvénic and is traveling faster than the rate at which changes in the magnetic field affect the flow. As a result of this behavior, magnetic field lines get dragged to infinity preserving frozen-in flow. [6, 10] The currents required to produce super-Alfvénic detachment are paramagnetic which results in convergent detachment but produce thrust losses due to attractive forces between the applied field and induced field currents.[6, 10, 2] Studies have shown that sub- to super-Alfvénic transition can minimize detachment losses with a slowly diverging magnetic field. An experimental study has suggested detachment behavior due to $B_f > 1$ rather than ion demagnetization and shows agreement with computational results.[19, 20, 10] Field line stretching however could not be measured. Other experimental and computational results have also demonstrated super-Alfvénic detachment and have identified a mechanism for self-collimation of the plasma plume. [64]

The cancellation of the applied field by the induced field is referred to as self-demagnetization and occurs due to the formation of diamagnetic currents in the plasma. These currents create both a radial confining force and an axial accelerating force.[45] The diamagnetic currents that drive this detachment are favorable for mo-

mentum transfer to the spacecraft, but create a magnetic field lines. The configuration of magnetic field lines to achieve this form of detachment are similar to those that would be seen in magnetic reconnection detachment. Self-demagnetization detachment has been demonstrated computationally.[2, 45] Figure 3.7 shows a schematic of possible induced field detachment.

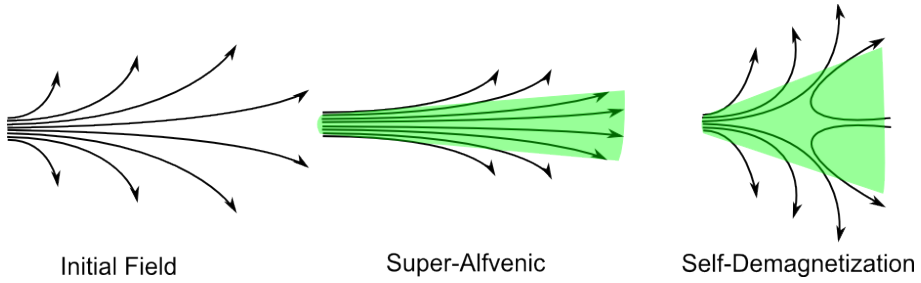

Figure 3.7: Induced field detachment mechanisms

3.2.3 Magnetic Reconnection

Magnetic reconnection is a widely studied problem in plasma physics and astrophyscis but has not been sufficiently studied when relating to plasma propulsion detachment scenarios. Phenomenon exhibiting magnetic reconnection physics relevant to plasma detachment are evident in coronal mass ejections and magnetic confinement fusion experiments.[36]

The most elementary description of magnetic reconnection is shown in Figure 3.8. An initial configuration of two magnetic field lines, (1), has a finite diffusion across the magnetic field lines, (2), which eventually leads the magnetic field lines to tear and reconnect into a new configuration (3) of lower energy. The reconfiguration of the magnetic field lines allows plasma flows which under the previous configuration were not possible. This characteristic of magnetic reconnection is particularly attractive for magnetic nozzle detachment because it allows magnetic islands to form which

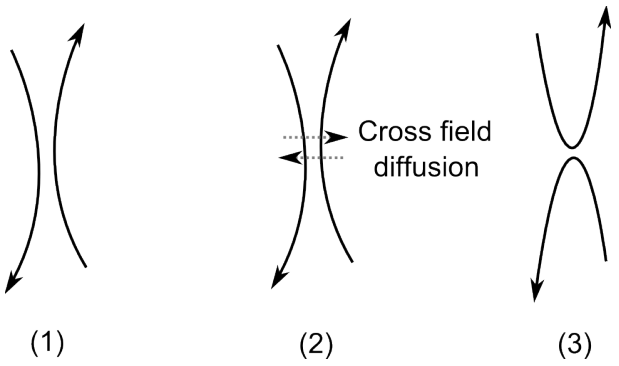

Figure 3.8: Magnetic field line reconnection

separate from the applied field.

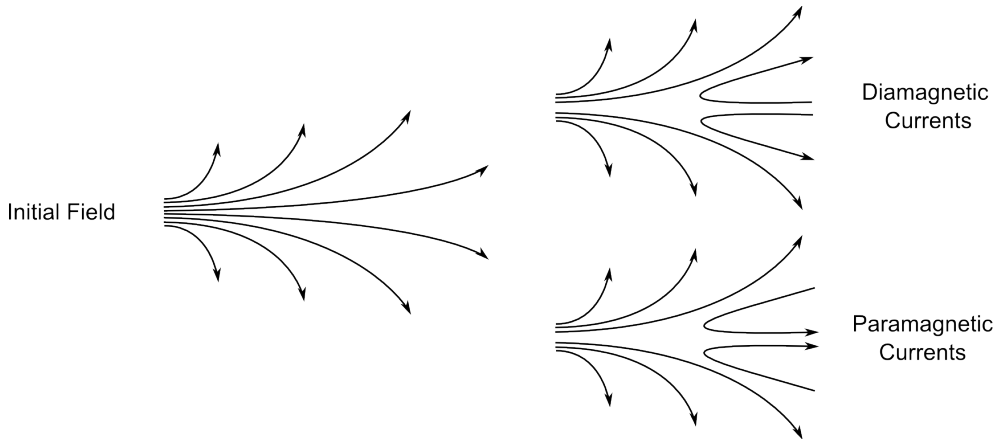

Figure 3.9: Possible magnetic field line reconnection configurations in magnetic nozzles

An example of possible reconnection field configurations in magnetic nozzles is shown in Figure 3.9. The initial field is that of a a dipole or solenoid magnetic field. The magnetic reconnection configuration depends on the strength and direction of the induced field which results from induced currents that may be diamagnetic or paramagnetic. The diamagnetic current configuration is particularly intriguing because the interaction between the applied field currents and the induced field currents would result in a repulsive force which produces thrust. Magnetic reconnection is an

inherently transient phenomenon which requires time-dependent numerical methods to study.

3.3 Momentum Transfer

The momentum change as a result of energy conversion and plasma detachment must be transferred back to the spacecraft to generate thrust. The mechanisms for momentum transfer in the absence of a physical wall are governed by the Lorentz force. Looking specifically at the $J \times B$ terms and assuming non-relativistic flows defines two momentum transfer mechanisms through the magnetic pressure and magnetic field convection.

$$\mathbf{J} \times \mathbf{B} = -\nabla \frac{\mathbf{B}^2}{2\mu_0} + \frac{1}{\mu_0}(\mathbf{B} \cdot \nabla)\mathbf{B} \tag{3.10}$$

As discussed previously the magnetic pressure can confine the plasma and results in the formation of a current layer at the plasma vacuum edge. It has been shown that the forces between the currents induced in the plasma plume and currents which create the magnetic nozzle are the primary mechanisms by which momentum is transfered between the spacecraft and the plasma.[39, 1, 40, 2, 41] Induced currents are created throughout the plume due to the motion of the plasma and are primarily azimuthal due to the axisymmetry of the nozzle. The resulting currents can be either diamagnetic, opposing the applied field, or paramagnetic, increasing the applied field. Diamagnetic currents create a repulsive force which is desirable for thrust while paramagnetic currents create an attractive force resulting in drag on the plasma. Diamagnetic currents create diverging magnetic field lines while paramagnetic currents can produce convergent field lines.

Paramagnetric and diamagnetic currents may exist simultaneously in a plasma due to diamagnetic surface currents and paramagnetic volumetric currents.[2, 40, 41]

To produce thrust under these conditions the force per unit length due to the diamagnetic surface currents must exceed that of the paramagnetic volumetric currents. This relationship has been showed computationally and suggests that thrust generation may occur even in the presence of paramagnetic currents.[41]

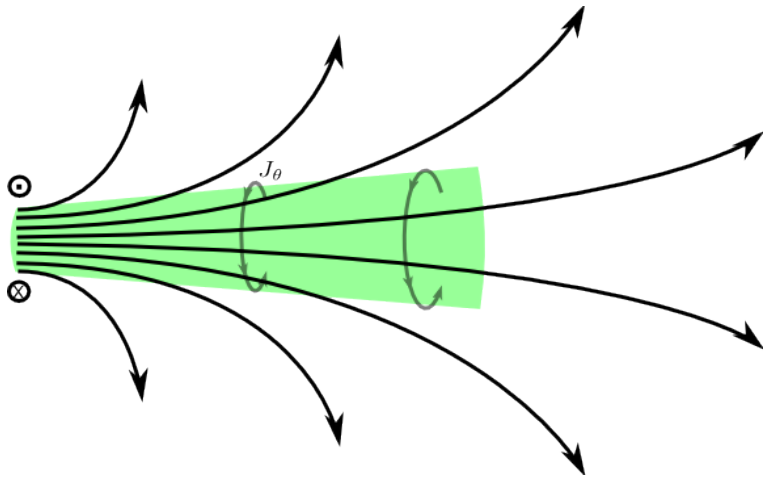

Figure 3.10: Illustration of currents in magnetic nozzle

To provide insight on this process we quote Little et al., "surface currents are induced that effectively act as a magnetic wall that confines the expanding plasma and transmits momentum from the plasma to the applied field coil through their mutual interaction."[41] Thus the notion of the confining magnetic pressure and the induced currents are intimately connected and provide the means for momentum transfer between the spacecraft and the plasma.

3.4 Operating Regimes of Magnetic Nozzles

Numerous physical mechanisms in the thrust generation process have been presented based on a review of magnetic nozzle physics literature. A summary of parameters which characterize some of these physical processes are shown in Table 3.1.

Physical Mechanism	**Parameter**
Adiabaticity	$r_L\|\nabla B\|/\|B\|$
Recombination	ν_{ei}
Confinement by Magnetic Pressure	$\beta_p = \frac{nk_BT}{B^2/2\mu_0}$
Resistive Detachment	$Re_m = UL/\eta$
Inertial Detachment	$\zeta = G^{-1/2}\|\frac{\nabla B}{B}\|$
Super-Alfvénic Detachment	$\beta_k = \rho u^2/(B^2/\mu_0)$

Table 3.1: Dimensionless numbers of physical mechanisms

We have also compiled Table A.1 in the Appendix as a reference to experiments which have studied magnetic nozzle physics. Table A.1 is by no means an exhausted list, but outlines the general parameter regimes in which some typical magnetic nozzle experiments operate. The numbers shown are calculated using equations from the NRL formulary[29] and are based on a single point in the flow. As such, the values throughout the nozzle may easily vary by an order of magnitude. Two cases for the VASIMR experiments are shown with the (DS) case denoting a point further downstream the nozzle. The table is included to give a general idea of the regimes and how they vary between magnetic nozzle propulsion devices and brief comments about each are given in the following subsections.

3.4.1 Variable Specific Impulse Magnetoplasma Rocket

The VASIMR experiment heats the ions by Ion Cyclotron Resonance Heating (ICRH) which then enter a magnetic nozzle configuration. Energy conversion by the conservation of the adiabatic invariant and ambipolar acceleration has been shown. [13, 5, 42, 57] Detachment has been demonstrated and the responsible mechanism is currently being determined. [57] Efficiency and thrust of the device have been determined and show encouraging results. [43]

3.4.2 High Power Helicon

The High Power Helicon (HPH) is an experiment performed by Winglee et al.[64] in which a plasma produced by a helicon source flows through a magnetic nozzle. This experiment showed both collimation of the plasma plume by a magnetic nozzle and self-collimation due to super-Alfvénic flow. The acceleration of the plasma in the nozzle was attributed to directionalizing of thermal energy.

3.4.3 Detachment Demonstration Experiment

The Detachment Demonstration EXperiment (DDEX) studied plasma produced by a pulsed plasma washer gun under the influence of a magnetic nozzle.[18, 19, 20] Detachment was demonstrated, suggesting super-Alfvénic detachment as the driving mechanism. Super-Alfvénic flow, $\beta_f > 1$, is shown at the detachment location, but field line stretching was not measured.

3.4.4 Helicon Double Layer Thruster

The Helicon Double Layer Thruster (HDLT) produces plasma by a helicon source which expands into a magnetic nozzle configuration. [63] Energy is transfered to the ions by the formation of a current-free electric double layer. Detachment is predicted due to ion demagnetization.

3.4.5 Kuriki Arc Heater

The Kuriki Arc Heater (KAH) experiment studies the flow of an arc heated plasma in a converging-diverging magnetic nozzle. [38] The plasma is shown to be significantly accelerated by both electric field forces and thermal energy directionalization. An energy equation is suggested that couples ion and electron energies through the electric potential. Detachment is not significantly addressed.

3.4.6 Magnetoplasmadynamic Arcjet

The MagnetoPlasmaDynamic Arcjet (MPDA) experiment studies the flow MPD exhaust under the influence of a magnetic nozzle. [32, 31] Results suggest energy conversion governed by isentropic expansion processes and not conservation of the magnetic moment. Plasma flow velocity and Mach number increase downstream as the ion temperature decreases.

3.5 Summary

Theoretical and computational work have defined a variety of physical mechanisms that can be used to accelerate and detach plasma in magnetic nozzles. Experiments have confirmed acceleration and detachment, but questions still remain as to which of the proposed mechanisms are responsible for this behavior. To proceed further experiments must determine which of the presented theoretical and experimental mechanisms are dominant in regimes relevant to plasma propulsion. Establishing which physical mechanisms are dominant will allow theory to predict the behavior of plasma within this regime. If the predicted behavior is confirmed by additional experiments the physics of magnetic nozzles will be sufficiently understood for design optimization. The convergence of experimental and theoretical results is crucial to the understanding of magnetic nozzles.

4. MAGNETOHYDRODYNAMICS AND MAGNETIC NOZZLE PHYSICS

The relevance of MHD to studying magnetic nozzle plasma physics must be established to justify studying magnetic nozzles with an MHD computational method. Therefore, we performed an order of magnitude analysis to determine the validity of continuum and MHD assumptions within the regimes in which magnetic nozzles operate.[22].

4.1 Validity of Continuum Assumptions for Magnetic Nozzle Physics

The validity of continuum assumptions must be evaluated in the operating regimes of magnetic nozzles in order to justify use of a fluid model such as MHD for computational studies. The Knudsen number, $Kn = \lambda/L$, is typically used for this purpose. For approximately $Kn < .1$ continuum assumptions may be considered valid. To calculate the Knudsen number the mean free paths of particles in a plasma must be determined. Particle mean free paths in plasmas are much more complex than in non-conducting fluids and is best illustrated by Figure 4.1.

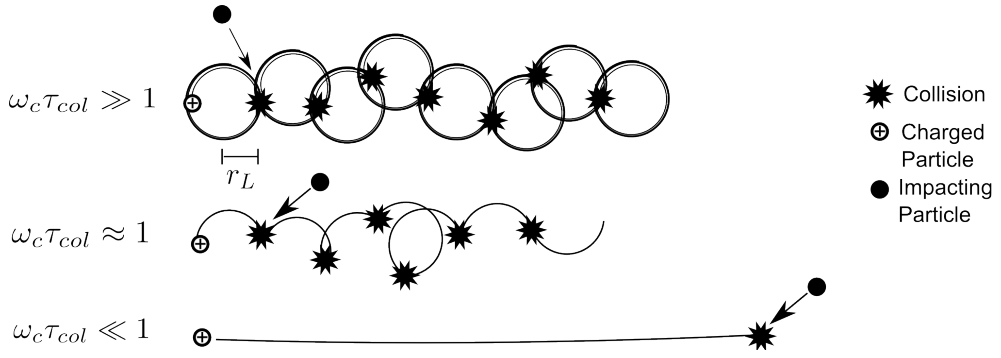

Figure 4.1: Mean free path in plasmas

Braginskii[9] suggests that the mean free path of charged particles can vary depending on the strength of the magnetic field acting on them. The strength of the

magnetic field is typically characterized by the Hall parameter, $\alpha = w_c \tau_{col}$. In strong magnetic fields, $\alpha \gg 1$, the farthest distance a particle can travel between collisions is on the order of the Larmor radius, therefore $\lambda_p \approx r_L$. For intermediate strength fields, $\alpha \approx 1$, a hybrid mean free path is defined as $\lambda_p \approx \sqrt{r_L \lambda}$. Finally for weak magnetic fields, $\alpha \ll 1$, the mean free path returns to its non-conducting fluid form of $\lambda_p = \lambda$. It is important to note that these newly defined mean free paths are valid for directions perpendicular to the magnetic field and that the conventional mean free path must still be used in the direction parallel to the field.

Transport properties involving momentum, such as viscosity, are determined by ion collisions while transport properties for internal energy and electromagnetic fields, such as thermal conductivity and electrical conductivity, are determined by electron collisions. This implies that the validity of each transport coefficient is determined by the Knudsen numbers of the individual species. Taking this into consideration we calculated Knudsen numbers according to Braginskii's convention for a number of experimental setups which incorporate magnetic nozzles. The results are shown in Table 4.1 in which the relevant values for the perpendicular field direction are highlighted. Again two cases are shown for VASIMR with (DS) denoting a point further down stream in the flow.

	Experiments						
	VASIMR[4]	**VASIMR(DS)**	**HPH**[64]	**DDEX**[20]	**HDLT**[63]	**KAH**[38]	**MPDA**[31]
Ion Hall #	4.53E+01	2.51E+00	8.29E-01	5.73E+00	5.15E-01	4.99E-03	5.47E+00
Electron Hall #	4.56E+02	4.66E+02	9.70E+01	3.35E+02	8.35E+03	5.84E+00	1.85E+02
Ion Knudsen #	3.77E+00	4.55E-01	1.09E-01	6.70E-02	7.20E-01	**2.55E-04**	1.09E+00
Electron Knudsen #	4.84E-02	3.11E-01	7.41E-02	4.56E-02	2.25E+02	2.46E-03	3.42E-01
Ion Hybrid	5.60E-01	**2.86E-01**	**1.19E-01**	**2.80E-02**	**1.00E+00**	3.61E-03	**4.63E-01**
Electron Hybrid	2.27E-03	1.44E-02	7.52E-03	2.49E-03	2.47E+00	**1.02E-03**	2.53E-02
Ion Strong Field	**8.30E-02**	1.80E-01	1.31E-01	1.17E-02	1.39E+00	5.10E-02	1.98E-01
Electron Strong Field	**1.06E-04**	**6.66E-04**	**7.63E-04**	**1.36E-04**	**2.70E-02**	4.21E-04	**1.87E-03**

Table 4.1: Knudsen numbers in magnetic nozzles

The results in Table 4.1 indicate that for most experimental setups continuum

assumptions are valid in the direction perpendicular to the magnetic field. The ion Knudsen number in the parallel field direction is the primary condition that violates continuum assumptions. This implies that the viscous transport in the parallel field direction would be the primary source of error when using a continuum model for these flows. This can be corrected by introducing more complex transport coefficients. Viscous transport, although important, is not the primary physics of interest in magnetic nozzles. Furthermore, the value of transport coefficients in plasmas is not clearly defined due to the difficulty in measuring these quantities accurately, allowing flexibility in choosing these values.

The primary conclusion drawn from Table 4.1 is that the operating regime of magnetic nozzles is on edge of validity for continuum solvers and this must be kept in mind when performing computational studies. It is also worth noting that the Knudsen number values may be different by assuming a different arbitrary characteristic length, we used plume diameter, or by considering a different portion of the plasma plume, we primarily used values near the nozzle throat or centerline which admittedly are more favorable for determining the validity of a continuum. Finally it must be stressed that the continuum assumptions only relate to the relevance of the transport properties, the overall conservation equations are valid even if continuum assumptions are not satisfied.

4.2 Order of Magnitude Analysis of Magnetic Nozzle Physics

To determine the type of MHD solver necessary to study magnetic nozzle physics we performed a parametric analysis of the generalized Ohm's law, Equation (5.31), for a number of experiments.[4, 64, 20, 63, 38, 31]

$$\mathbf{E} = -\mathbf{U} \times \mathbf{B} + \frac{1}{n_e q}\mathbf{J} \times \mathbf{B} - \frac{1}{n_e e}\nabla(n_e k T_e) + \eta \mathbf{J} \tag{4.1}$$

The terms on the right side of (5.31) will be referred to as the convective, Hall, electron pressure, and resistive terms respectively. To maintain a single fluid model the plasma is assumed to be quasi-neutral ($n_i = n_e$) and single temperature ($T_i = T_e$). Table 4.2 shows the results of the parametric analysis. Note that these ratios are calculated primarily using data near the nozzle throat where the magnetic field is strongest.

		Experiments						
Ratio of Terms	**Equation**	**VASIMR**	**VASIMR(DS)**	**HPH**	**DDEX**	**HDLT**	**KAH**	**MPDA**
MHD Assumption	ω_{ce}/ω	$\approx 10^5$	$\approx 10^5$	$\approx 10^5$	$\approx 10^5$	$\approx 10^3$	$\approx 10^5$	$\approx 10^4$
Hall/Convective	ω/ω_{ci}	$\approx 10^{-1}$	$\approx 10^0$	$\approx 10^{-1}$	$\approx 10^{-2}$	$\approx 10^1$	$\approx 10^{-1}$	$\approx 10^{-1}$
Resistive/Convective	$1/Rm$	$\approx 10^{-3}$	$\approx 10^{-3}$	$\approx 10^{-2}$	$\approx 10^{-2}$	$\approx 10^{-1}$	$\approx 10^1$	$\approx 10^{-2}$
Hall/Resistive	ω_{ce}/ν_{ei}	$\approx 10^2$	$\approx 10^2$	$\approx 10^2$	$\approx 10^2$	$\approx 10^3$	$\approx 10^0$	$\approx 10^2$
Hall/Electron Pressure	p_B/p_e	$\approx 10^1$	$\approx 10^1$	$\approx 10^1$	$\approx 10^2$	$\approx 10^4$	$\approx 10^3$	$\approx 10^1$
Electron Pres./Convective	$p_e\omega/p_B\omega_{ci}$	$\approx 10^{-2}$	$\approx 10^{-1}$	$\approx 10^{-2}$	$\approx 10^{-4}$	$\approx 10^{-3}$	$\approx 10^{-4}$	$\approx 10^{-2}$

Table 4.2: Parametric analysis

The parametric analysis shows that the primary assumption for simplifying the electron equation of motion into the generalized Ohm's law is satisfied in all systems analyzed. The analysis also shows that Hall term effects must be included. The resistive term appears to be small compared to the convective and Hall terms in most cases, but is incorporated to eliminate numerical stiffness, include MHD turbulence effects, and account for the contribution of cross field diffusion to detachment. Additionally, experiments have shown cross field diffusion to be much greater than expected due to anomalous resistivity, which may be incorporated in the future[11]. The electron pressure term is found to be important in some cases, but negligible in most. This term is included primarily for completeness of the model. In summary, we have shown that the generalized Ohm's law is necessary to capture the relevant physics of magnetic nozzles. Similar results were found in a study by Araya[4] which suggests the use of Hall MHD with tensorial transport properties to study the VASIMR propulsion system.

5. SOLVER DEVELOPMENT

5.1 Introduction

This chapters discusses the theory and implementation of the Magnetohydrodynamic Gas Kinetic Method (MGKM). An overview of the Gas Kinetic Method (GKM) will be given along with the necessary changes to develop MGKM. The Gas Kinetic Method was initially developed by Kun Xu. [65] It has since been developed further by the Turbulence Research Group at TAMU under Sharath Girimaji to perform Direct Numerical Simulation (DNS) of turbulence.[35] It has been shown to be a robust solver and has been extensively used to study Navier-Stokes flows.

5.2 The Gas Kinetic Method

5.2.1 GKM Overview

GKM is a finite volume numerical scheme that solves the Navier-Stokes equations using a combination of fluid and kinetic theory methods. The fluid part of the method involves updating cell-centered macroscopic properties such as density and momentum through calculating fluxes at the cell interface. The kinetic theory portion determines how these fluxes are calculated.

The basic structure of GKM can be organized into three stages: reconstruction, gas evolution, and projection. During the reconstruction stage a piecewise continuous function connecting the cell centered macroscopic flow values is created. In the gas evolution stage fluxes are calculated at the cell interfaces based on the Boltzmann BGK equation which is defined by the interpolated macroscopic flow variables. Finally during the projection stage the new macroscopic flow values at the cell centers are calculated based on the fluxes.

To find new cell-centered values of the macroscopic quantities the governing equation for GKM has to be solved. This equation, Equation 5.1, is shown below and represents the change of the macroscopic property in time due to fluxes through the cell interfaces.

$$\frac{\partial}{\partial t}\int_{\Omega} U\, d\mathbf{x} + \oint_{A} \mathbf{F}\cdot\, d\mathbf{A} = 0 \tag{5.1}$$

In this equation Ω is the control volume, A is the surface of the control volume, and $\mathbf{F} = \mathbf{F}(\overrightarrow{x}, t) = F_1\hat{i} + F_2\hat{j} + F_3\hat{k}$ is the flux. To give an example of how this equation may be solved we show a brief derivation in 1D. Equation 5.2 is the 1D version of Equation 5.1. The fluxes in Equation 5.2 are defined in Equation 5.3.

$$\frac{\partial}{\partial t}\int_{\triangle x} U\, dx + \Big(F_1(x_{j+\frac{1}{2}}, t) - F_1(x_{j-\frac{1}{2}}, t)\Big) = 0 \tag{5.2}$$

$$F_1 = [F_\rho, F_{\rho u_1}, F_E]^T = \int_{-\infty}^{\infty} v_1 \psi f(x_1, t, v_1, \xi)\, d\Xi \tag{5.3}$$

From a computational standpoint, Equation 5.2 should be integrated over a single time step to find Equation 5.4.

$$U(t+\triangle t) - U(t) = -\frac{1}{\triangle x}\int_{t}^{t+\triangle t}\Big(F_1(x_{j+\frac{1}{2}}, t) - F_1(x_{j-\frac{1}{2}}, t)\Big)\, dt \tag{5.4}$$

Equation 5.4 is the useful form of the governing equation for the 1D GKM and is discretized in Equation 5.5.

$$U_j^{n+1} = U_j^n - \frac{1}{x_{j+\frac{1}{2}} - x_{j-\frac{1}{2}}}\int_{t}^{t+\triangle t}(F_{j+\frac{1}{2}}(t) - F_{j-\frac{1}{2}}(t))\, dt \tag{5.5}$$

The individual stages of reconstruction, gas evolution, and projection which are

necessary to solve this governing equation are discussed in the following sub-sections.

5.2.2 Reconstruction

The reconstruction stage is defined as the stage in which piecewise continuous functions of flow variables are obtained inside each cell to connect the cell-centered values with one another. This step is necessary so that the quantities needed to calculate the fluxes at the boundary can be found. These piecewise continuous functions are constructed by limiters which are used because simple polynomials may generate oscillations if large gradients, such as shocks, exist in the flow [65]. Limiters detect these large gradients and better resolve them while preventing the oscillations. The specific limiter used by our solver is known as WENO (Weighted Essentially Non-Oscillatory) and is widely used in shock capturing schemes. After reconstruction is completed, macroscopic properties are defined at the cell interfaces with respect to the right and left cell centers around the interface. The values found to the left and right of the interface are not necessarily the same number and can not simply be averaged to find a single number at the interface.

5.2.3 Gas Evolution

The gas evolution phase is arguably the defining stage of GKM. The purpose of the gas evolution phase is to calculate the fluxes at the interfaces. To achieve this the distribution function, f, must be known at the interfaces defined by the x locations $x_{j-\frac{1}{2}}$ and $x_{j+\frac{1}{2}}$ at time t. To find this the formal integral solution of the Boltzmann BGK equation must be found. We will be following the description of this stage presented by Xu.[65] The general solution for this equation at the cell interface $x_{j+1/2}$ at time t is shown in Equation 5.6.

$$f(x_{i+1/2},t,v_1,v_2,v_3,\xi)=\frac{1}{\tau}\int_0^t g(x_1',t',v_1,v_2,v_3,\xi)e^{-(t-t')/\tau}\,dt'+e^{-t/\tau}f_0(x_{i+1/2}-v_1t) \tag{5.6}$$

In this equation $x'=x_{j+1/2}-v_1(t-t')$ is the trajectory of the particle, f_0 is the initial distribution function, and g is the equilibrium distribution function. This equation identifies two unknowns g and f_0 which must be determined to fully define f. Following the notation of Xu, $x_{j+1/2}=0$ will be used from now on. The equations for g and f_0 are modeled as first-order expansions of the local equilibrium distribution and are shown in Equations 5.7 and 5.8. The superscripts l,r refer to the left and right side of the cell interface respectively.

$$f_0(x)=\begin{cases} g^l[1+a^lx-\tau(a^lv_1+A^l)], & x\le 0 \\ g^r[1+a^rx-\tau(a^rv_1+A^r)], & x\ge 0 \end{cases} \tag{5.7}$$

$$g(x)=\begin{cases} g_0[1+\overline{a}^lx+\overline{A}t], & x<0 \\ g_0[1+\overline{a}^rx+\overline{A}t], & x\ge 0 \end{cases} \tag{5.8}$$

The variables $a^{l,r}$, $A^{l,r}$, $\overline{a}^{l,r}$, and $\overline{A}^{l,r}$ are slopes related to the Maxwellian and are defined by Equations 5.9 and 5.10.

$$\overline{A}=\frac{\partial \ln g_0}{\partial t} \qquad \overline{a}^{l,r}=\nabla \ln g_0 \tag{5.9}$$

$$A^{l,r}=\frac{\partial \ln g^{l,r}}{\partial t} \qquad a^{l,r}=\nabla \ln g_{l,r} \tag{5.10}$$

These slopes may also be expressed in the form of Equation 5.11.

$$a^{l,r} = a_1^{l,r} + a_2^{l,r} v_1 + a_3^{l,r} v_2 + a_4^{l,r} v_3 + a_5^{l,r} \frac{1}{2}(v_1^2 + v_2^2 + v_3^2 + \xi^2) = a_\alpha^{l,r} \psi_\alpha \tag{5.11}$$

Equation 5.7 is found from a combination of the first order Chapman-Enskog expansion, shown in equation 5.12, and a Taylor series expansion. Equation 5.8 is simply a Taylor series expansion.

$$f = g - \tau(g_t + u g_x) \tag{5.12}$$

Note that for 1-D the ∇ becomes $\frac{\partial}{\partial x}$. The additional terms due to the Chapman-Enskog expansion account for the nonequilibrium states and the deviation of the distribution function away from the Maxwellian. The gas is out of equilibrium due to spatial distributions of macroscopic quantities. These nonequilibrium parts have no direct contribution to the conserved variables, which is shown mathematically in Equation 5.13. The Chapman-Enskog terms simply change the shape of the Maxwellian but the integration should produce the same macroscopic quantities to satisfy conservation relations.

$$\int (a^{l,r} + A^{l,r}) \psi g^{l,r} d\Xi = 0 \tag{5.13}$$

The Maxwellian distributions, g^l, g^r, and g_0 are defined in Equations 5.14.

$$g^l = \rho^l \left(\frac{\lambda^l}{\pi}\right)^{\frac{K+3}{2}} e^{-\lambda^l[(v_1-u_1^l)^2+(v_2-u_2^l)^2+(v_3-u_3^l)^2+\xi^2]}$$

$$g^r = \rho^r \left(\frac{\lambda^r}{\pi}\right)^{\frac{K+3}{2}} e^{-\lambda^r[(v_1-u_1^r)^2+(v_2-u_2^r)^2+(v_3-u_3^r)^2+\xi^2]} \tag{5.14}$$

$$g_0 = \rho_0 \left(\frac{\lambda_0}{\pi}\right)^{\frac{K+3}{2}} e^{-\lambda_0[(v_1-u_{1_0})^2+(v_2-u_{2_0})^2+(v_3-u_{3_0})^2+\xi^2]}$$

The function g_0 is a local Maxwellian distribution function located at $x = 0$, the cell interface. The function g is continuous at $x = 0$, but has different slopes for $x < 0$ and $x > 0$. The function f_0 is piecewise continuous at $x = 0$, but it also has different slopes for $x < 0$ and $x > 0$. Figure 5.1 shows f_0 and $g^{l,r}$ pictorially. As will be shown later, g is evaluated from f_0. The final gas distribution, f, at the cell interface $x_{i+\frac{1}{2}}$ is a nonlinear combination of both f_0 and g.

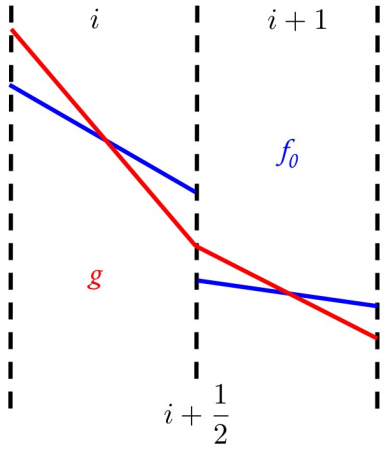

Figure 5.1: Graphical representation of the spacial distribution of the initial state f_0 and the equilibrium distribution g at $t = 0$.[3]

The macroscopic variables necessary to determine the distribution functions of Equation 5.14 are found at the cell interfaces through the reconstruction phase. The functions g^l and g^r are fully defined and are used to determine the the slopes in

Equations 5.15-5.17. These equations relate a Taylor Series expansion for Ψ to the expansion for f_0. As shown previously $\Psi = (\rho, \rho u, ..., e)$.

$$\Psi = \begin{cases} \Psi^l + \frac{\partial \Psi^l}{\partial x} x, & x \leq 0 \\ \Psi^r + \frac{\partial \Psi^r}{\partial x} x, & x \geq 0 \end{cases} \tag{5.15}$$

$$\Psi^l + \frac{\partial \Psi^l}{\partial x} x + ... = \int_{-\infty}^{\infty} g^l (1 + a^l x) \psi_\alpha \, d\Xi \tag{5.16}$$

$$\Psi^r + \frac{\partial \Psi^r}{\partial x} x + ... = \int_{-\infty}^{\infty} g^r (1 + a^r x) \psi_\alpha \, d\Xi \tag{5.17}$$

The Chapman-Enksog terms are ignored because their integration equals zero due to the conservation of the macroscopic quantities. Comparing coefficients of x leads to Equations 5.18 and 5.19.

$$\Psi^l = \int_{-\infty}^{\infty} g^l \psi_\alpha \, d\Xi \qquad \frac{\partial \Psi^l}{\partial x} = \int_{-\infty}^{\infty} g^l a^l \psi_\alpha \, d\Xi \tag{5.18}$$

$$\Psi^r = \int_{-\infty}^{\infty} g^r \psi_\alpha \, d\Xi \qquad \frac{\partial \Psi^r}{\partial x} = \int_{-\infty}^{\infty} g^r a^r \psi_\alpha \, d\Xi \tag{5.19}$$

These equations are then rewritten with the previous expansions of a^l and a^r to give the relations in Equation 5.20 and 5.21.

$$\frac{\partial U^l}{\partial x} = \int_{-\infty}^{\infty} \psi_\alpha g^l a^l_\beta \psi_\beta \, d\Xi = a^l_\beta \int_{-\infty}^{\infty} g^l \psi_\alpha \psi_\beta \, d\Xi \tag{5.20}$$

$$\frac{\partial U^r}{\partial x} = \int_{-\infty}^{\infty} \psi_\alpha g^r a^r_\beta \psi_\beta \, d\Xi = a^r_\beta \int_{-\infty}^{\infty} g^r \psi_\alpha \psi_\beta \, d\Xi \tag{5.21}$$

A matrix $M_{\alpha\beta}$ is defined in Equation 5.22 to solve this system of equations. This

matrix is simply set of the different moments of the Maxwellian. These terms are obtained analytically.

$$M_{\alpha\beta}^{l,r} = \frac{1}{\rho^{l,r}} \int_{-\infty}^{\infty} g^{l,r} \psi_\alpha \psi_\beta \, d\Xi \tag{5.22}$$

The slopes $A^{l,r}$ are then also found by satisfying the zero contribution relation of the Chapman-Enksog terms in Equation 5.13. The macroscopic variables necessary to determine the function g_0 are found by the relation in Equation 5.23 which relates the equilibrium distribution functions to the left and right of an x interface to the conservative variables at $t = 0$.

$$\int g_0 \psi_\alpha \, d\Xi = \Psi^0 = \int_{v_1>0} g^l \psi_\alpha \, d\Xi + \int_{v_1<0} g^r \psi_\alpha \, d\Xi \tag{5.23}$$

The slopes $\overline{a}^{l,r}$ are obtained through a relation similar to that described for $a^{l,r}$ in which a new matrix $\overline{M}_{\alpha\beta}^{0}$ is defined with slopes related to the Ψ^0 variables. The only unknown that remains is $\overline{A}$ which is determined by the overall conservation constraint shown in Equation 5.24.

$$\int_0^{\triangle t} \int (g - f) \psi_\alpha \, dt d\Xi = 0 \tag{5.24}$$

At this point all the necessary slopes to fully define f_0 and g have been found. These distribution functions then fully describe f at the cell interface, which can then be used to calculate the necessary fluxes.

5.2.4 Projection

In the projection stage the cell centered values for mass, momentum, and energy are updated at the cell-centers. This is done by using Equation 5.5 rewritten in Equation 5.25.

$$\Psi_j^{n+1} = \Psi_j^n - \frac{1}{x_{j+\frac{1}{2}} - x_{j-\frac{1}{2}}} \int_t^{t+\triangle t} (F_{j+\frac{1}{2}}(t) - F_{j-\frac{1}{2}}(t))\, dt \tag{5.25}$$

Note that in this implementation of GKM the integrals over time have already been evaluated in the gas evolution phase.

5.3 Generalized Ohm's Law GKM Solver

The MGKM solver consists of a "fluid" portion that numerically solves the Navier Stokes equations through the Gas Kinetic Method (GKM)[65, 35] and "magnetic" portion that incorporates MHD physics through source terms to the conserved fluid variables.[3] These sources appear in the projection stage of the original GKM. A generalized Ohm's law and Maxwell's equations are used to close the system of MHD equations and self-consistently calculate the induced magnetic field. The system of equations is shown below with the "fluid" portion on the left side and the "magnetic" portion on the right side of the conservation equations.

$$\frac{\partial \rho}{\partial t} + \nabla \cdot (\rho \mathbf{U}) = 0 \tag{5.26}$$

$$\frac{\partial (\rho \mathbf{U})}{\partial t} + \nabla \cdot \left[\rho \mathbf{U}\mathbf{U} + \underline{\underline{\tau}} + \underline{\underline{I}} p\right] = \mathbf{J} \times \mathbf{B} \tag{5.27}$$

$$\frac{\partial e}{\partial t} + \nabla \cdot \left[\mathbf{U}(e+p) - k\nabla T + \mathbf{U} \cdot \underline{\underline{\tau}}\right] = \mathbf{J} \cdot \mathbf{E} \tag{5.28}$$

$$\mathbf{J} = \frac{\nabla \times \mathbf{B}}{\mu_0} \tag{5.29}$$

$$\frac{\partial \mathbf{B}}{\partial t} = -\nabla \times \mathbf{E} \tag{5.30}$$

$$\mathbf{E} = -\mathbf{U} \times \mathbf{B} + \frac{1}{n_e q}\mathbf{J} \times \mathbf{B} - \frac{1}{n_e e}\nabla(n_e k T_e) + \eta \mathbf{J} \tag{5.31}$$

In the these equations $\underline{\underline{\tau}}$ is the dissipative stress tensor and e is the hydrodynamic energy, $e = \rho U^2/2 + p/(\gamma - 1)$. To maintain a single fluid model the plasma is assumed to be quasi-neutral ($n_i = n_e$) and single temperature ($T_i = T_e$).

The source terms on the right of the conservation equations are discretized according to second-order finite differencing. The contributions of these terms to the conserved flow variables is then added through first order forward time differencing on the same order as GKM. Numerically we did not neglect terms which satisfied $\nabla \cdot B = 0$ in order to include the 8-wave formulation[61] which should propagate numerical errors in $\nabla \cdot B = 0$ with the flow.

GKM was developed initially as a Navier Stokes solver by Xu[65] and was adapted into a resistive MHD solver by Araya.[3] We have further developed MGKM to incorporate the generalized Ohm's law in order to capture the relevant physics of magnetic nozzles. Validation test cases for the resistive and generalized Ohm's law solver are presented in the next chapter.

5.4 Sub-cycling Hall Effect

The characteristic velocities of Hall MHD for a numerical test case of the VASIMR propulsion system are shown in Table 5.1. Incorporation of the Hall term introduces the Whistler wave characteristic which is the most restrictive for determining time step size. Time steps that are two to three orders of magnitude smaller than those for resistive MHD result from the typical grid sizes of $10^{-2} - 10^{-1}$ (m). This results in significant increases in computational effort.

This problem is addressed in our solver through sub-cycling the Hall term effects through intermediate time stepping.[28] The Hall term lends itself well to sub-cycling

Characteristic	Equation	Approximate Values (m/s)
Fluid	U	$\approx 2 \cdot 10^4$
Alfvén (V_A)	$B/\sqrt{\rho\mu_0}$	$\approx 6 \cdot 10^4$
Magnetosonic (V_M)	$\sqrt{V_A^2 + C_s^2}$	$\approx 6 \cdot 10^4$
Hall Velocity	J/ne	–
Hall Drift Velocity	$\frac{B_0}{n^2 e \mu_0} \frac{\partial n}{\partial x}$	–
Whistler Wave (V_W)	kV_A^2/ω_{ci}	$\approx 2 \cdot 10^5/(\Delta x)$

Table 5.1: MHD characteristic velocities based on VASIMR

because it is isolated in changing only the magnetic field while it is a strong function of the magnetic field and magnetic field gradients. To sub-cycle the Hall effect the contributions due to the Hall term are solved on their own time step. The Hall effect is solved for time steps Δt_{Hall} until $\Delta t_{resistive}$ is reached at which the result of the Hall time stepping is used to advance the rest of the scheme. This method is shown graphically in Figure 5.2. This type of solver is valid if the remainder of the flow effects are assumed to be stationary on the Hall time scale.

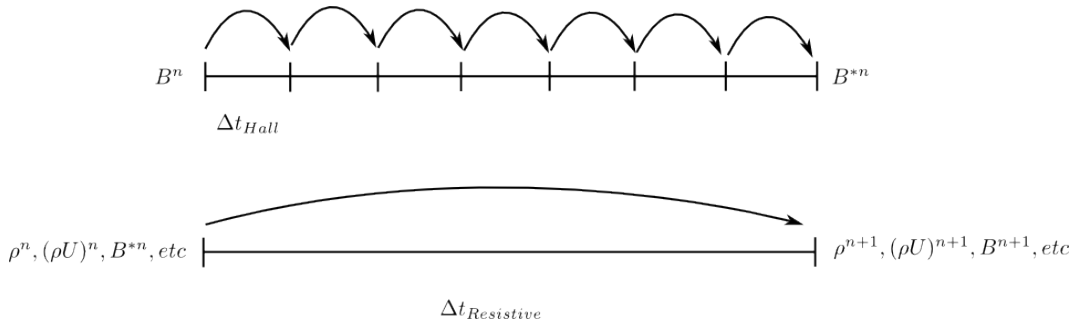

Figure 5.2: Graphical representation of sub-cycling.

Test cases with and without sub-cycling showed negligible differences in results while significantly decreasing computational time. Figure 5.3 shows the time taken per iteration and then what would be the equivalent time taken per iteration. Including sub-cycling increases the time taken per global iteration, but a new equivalent time per iteration is used which takes into account that multiple intermediate itera-

tions of the Hall term are occurring with each global time step. The equivalent time step is found by dividing the global time step by the number of sub-cycle iterations and is what should be compared. Figure 5.4 shows the relative speed up when comparing the equivalent time steps. The data shown in Figures 5.3 and 5.4 are from Hall MHD shock-tube runs.

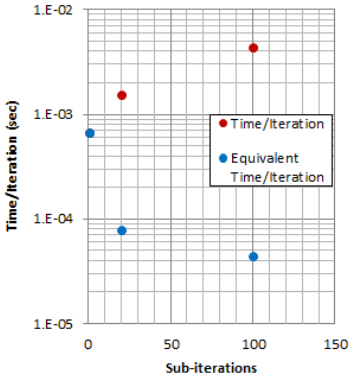

Figure 5.3: Time per iteration and equivalent time per iteration with sub-cycling

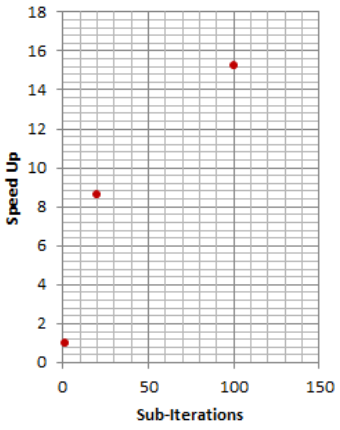

Figure 5.4: Speed up with sub-cycling

5.5 Future Work

Computational challenges currently exist for studying the more complex magnetic nozzle flows and will be addressed in future work. The lack of an explicit way in MHD to satisfy the Maxwell's equation requiring $\nabla \cdot \mathbf{B} = 0$ also presents a computational challenge. This condition is analytically satisfied for all time if is initially satisfied, but numerical errors violating this condition have the potential for unmitigated growth due to the lack of an equation enforcing it. We have a method implemented in our solver which should alleviate this numerical error, but have found that strong shocks cause this method to fail. A number of numerical methods which address this error will be considered in the future.[61] Fluid expansion into a vacuum is also numerically challenging due to the formation of steep gradients and shocks that may lead the numerical method to produce negative densities and temperatures. This problem may be resolved in the future through the use of logarithmic variables [53]or a multi-fluid GKM solver. Further suggestions are discussed in the conclusion chapter.

6. SOLVER VALIDATION

6.1 Introduction

The resistive MGKM solver has been previously validated by Araya.[3] The validation test cases consisted of 2D channel flows and resistive MHD jets. Among the channel flows studied were Hartmann flows and Couette flows. The resistive MHD jet cases studied were in the parameter regime of liquid metal jets and demonstrated stretching of the laminar round jet when subjected to a magnetic field perpendicular to the flow direction. Araya showed very good agreement with the predictions of Davidson [17] who analytically studied this problem and predicted the jet stretching phenomenon.

To expand on these initial validation cases we have studied 1D MHD shock-tube flows as well as Hartmann channel flows with the addition of the Hall effect. These test cases have further validated the solver in the compressible and Hall effect regimes.

6.2 MHD Shock-tube

The MHD shock-tube test case is a one dimensional problem that studies the interaction between a high pressure region and low pressure region separated initially by a current layer. The parameters used for our test cases are equivalent to those used by Brio-Wu [12] which are closely related to those studied by Sod.[56] A graphical representation of the test case is shown in Figure 6.1 in which $\hat{x}$ is the direction of propagation. Note the the magnetic field is non-dimensionalized in Figure 6.1. The original Brio-Wu test case does not include the Hall effect.

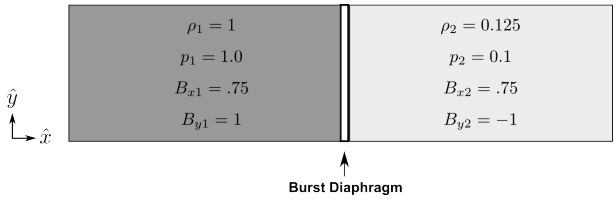

Figure 6.1: One dimensional MHD shock-tube setup

6.2.1 Ideal MHD Shock-tube

The MHD shock-tube problem was first studied without Hall effects to compare directly with the results of Brio-Wu. The results for the density variation in the domain are compared side-by-side in Figure 6.2. Our computational results showed very good agreement when running to an equivalent total time. Our solver showed the same fast rarefraction wave (FR), slow compound wave (SM), contact discontinuity (C), and slow shock (SS) structure. It is important to note here that the major difference between MHD shock-tube problems and Navier Stokes shock-tube problems is the formation of the slow compound wave in MHD shocks. Additional comparison with Brio-Wu's results are shown in Figures 6.3 and 6.4.

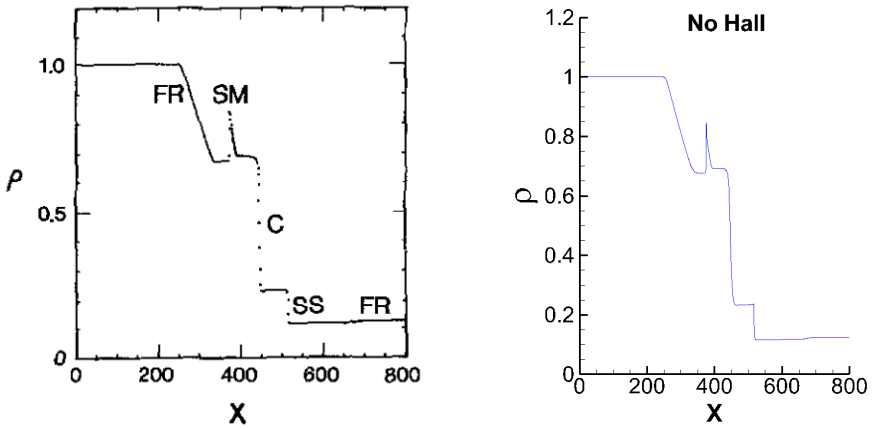

Figure 6.2: Left: Brio-Wu Ideal MHD results [12], Right: MGKM Ideal MHD results

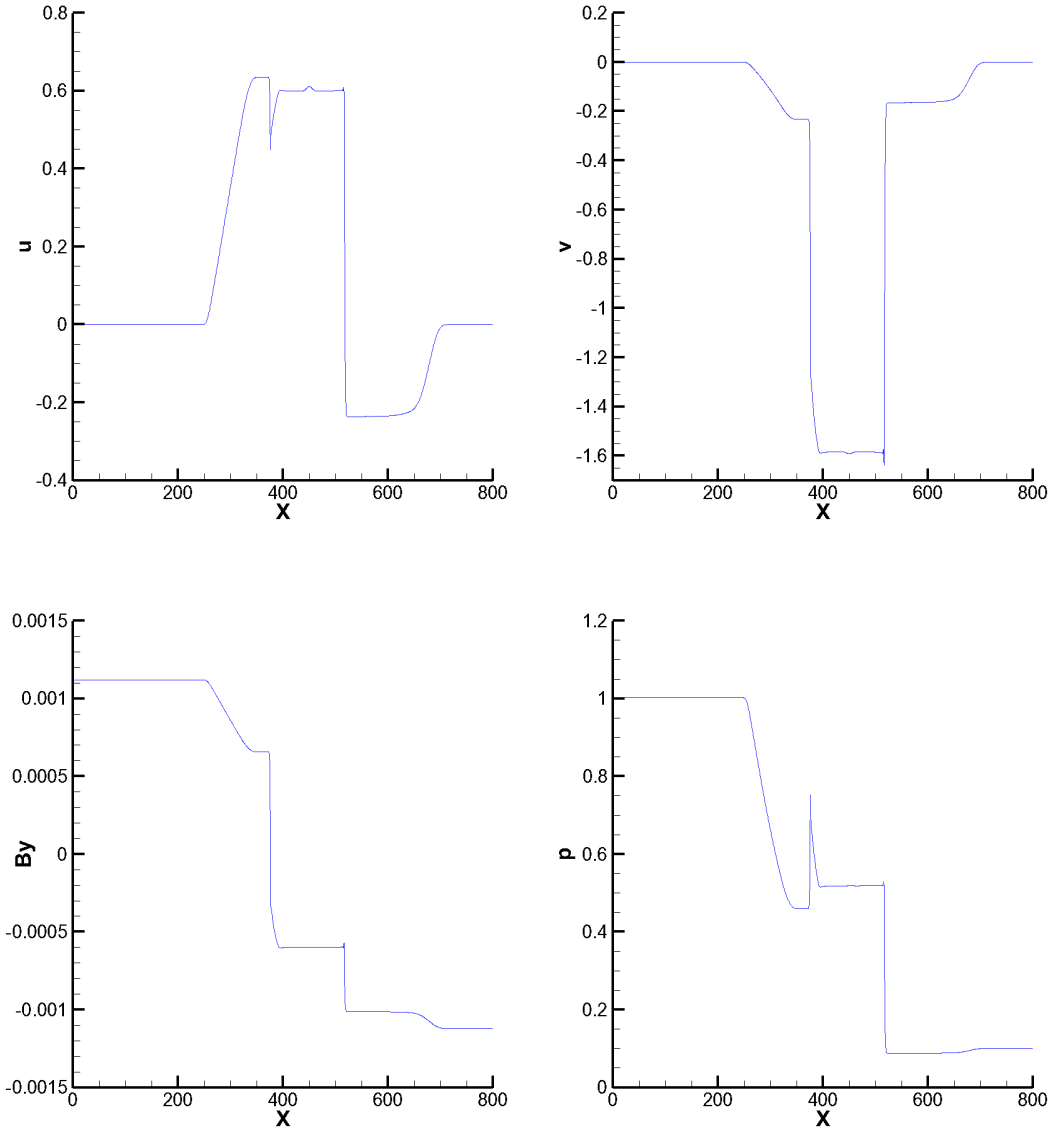

Figure 6.3: MGKM shock-tube results

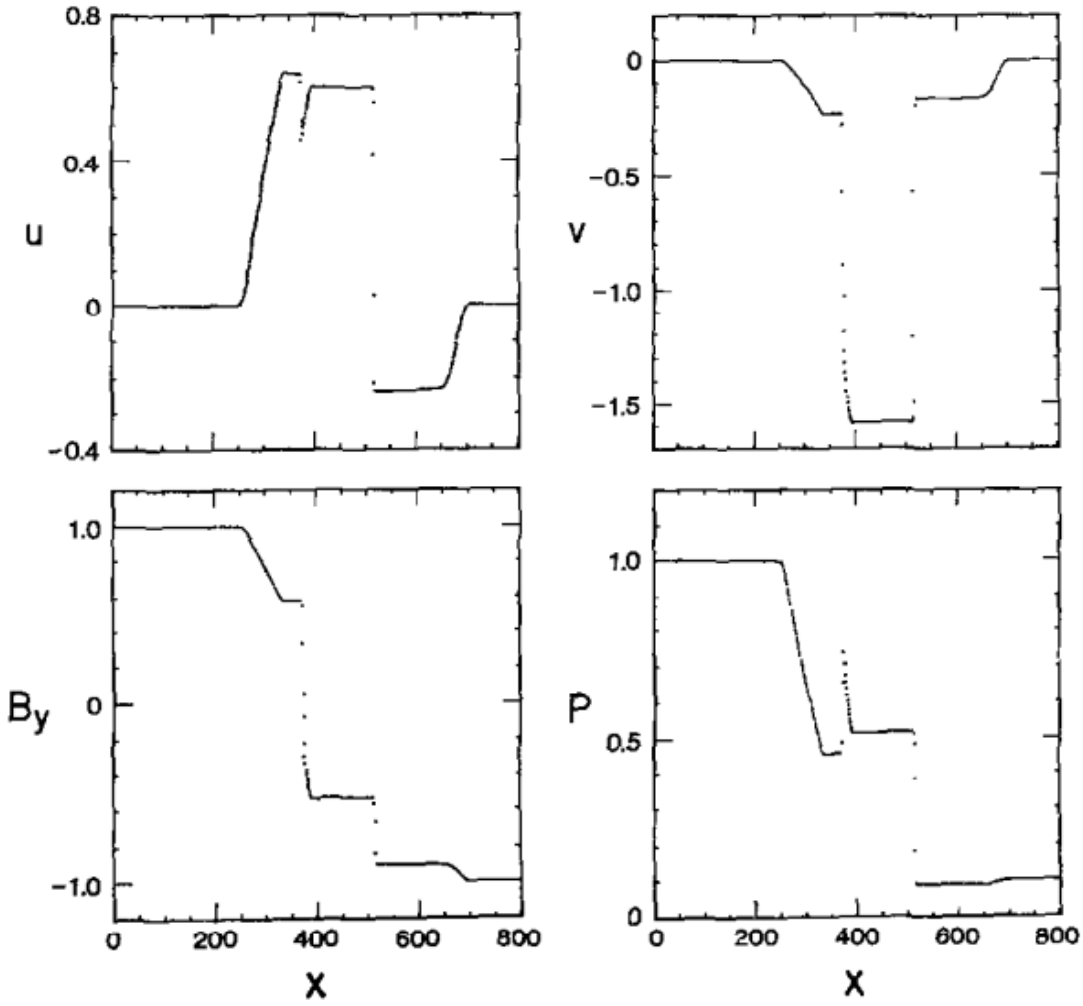

Figure 6.4: Brio-Wu shock-tube results [12]

Our results show very good agreement with those of Brio-Wu and verify the validity of MGKM as a compressible MHD solver. These results also demonstrate the increased complexity of MHD flows compared to those of Navier Stokes flows due to the presence of additional characteristic waves.

6.2.2 Hall MHD Shock-tube

Shock-tube flows were also studied in the regimes where the Hall effect becomes important. Using the same inputs as Brio-Wu, we increased the molar mass of the gas to increase the ratio ω_f/ω_{ci}. As shown in Chapter 4, this parameter characterizes the ratio of the Hall to the convective term in Ohm's law. Increasing this quantity thus increases the effect of the Hall term on the flow.

Hall MHD shocks have not been as well studied in literature and no definitive results exist to compare against. Our results showed good qualitative agreement with the limited results from literature [58, 55] shown in Figures 6.5 and 6.6. Hall MHD and two fluid solvers are employed to find the literature results shown. Additional Hall effect results are shown in Figure 6.7 to illustrate the differences between ideal MHD and Hall MHD shocks. It is evident from these figures that the additional characteristics due to the Hall term can significantly alter the shock structure of the flow. The shock structure appears to be less defined and additional oscillatory behavior occurs. Additional study of these shock structures should be done in the future to better understand the underlying physics.

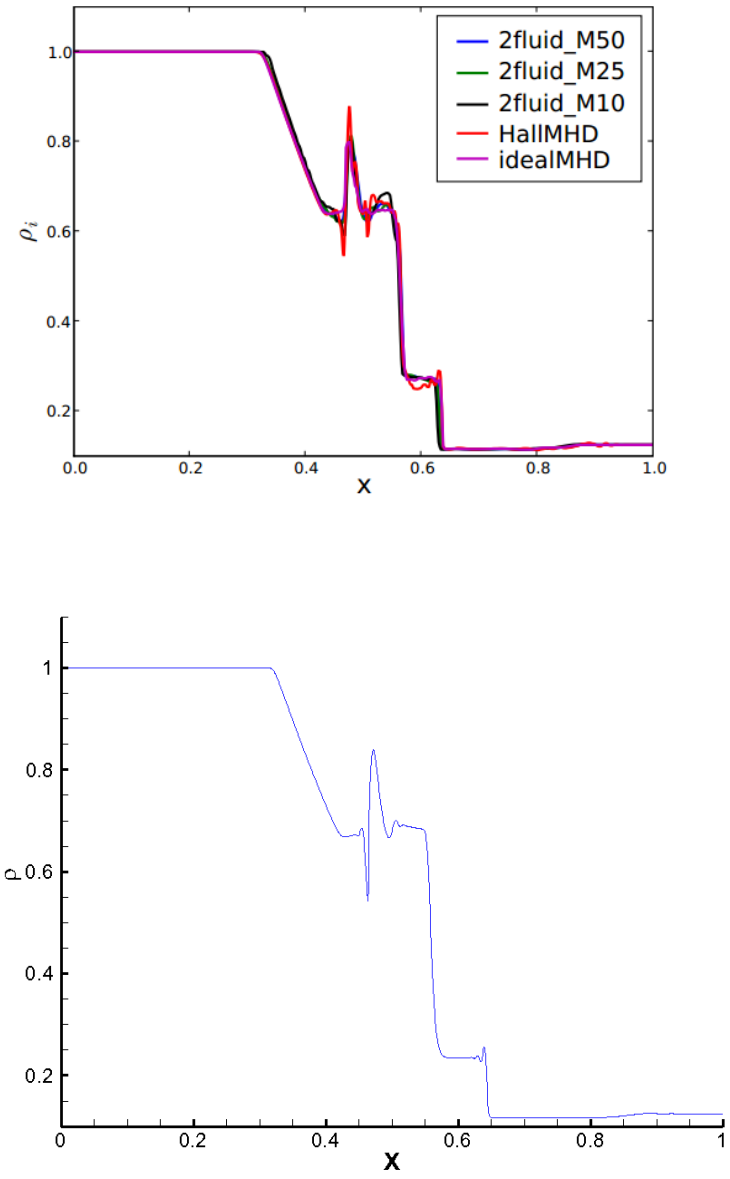

Figure 6.5: Top: Srinivasan results for $r_L = 7 \cdot 10^{-4}$,[58] Bottom: MGKM results for $r_L = 6.7 \cdot 10^{-4}$

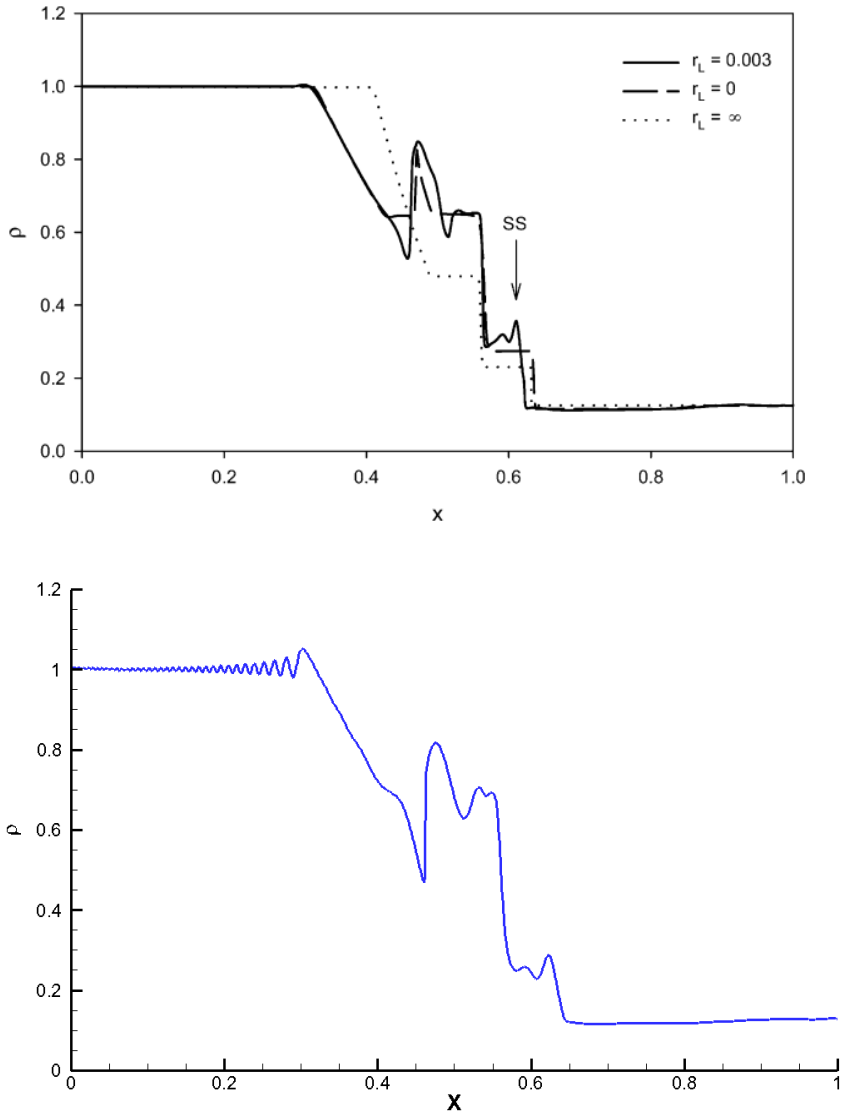

Figure 6.6: Top: Shumlak results for $r_L = 3 \cdot 10^{-3}$,[55] Bottom: MGKM results for $r_L = 3 \cdot 10^{-3}$

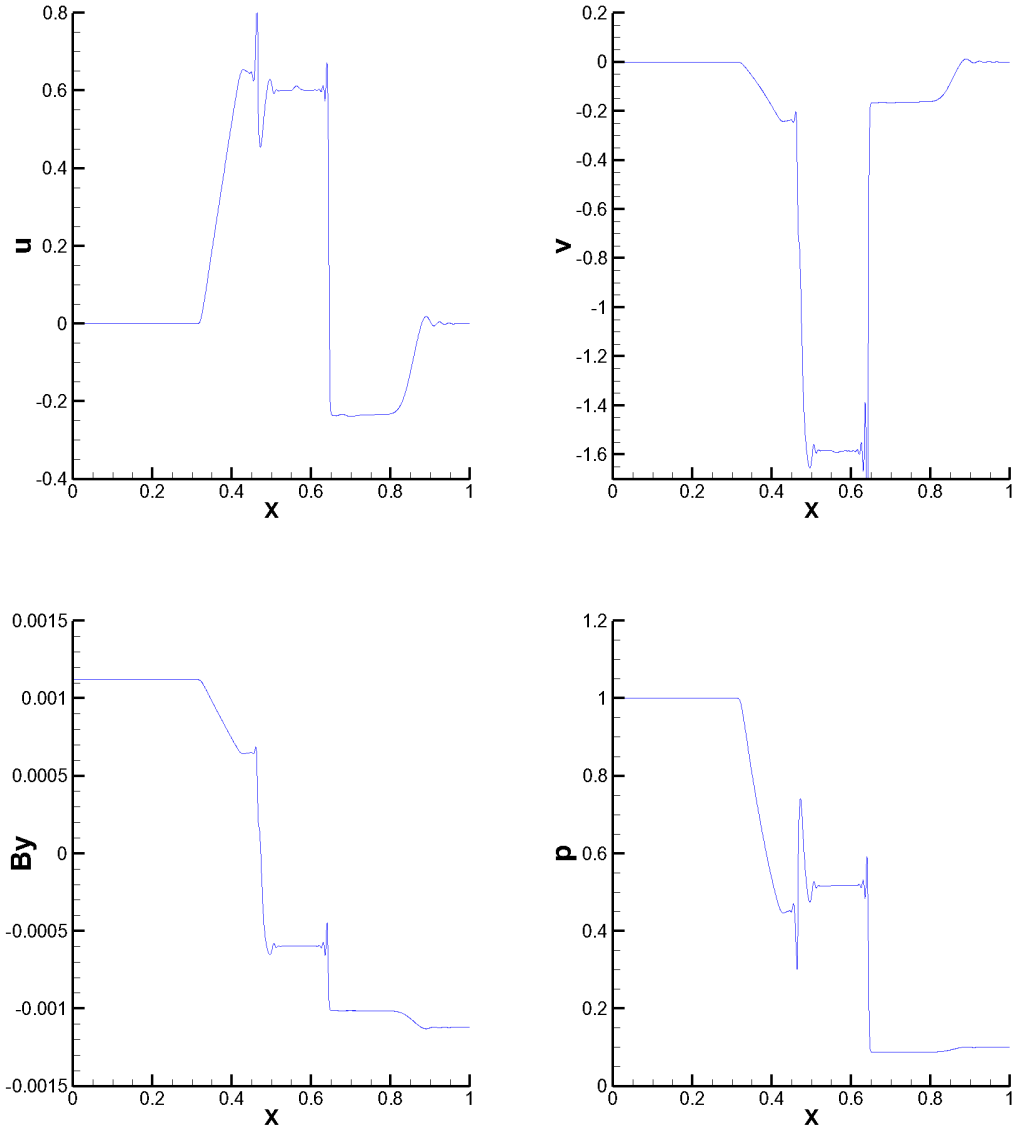

Figure 6.7: Additional Hall MGKM results for $r_L = 6.7 \cdot 10^{-4}$

6.2.3 Discussion

We have demonstrated that MGKM results agrees well with literature both in the ideal MHD limit and with the addition of the Hall term. The addition of the Hall term

complicates the structure of shock-tube flow through the additional characteristics of the Whistler wave and the Hall drift that are incorporated due to the Hall term. Oscillatory behavior develops which is not present when the Hall term is turned off. Some of this behavior can be damped out by increasing the resistivity as shown in Figure 6.8. As the conductivity is decreased the resistive diffusion becomes stronger and the oscillatory behavior is damped out. The oscillations may occur due to the finite differencing implementation of the "magnetic" portion of MGKM. As such, the WENO subroutine is not used as a limiter on the magnetic field and oscillatory behavior may develop. Reformulating MGKM so that the "magnetic" portion of the code is a finite volume implementation as well may help address this issue without artificially increasing diffusive behavior.

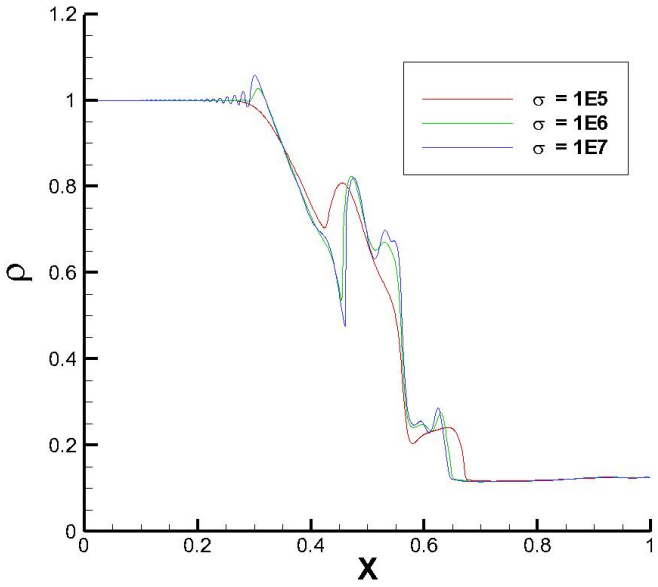

Figure 6.8: Damping due to increased resistivity

6.3 Hartmann Flow

Hartmann flows with the addition of the Hall term are studied to validate the MGKM solver. The Hartmann number is defined as $Ha = BL\sqrt{\sigma/\mu_0}$ and characterizes the ratio of the electromagnetic force to the viscous force. The computational setup for the Hartmann flow problem is shown in Figure 6.9. A pressure-driven Poiseuille flow profile is given at the left boundary which is allowed to develop downstream under the influence of an applied magnetic field perpendicular to the flow direction. In the absence of the field the enforced pressure gradient would maintain the Poiseuille flow profile set at the inlet.

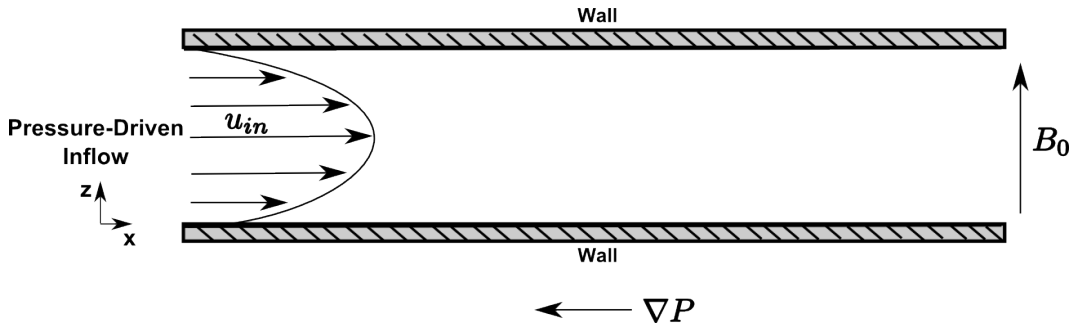

Figure 6.9: Hartmann flow setup

Hartmann flows in regimes where the Hall effect is negligible have been extensively studied. [59, 3] Relatively simple analytical solutions exist to for these flows which may be reproduced by computational methods. Inclusion of the Hall term significantly complicates the dynamics of the flow and no simple analytical solutions which are well suited for comparison with computational methods exist. In existing semi-analytical solutions assumptions are made regarding the applied electrical field which are difficult to impose computationally with a MHD solver. [48]

For the case of Hartmann flows, the Hall term can be neglected when the ratio

of Hall effects to resistive effects is small. This ratio is characterized by $\alpha = \omega_{ce}\tau_e$ where as α increases, the effect of the Hall term increases. To measure the effect of the Hall term we performed a number of numerical simulations with increasing α, the results of which are shown in Figure 6.10 .

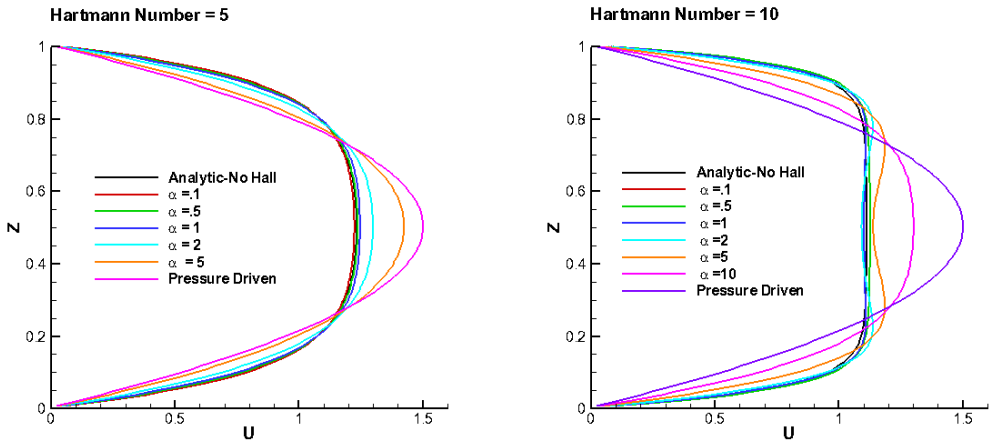

Figure 6.10: Hartmann flow results of normalized u velocity profiles

As expected, the results for the low α where the Hall term is negligible and the analytical solution for a flow without the Hall term show good agreement. This behavior demonstrates that the flow behaves correctly in the limit where Hall effects are negligible. As α increases, the flow develops a more complex structure as the effect of the Hall term becomes more pronounced and eventually approaches the original pressure driven solution. Similar behavior was shown and predicted by Sato [48] and overall our results show good qualitative agreement. A comparison between these results is shown in Figures 6.11-6.12 below in which the results from Sato have been digitized and non-dimensionalized to compare with our results. Sharp edges in the semi-analytical results are due to digitizing errors that occur when multiple lines cross in Sato's original plots. The numerical results show an induced cross flow

which is consistent with the results of Sato. It is important to note that in the Figure 6.12 we changed the flow direction from the negative $\hat{y}$ direction to the $\hat{z}$ direction to correspond with the axes used by Sato in which the applied field direction is $\hat{y}$.

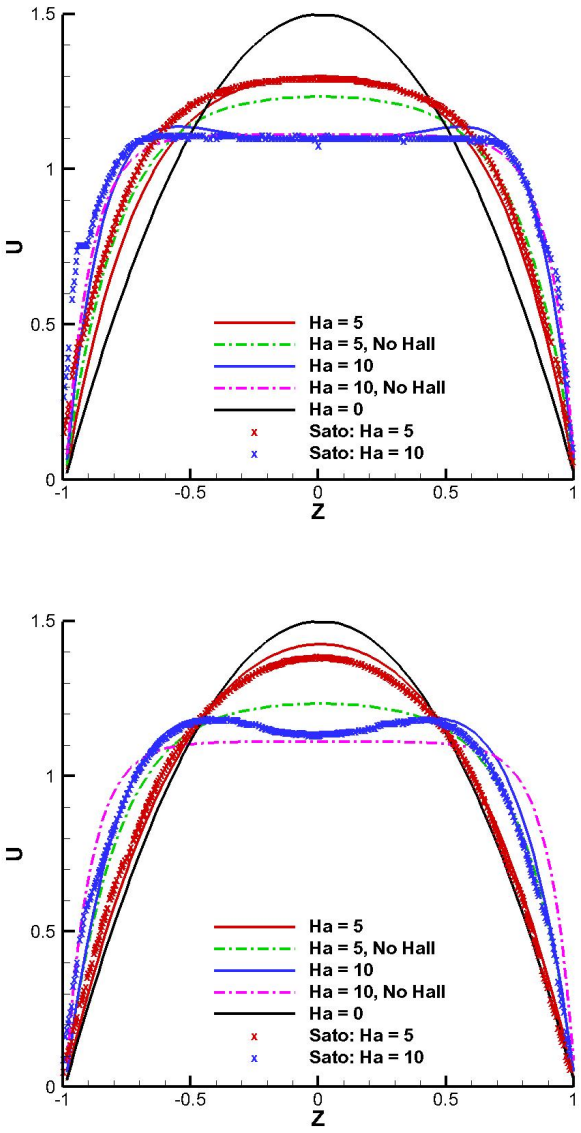

Figure 6.11: Hartmann flow results of normalized u velocity profiles for comparison with Sato. Top: $\alpha = 2$, Bottom: $\alpha = 5$

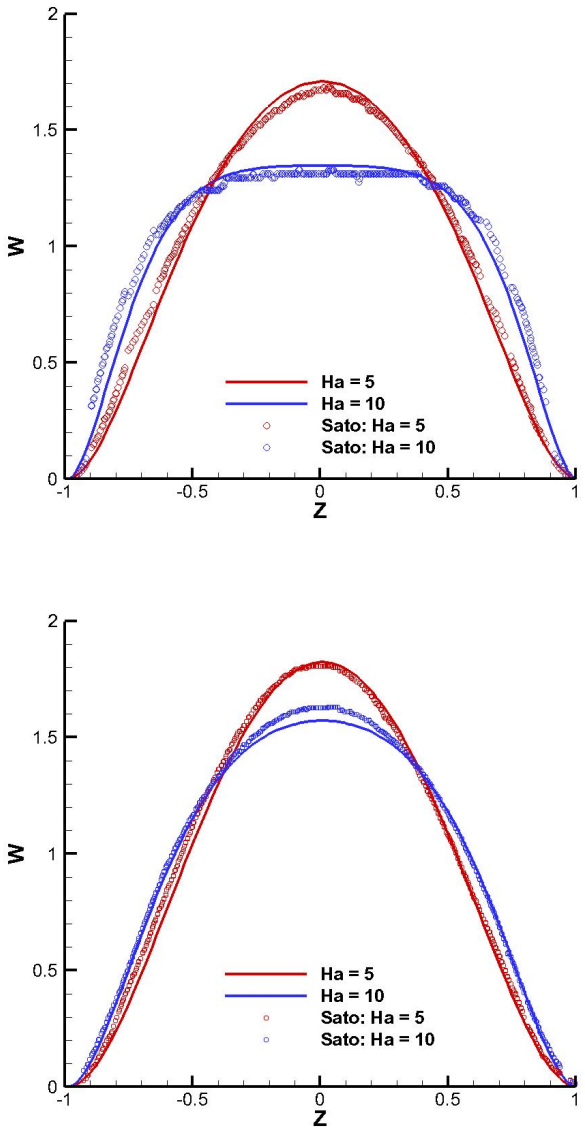

Figure 6.12: Hartmann flow results of normalized v velocity profiles for comparison with Sato. Axis is changed to w and the sign changed to align with coordinates of Sato. Top: $\alpha = 2$, Bottom: $\alpha = 5$

Figures 6.13 - 6.18 show additional results of the MGKM Hartmann flow results. These contours show the development of Hartmann flows with $Ha = 10$ as $\alpha =$

$.1 \rightarrow 10$. The quantities are normalized by the mean u velocity and the applied field strength B_0 when indicated. Each test case has slightly different parameters due to striving to keep the appropriate non-dimensional numbers constant while varying α. For example, to increase α the magnetic field strength must be increased which results in an decrease in the characteristic length L to keep the Hartmann number constant. This leads to a difference of two orders of magnitude for B_0 and L for $\alpha = .1 \rightarrow 10$. All plots have the axes non-dimensionalized by the channel height. In general we attempted to use the same contour scale, but some cases did not permit this. Figure 6.14 is particularly interesting because it shows the cross flow which is created due to the Hall term. The magnetic field contours are included primarily to give a general idea of the changing field shape, if additional time permitted further study of these fields could prove enlightening.

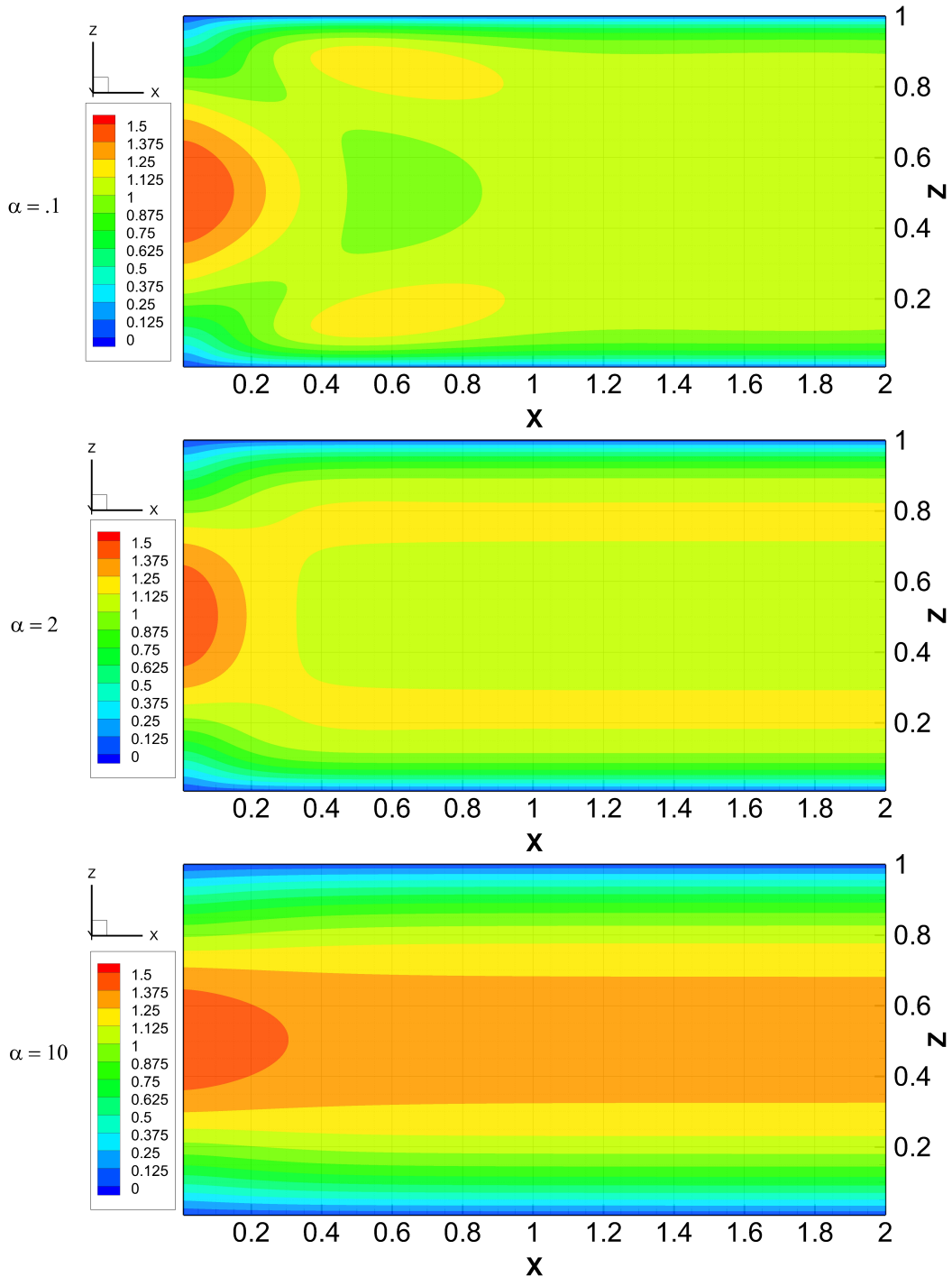

Figure 6.13: Hartmann flow with normalized u contours.

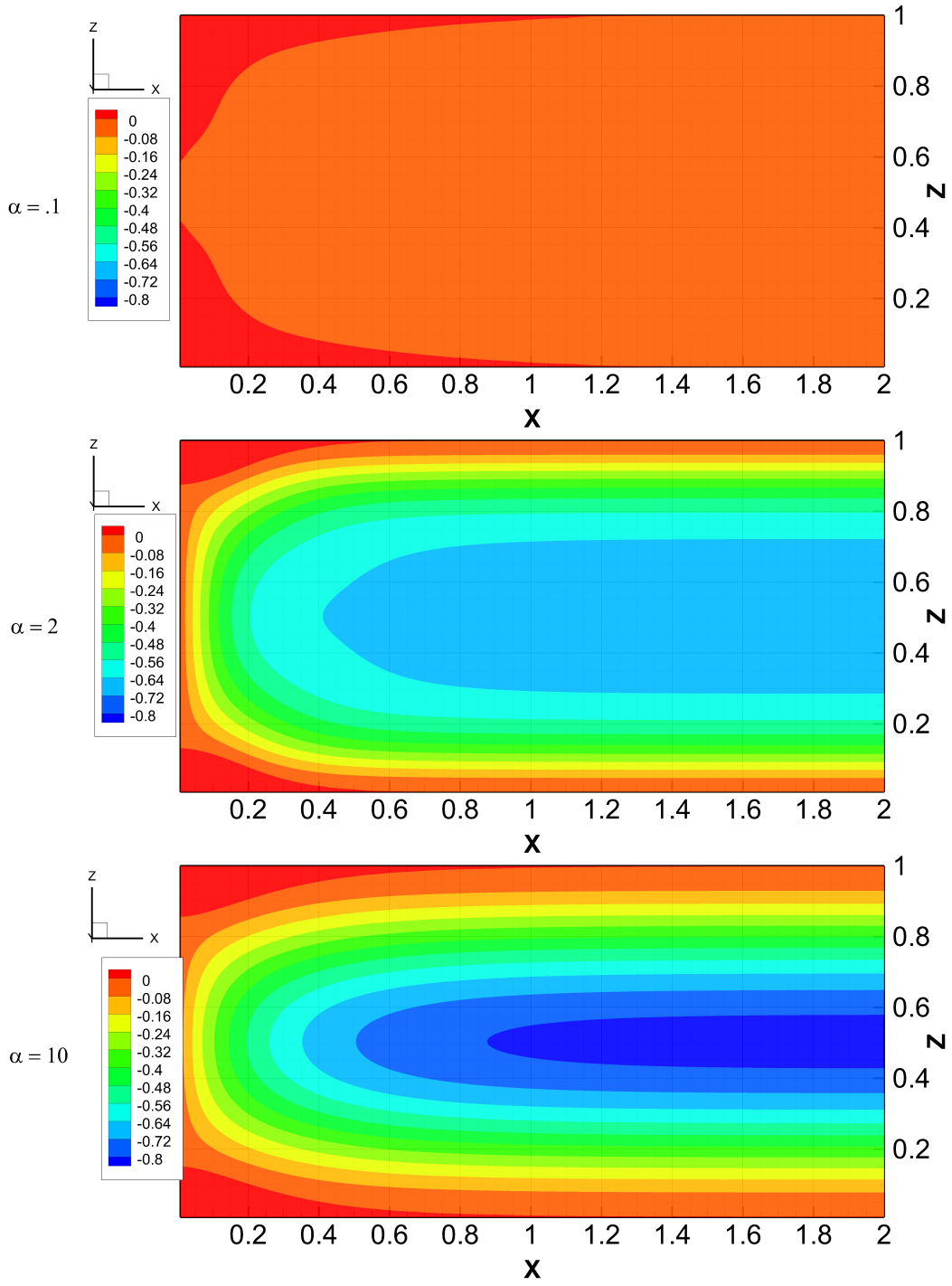

Figure 6.14: Hartmann flows with normalized v contours.

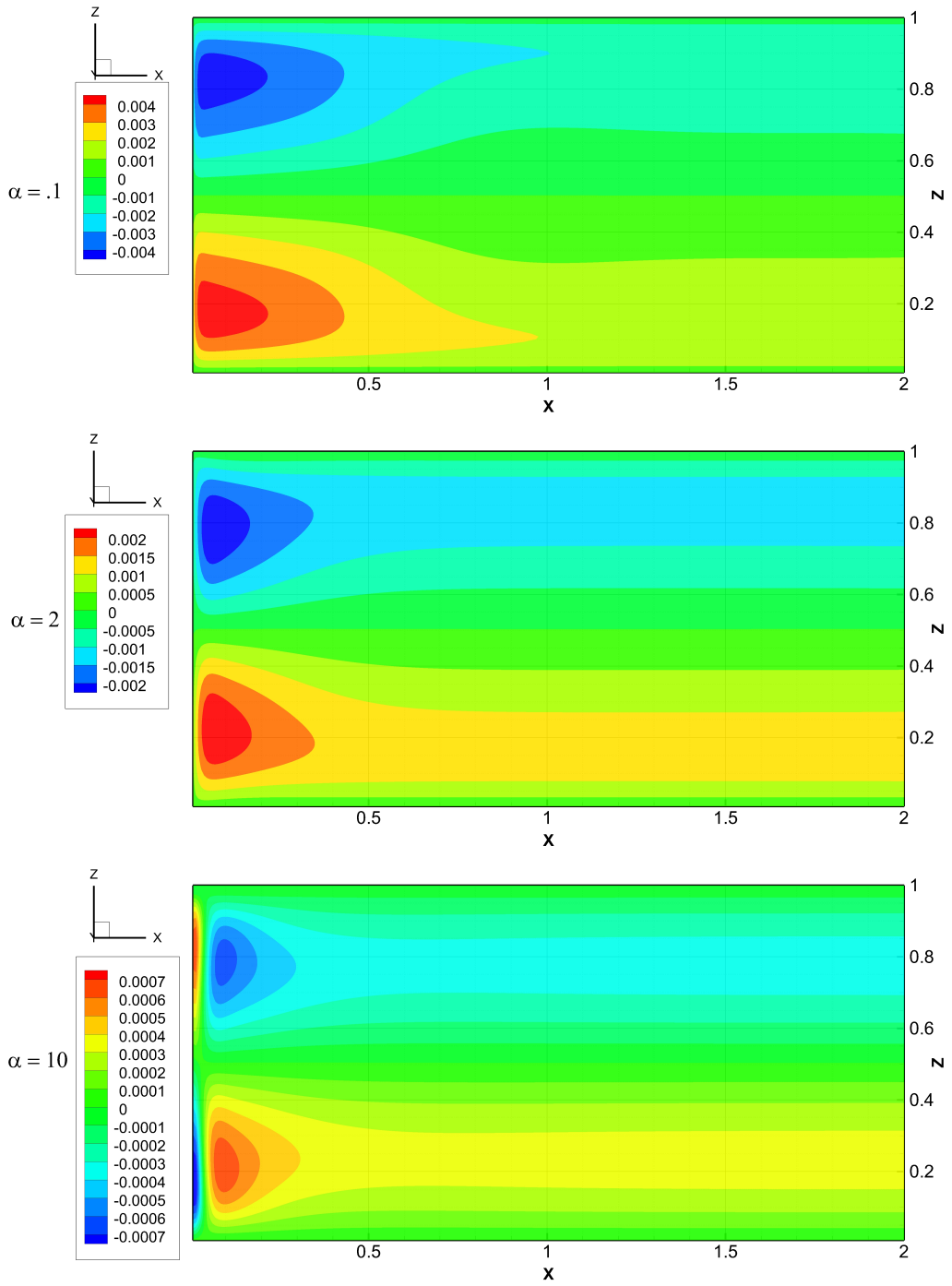

Figure 6.15: Hartmann flows with B_x contours.

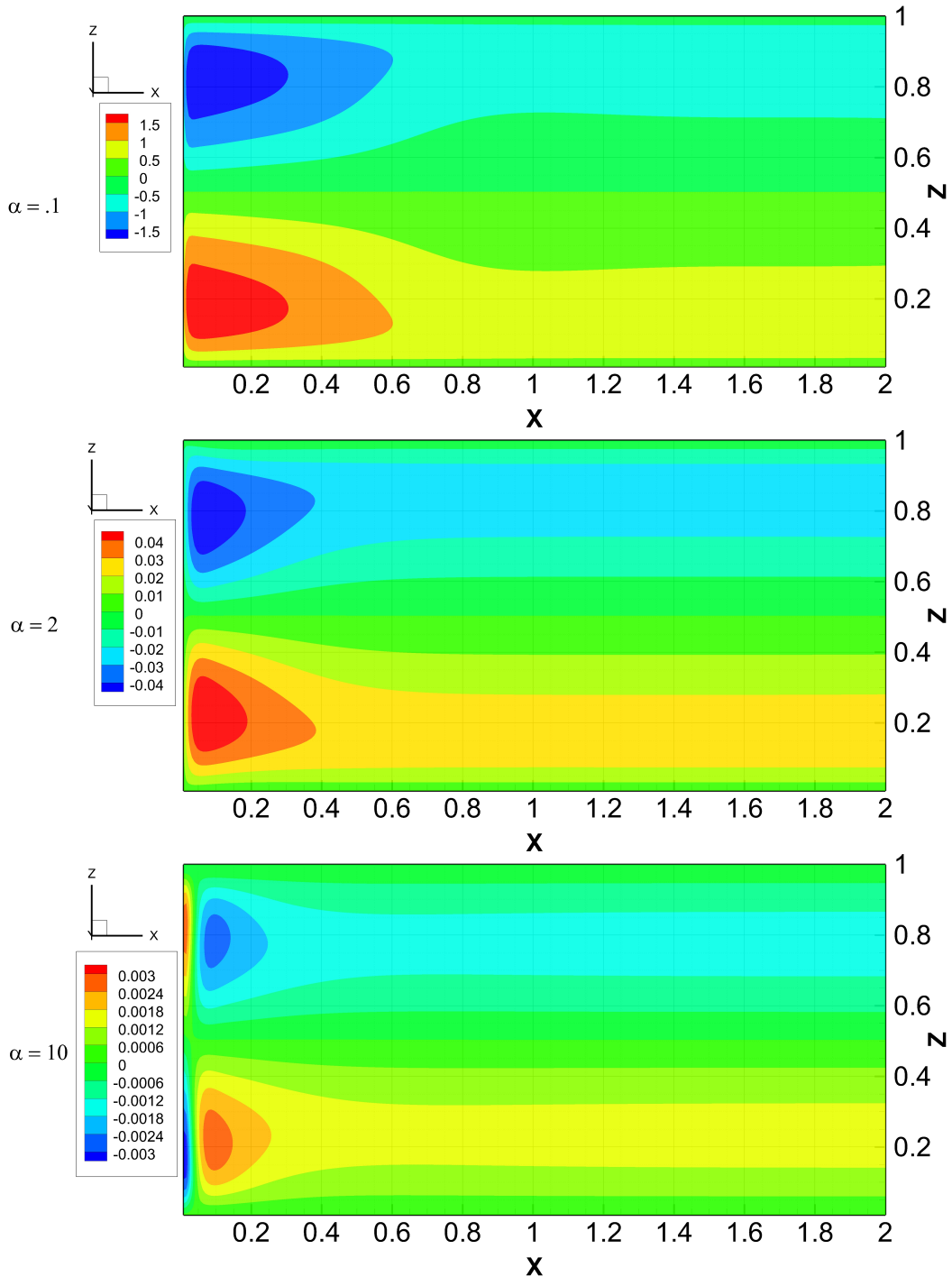

Figure 6.16: Hartmann flows with normalized B_x contours.

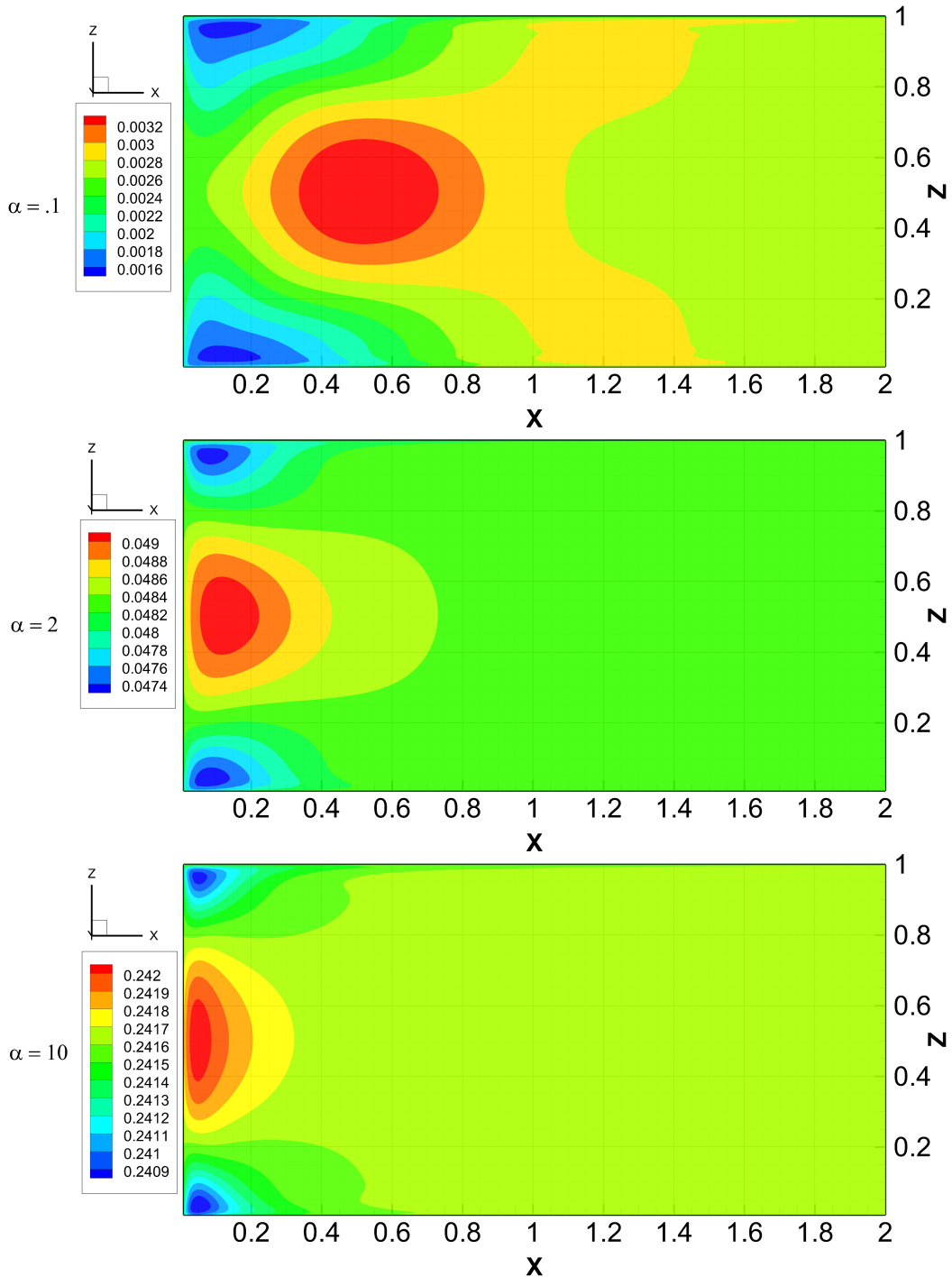

Figure 6.17: Hartmann flows with B_z contours.

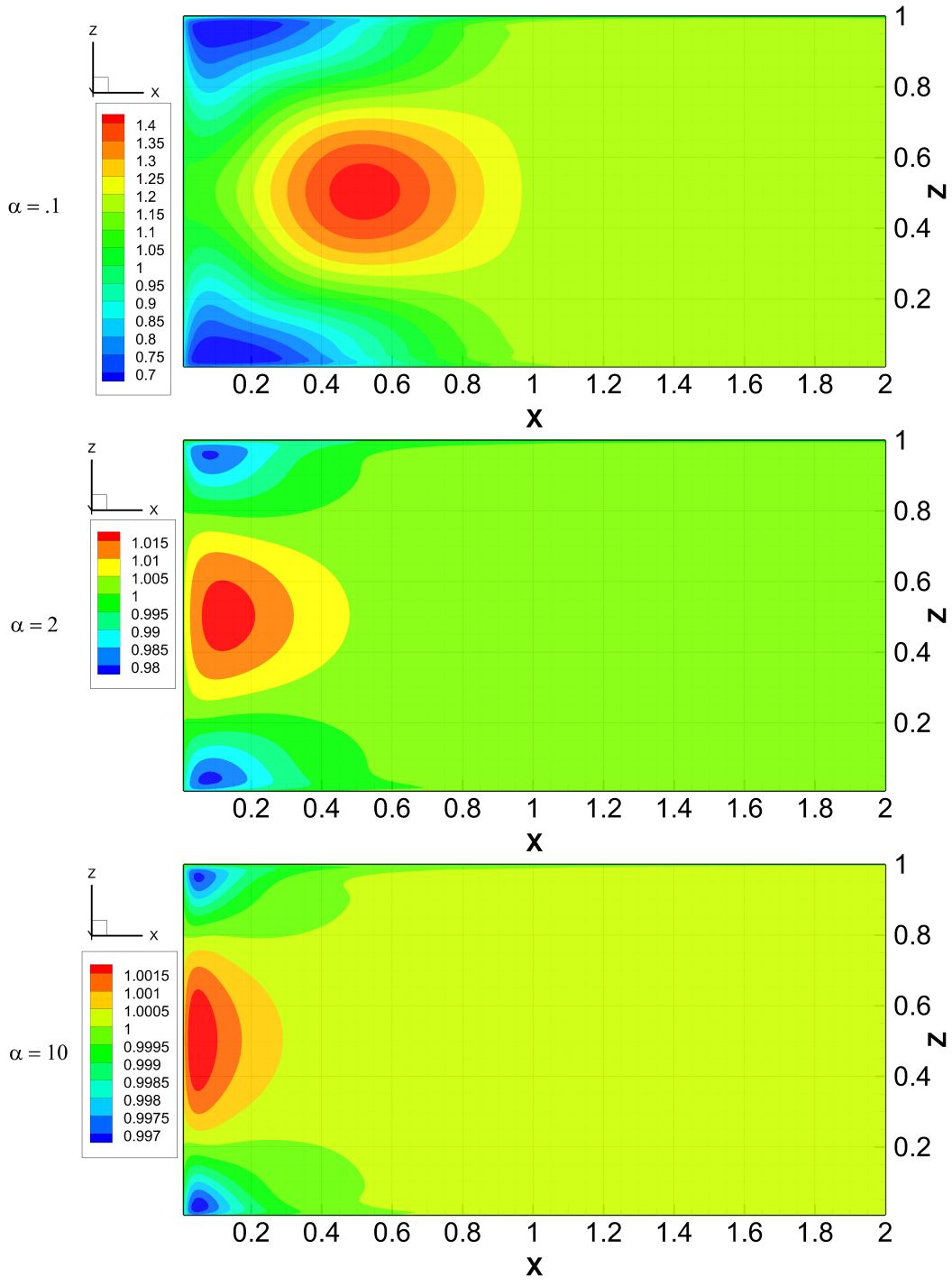

Figure 6.18: Hartmann flows with normalized B_z contours.

6.3.1 Discussion

We have studied Hartmann flows in which the Hall effect is important and showed behavior that was predicted by the analytical analysis of Sato.[48] The addition of Hall physics complicates the dynamics of the flow and creates cross flows perpendicular to the original inlet flow and the applied magnetic field. This behavior results from the formation of a induced current along the flow direction which creates a $J \times B$ force perpendicular to the original flow and field direction. This physics is attributed due to the magnetization of electrons, which remain on field lines, and the demagnetization of ions, which flow across field lines. This behavior will be discussed more in the following chapter. The variation of parameters in the Hartmann flow problems did not lend itself well to simple comparisons between the induced currents in the different problems.

These numerical studies are novel and we were not able to find significant similar work in literature aside from the analytical studies of Sato. Additional study of this problem can be done in the future to further characterize this behavior and questions remain about which boundary conditions are best for this type of problem. We have confirmed through numerical studies the analytical work of Sato.

7. JET RESULTS

7.1 Introduction

Upon validation of MGKM we began to study jet flows relatable to the magnetic nozzle problem. The purpose of these jet flows is to illustrate the influence of the Hall effect and provide insight on the overall magnetic nozzle problem.

7.2 Computational Domain

The computational domain for the jet cases is shown in Figure 7.1. An inflow profile is imposed through a Dirichlet boundary condition based on a Schlichting jet profile [49]. This inflow condition consists of flow only in the axial direction, $\hat{x}$, and assumes that the induced field is much smaller than the applied field. By this assumption the induced field is set to zero at the inlet. The inflowing plasma interacts with an initially stationary plasma of the same density, temperature, and static pressure in the domain. All other boundaries are set to zero-gradient, Neumann boundary conditions for the velocity and the induced field.

A diverging applied magnetic field is imposed over the entire domain and is read in as an input to the solver. This diverging applied field is generated by a current loop and is calculated through a MATLAB subroutine which approximately solves the Biot-Savart law through elliptic integrals. The current loop has a radius of 1.6 meters and is placed at the first grid point so that the applied magnetic field lines are parallel to the incoming flow at this point. The applied field is a constant and does not vary in time while the induced field is self consistently calculated by the MHD equations. An example of a typical domain and the diverging applied magnetic field lines is shown in Figure 7.2.

The typical domain consists of a $200 \times 64 \times 64$ grid with a grid size of $\Delta x = 0.025$.

The grid size was chosen to enable multiple test cases to be run. In the future finer grids should be run which will be discussed in later sections. The qualitative physical behavior did not vary with grid refinement, although some minor quantitative differences are seen.

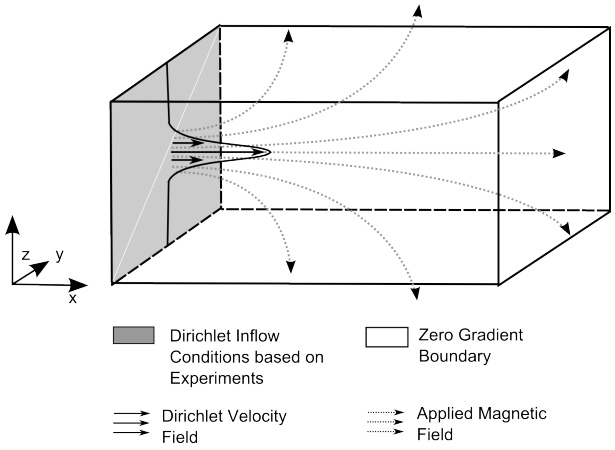

Figure 7.1: Computational domain

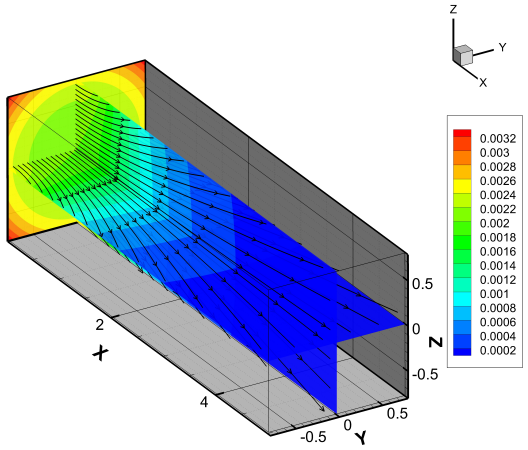

Figure 7.2: Applied magnetic field lines with contours of the magnitude of the applied field (T).

Multiple test cases of the plasma jets with the Hall effect were studied with varying parameters and boundary conditions. The case which best shows the effects of the Hall term is chosen to be presented in this chapter. Overall results between different jet cases was found to be consistent and presentation of these results would prove redundant.

7.3 Parametric Regime

The physical parameters and equivalent non-dimensional numbers for the selected jet case are shown in Tables 7.1 and 7.2 respectively. The parameters chosen are similar to those studied by Araya[3] with necessary changes made to shift the problem into the Hall and magnetic nozzle physics regime. The magnetic nozzle regime found in the previous chapters is shown for comparison as well as the parameters used by Araya. The working fluid for our numerical cases is no longer a liquid metal jet as it was for Araya, but is instead nearly a Xenon plasma.

From these tables it is evident that the parameters chosen for the numerical experiment generally fall within the parameter range of the magnetic nozzle experiments, but do not correspond to any single test case. The primary parametric differences between our numerical experiment and the magnetic nozzle regime are the magnetic field strengths and the Mach numbers which are lower in the numerical experiments due to computational restrictions. The Mach number for the numerical experiments is still within the sub-sonic, incompressible regime, while the Mach numbers in the magnetic nozzle regimes are highly compressible and mostly super-sonic.

It has to be stressed that although the numerical experiments are similar to magnetic nozzle flows parametrically they are not equivalent due to the lack of super-sonic jet expansion. This is evidenced in the differences between the the jet static pressure and the background static pressure ratios. In the future high Mach number

and jet expansion cases should be studied to fully characterize this type of flow. Further development of the numerical solver is required to enable the study of these cases which are more directly related to experiments.

Case	$\rho\ (kg/m^3)$	$n\ (\#/m^3)$	$T\ (eV)$	$U_{in}\ (m/s)$	$\mu\ (kg \cdot m/s)$	$\sigma\ (S/m)$	$B\ (T)$
Mag. Noz.	$10^{-9} - 10^{-6}$	$10^{17} - 10^{20}$	$10^{-1} - 10^{2}$	$10^{3} - 10^{5}$	$10^{-8} - 10^{-2}$	$10^{3} - 10^{4}$	$10^{-2} - 10^{-1}$
Num. Exp.	$1.0 \cdot 10^{-5}$	$4.59 \cdot 10^{19}$	$3.04 \cdot 10^{0}$	$4.1 \cdot 10^{2}$	$1.37 \cdot 10^{-6}$	$1.0 \cdot 10^{5}$	$2.0 \cdot 10^{-3}$
Araya	1.0	$2.08 \cdot 10^{25}$	$3.04 \cdot 10^{-2}$	$4.1 \cdot 10^{1}$	$1.37 \cdot 10^{-2}$	$1.0 \cdot 10^{4}$	$3.0 \cdot 10^{-2}$

Table 7.1: Fluid conditions

Case	Reynolds	Magnetic Reynolds	Mach	Electron Hall	$1/(\tau_{res}\omega_{ci})$	p_{back}/p_{jet}
Mag. Noz.	$10^{0} - 10^{4}$	$10^{-2} - 10^{3}$	$10^{0} - 10^{1}$	$10^{0} - 10^{3}$	$10^{-2} - 10^{1}$	$\approx 10^{-5}$
Num. Exp.	$6.00 \cdot 10^{2}$	$1.03 \cdot 10^{0}$	$2.17 \cdot 10^{-1}$	$2.72 \cdot 10^{0}$	$1.74 \cdot 10^{-1}$	1
Araya	$6.00 \cdot 10^{2}$	$1.03 \cdot 10^{0}$	$1.00 \cdot 10^{-1}$	$9.00 \cdot 10^{-5}$	$2.57 \cdot 10^{-4}$	1

Table 7.2: Non-dimensional numbers

7.4 Preliminary Physics Discussion

Before presenting the results of the plasma jet cases we will briefly discuss the anticipated physics. Hall effects on plasma jets with diverging magnetic fields have not been extensively studied and magnetic nozzle studies have largely neglected the effect of Hall physics to simplify the problem. However, we have shown in our literature survey that these effects may become important and in this study wish to characterize the behavior that may occur due to Hall effects. A brief discussion of the physics of the Hall term in MHD magnetic nozzles was given by Gerwin in which he states, "the main effect of the Hall term is to induce a small rotational motion of the plasma."[24] Our primary research question thus becomes: *Do magnetohydrodynamic plasma jets under the influence of a diverging magnetic field experience rotation due to the Hall effect?*

7.4.1 Resistive MHD Jet Physics

To explain the physics in magnetic nozzles we begin by discussing the behavior of a resistive MHD plasma jet in a diverging magnetic field without the Hall effect. In MHD plasmas magnetic field lines and velocity stream lines mutually attract one another and generally want to line up. This alignment occurs due to the Lorentz force which allows streaming of particles along magnetic field lines and induces cyclotron motion in the perpendicular field direction. The ideal MHD equations force the flow and field lines to line up with one another, while resistive MHD allows cross field transport due to collisional processes. A resistive magnetic nozzle balances the attraction between the magnetic field and velocity steam lines due to the Lorentz force with the cross-field resistive diffusion.

Magnetohydrodynamics is based on the interaction of the velocity flow field and the magnetic field. Currents and electric fields are secondary quantities that are derivative of the velocity and magnetic fields. They can however be used to more intuitively understand the physical processes. A schematic of the currents and fields in a resistive MHD jet is shown in Figure 7.3. The axial flow and the radially diverging magnetic field mutually attract one another as they interact. The current necessary for this attraction is an azimuthal current that results in a Lorentz force which expands and slows down the jet.

7.4.2 Hall MHD Jet Physics

The Hall MHD jet undergoes the same physical processes discussed in the previous sub-section and includes additional effects due to Hall physics. The Hall term models effects that occur due to ion demagnetization. Ion demagnetization occurs when the ion Larmor radius is larger than or on the order of a characteristic dimension of the system. The Hall term captures the physics of electrons which remain attached to the magnetic field lines and ions which may stream across them. Hall MHD is often referred to as incorporating two fluid effects in the single fluid MHD equations.

In a magnetic nozzle plasma jet the Hall effect can generate axial currents. These axial currents may form due to electrons remaining attached to the diverging magnetic field lines and ions which stream axially across them. A schematic of these currents is shown in Figure 7.3. The interaction of these axial currents and the applied field result in a Lorentz force which causes the azimuthal rotation predicted by Gerwin. [24]

Radial currents may also be induced due to the magnetization of electrons and demagnetization of ions. As the field lines diverge they pull the electrons radially outward without the ions. This is results in a radially inward current which interacts with the axial magnetic field component and produces an azimuthal rotating force.

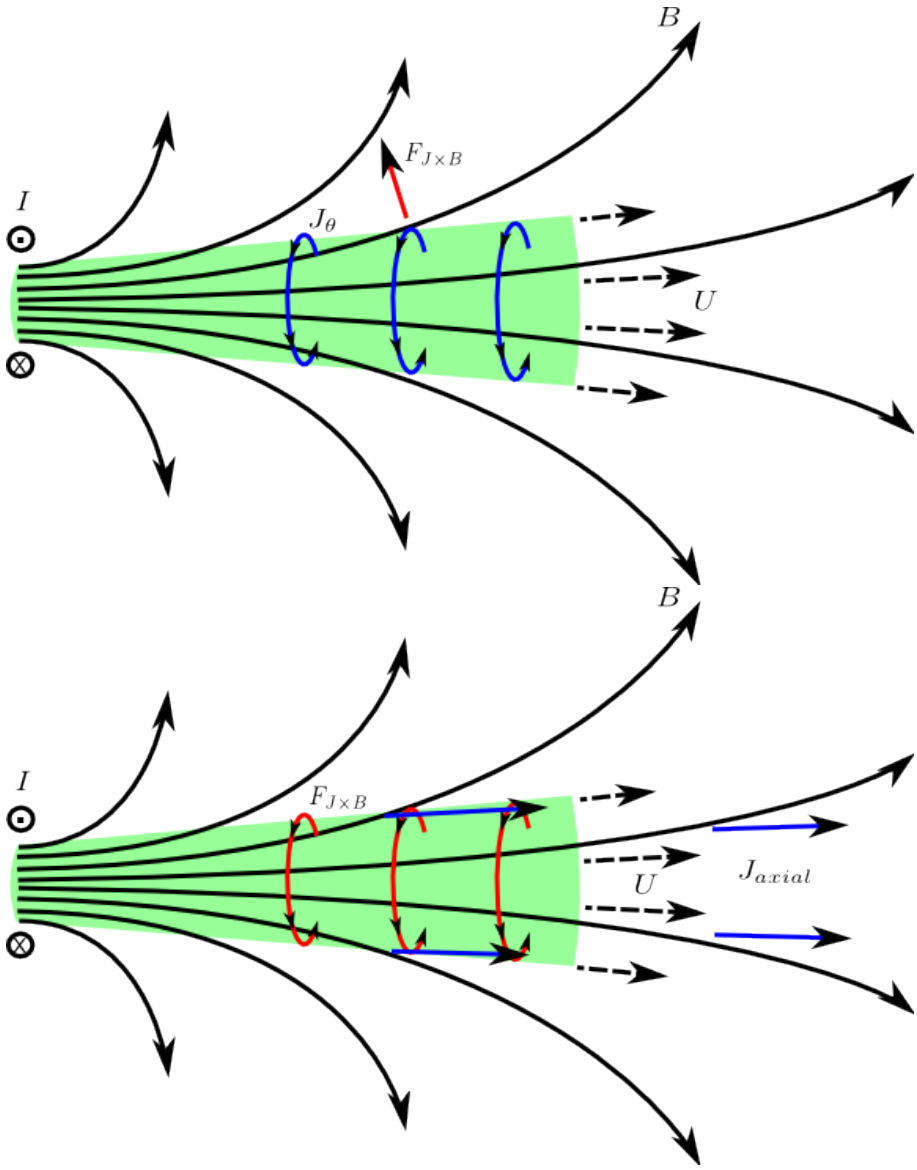

Figure 7.3: Top: Resistive MHD jet. Bottom: Additional Hall MHD jet effects. Blue lines correspond to induced currents J, red lines correspond to $J \times B$ forces, I represents the current loop that creates the applied field, dashed lines represent the velocity U, and finally solid black lines represent the applied field B. The plasma is represented by the transparent green color.

7.5 Hall Effect Plasma Jet Results

The results from the Hall effect plasma jet numerical experiments are presented in this section. The results are compared for three jet flows: no magnetic field, magnetic field without the Hall term, and magnetic field with the Hall term. Typical results comparing the velocity magnitude in the various runs is shown in figure 7.4, these plots serve primarily as a means to orient the reader for the later plots. Slices of the $\hat{y}$ and $\hat{z}$ planes are placed at the middle of the domain while $\hat{x}$ planes are at the inlet. Streamlines for future plots are 3D streamlines which originate at the inlet on these mid-planes unless otherwise mentioned. Contour levels and streamline origination points are identical for all plots that are shown together unless otherwise noted.

Figures 7.5 and 7.6 are $\hat{y}$ mid-plane slices that show contours and streamlines of the velocity. It is evident from these graphs that in the cases with the magnetic field turned on the velocity streamlines near the inlet tend to get pulled radially outward in the direction of the magnetic field in comparison with the slight inward motion without the field. Streamline rotation is seen in the Hall effect case where streamlines rotate in front of and behind the mid-plane. Figure 7.7 shows the $\hat{x}$ inlet-plane and demonstrates the flow streamline rotation that occurs due to the Hall term. The cases without the Hall term only show radial motion, while with the Hall term significant rotation is seen. Figures 7.8 and 7.9 show iso-surfaces of the velocity magnitude for the various cases. These iso-surfaces demonstrate a slow down of the jet when the magnetic field is turned on. This slow down and expansion occurs due to the flow redirection caused by the $J \times B$ force resulting from the azimuthal currents. Figure 7.10 demonstrates flow entrainment that occurs due to flowing into a stationary background plasma of the same static pressure. This behavior is similar to that seen by Araya.[3] Entrainment characteristics are also altered due to the

addition of the Hall term. Magnetic nozzle runs that include expansion will not exhibit this entrainment behavior and will expand throughout the domain.

Figure 7.11 shows contours of the azimuthal, $\hat{\theta}$, velocity of the plasma that occur due to the Hall effect. The $\hat{\theta}$ direction is defined by the right hand rule with respect to the axial, $\hat{x}$, direction. A region of negative azimuthal velocity is seen at the inlet which results partly due to the strong boundary condition of $B_i = 0$ at the inlet. Cases with a zero gradient boundary condition at the inlet do not show this initial negative $\hat{\theta}$ velocity, but give a more ambiguous boundary for the inlet which is difficult to justify physically.

Having demonstrated the effects on the flow field, we will now analyze the induced currents which are responsible for these changes. Figure 7.12 shows induced azimuthal currents in the plasma jet. As discussed in the theory section these currents are responsible for the expansion of the plasma jet in the magnetic field direction and also result in some slow down of the jet. These currents are present both with and without the Hall term. Figure 7.13 shows contours of induced axial, $\hat{x}$, currents in the plasma jet. These currents occur due to the Hall term and result in the forces responsible for the azimuthal velocity and plasma rotation. As mentioned in the theory section these currents may occur due to positive ions streaming across the diverging magnetic field lines. Figures 7.14, 7.15, and 7.16 show contours of the induced current magnitude and streamlines of the induced current. For cases without the Hall term the induced currents are purely azimuthal and remain in the $\hat{x}$ planes. Cases with the Hall term have streamlines that form helical configurations originating at the inlet.

Figure 7.17 shows the induced magnetic field and the stream traces of these induced fields. The induced field is strongest at the inlet but generally remains smaller than the applied field by at least an order of magnitude resulting in little

alteration of the total magnetic field. The induced fields in the case with the Hall term also show rotation which is not evident in cases without the Hall term.

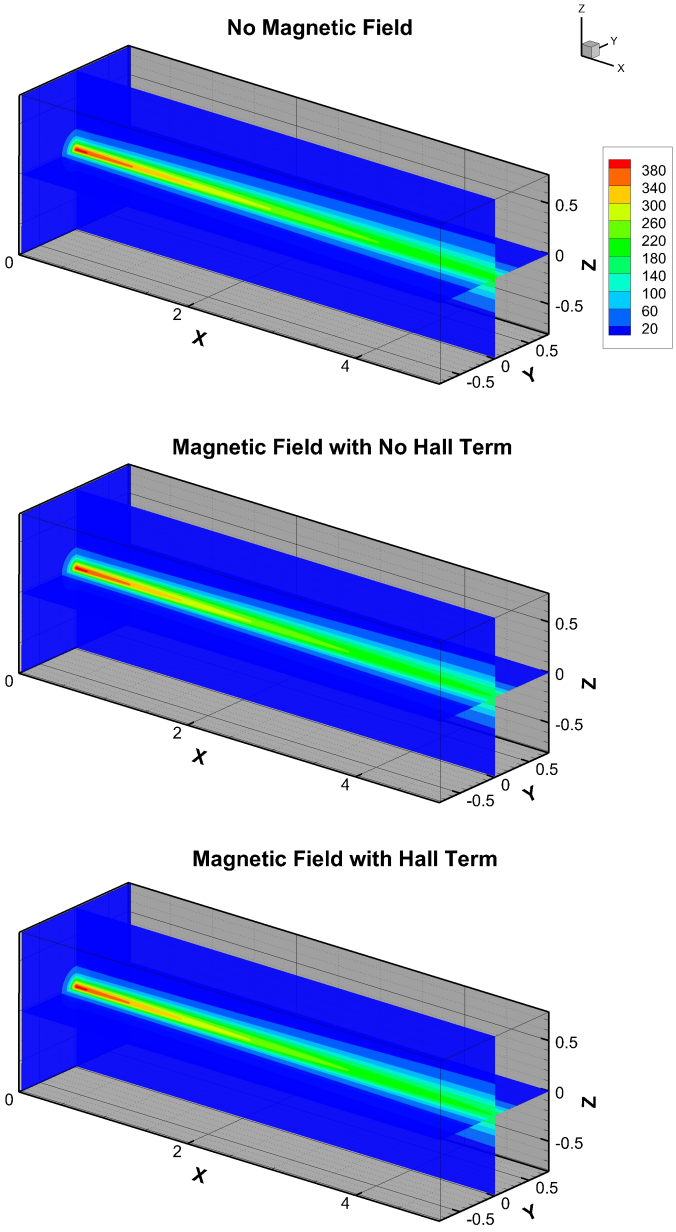

Figure 7.4: Velocity magnitude (m/s) contours in 3D.

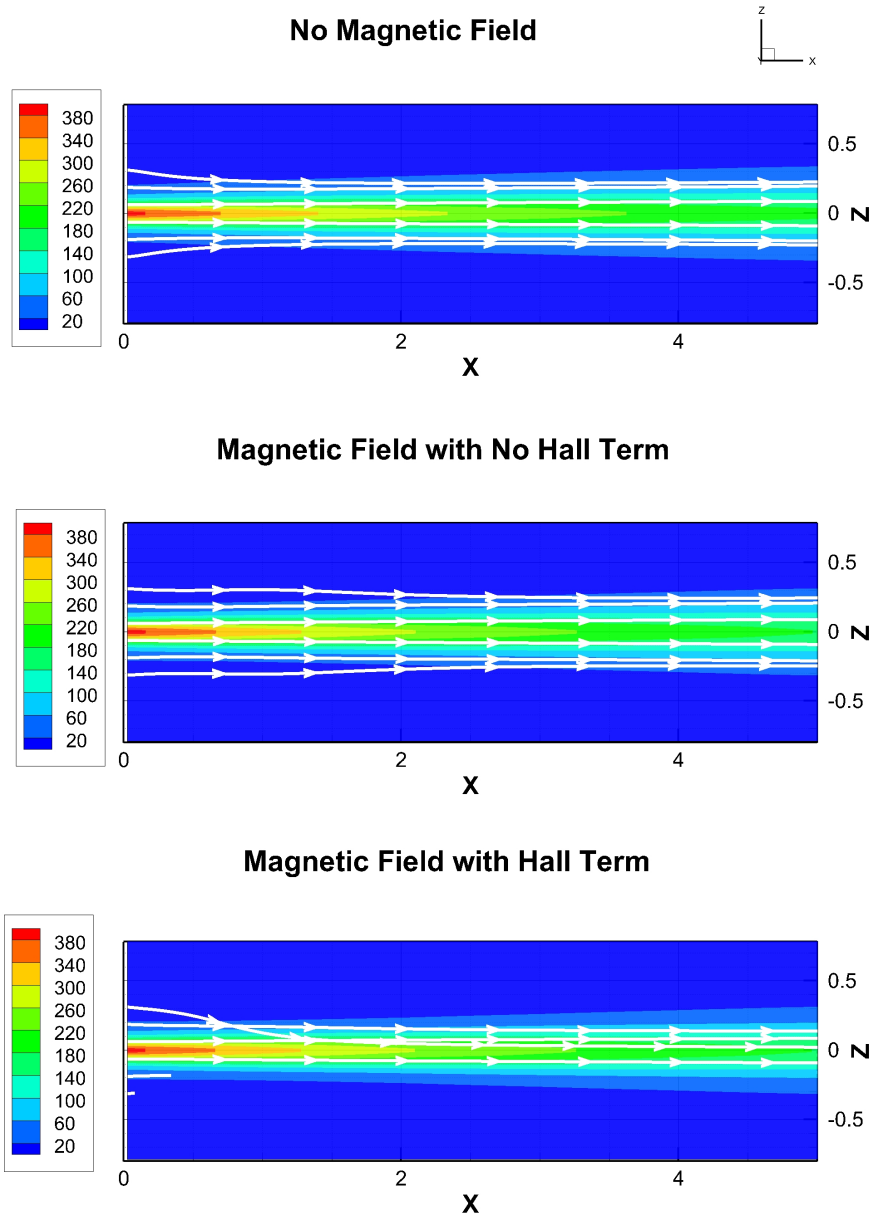

Figure 7.5: Velocity magnitude (m/s) contours on $\hat{y}$ mid-plane with velocity streamlines.

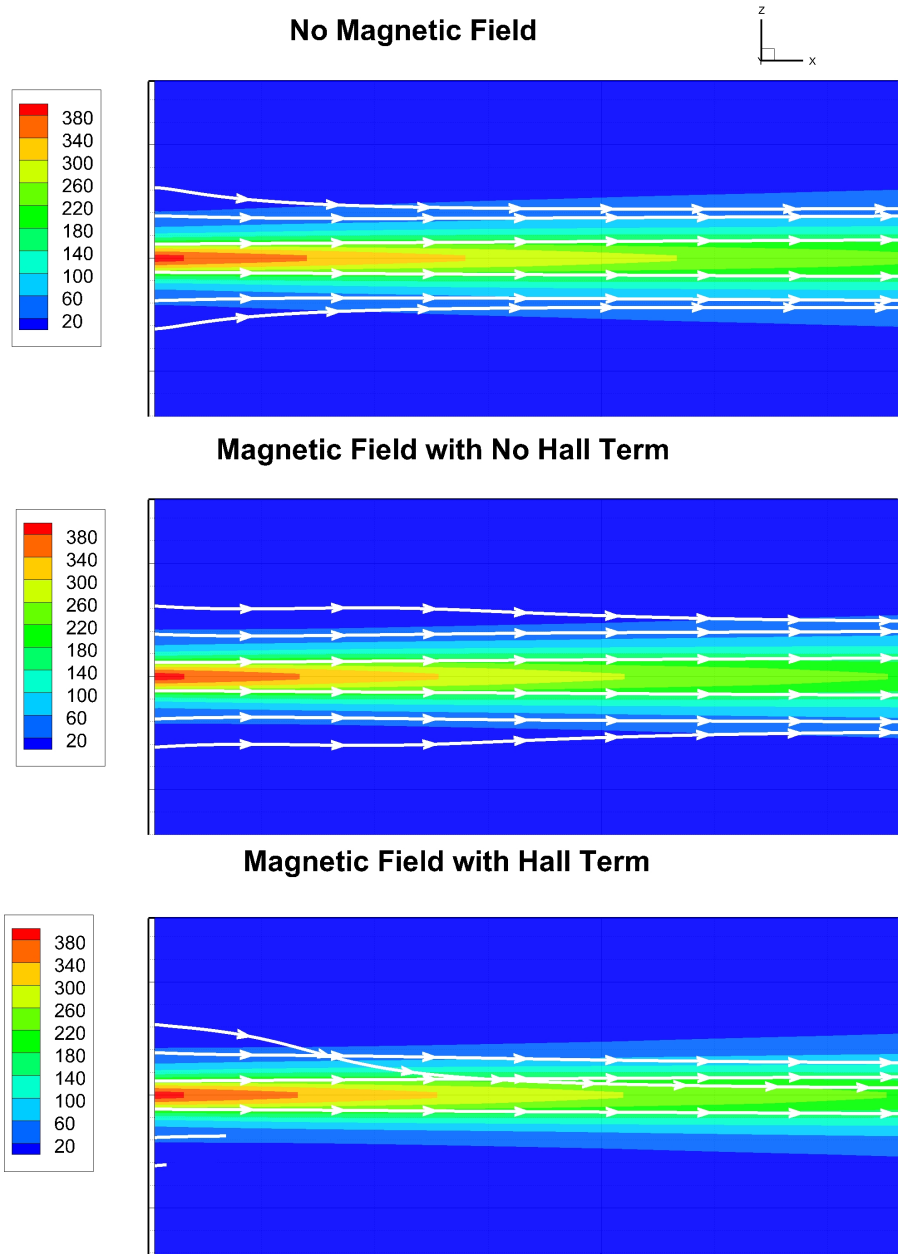

Figure 7.6: Zoomed in view of velocity magnitude (m/s) contours on $\hat{y}$ mid-plane with velocity streamlines.

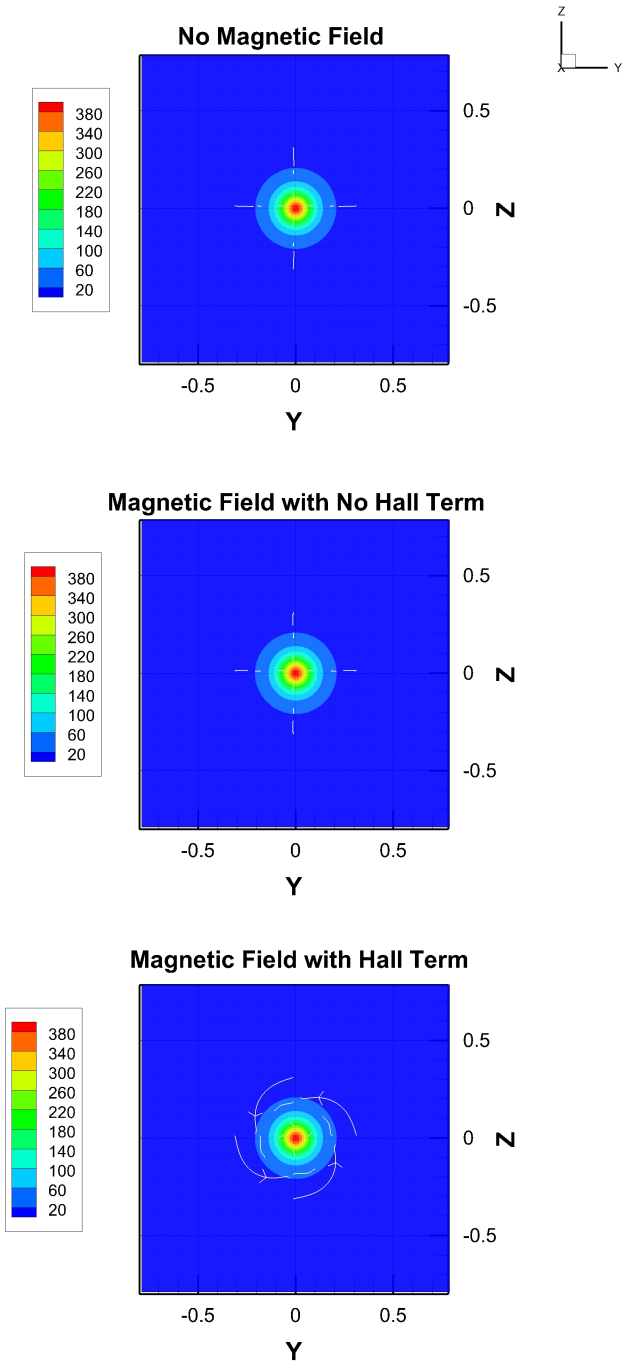

Figure 7.7: Velocity magnitude (m/s) contours on $\hat{x}$ inlet-plane with velocity streamlines.

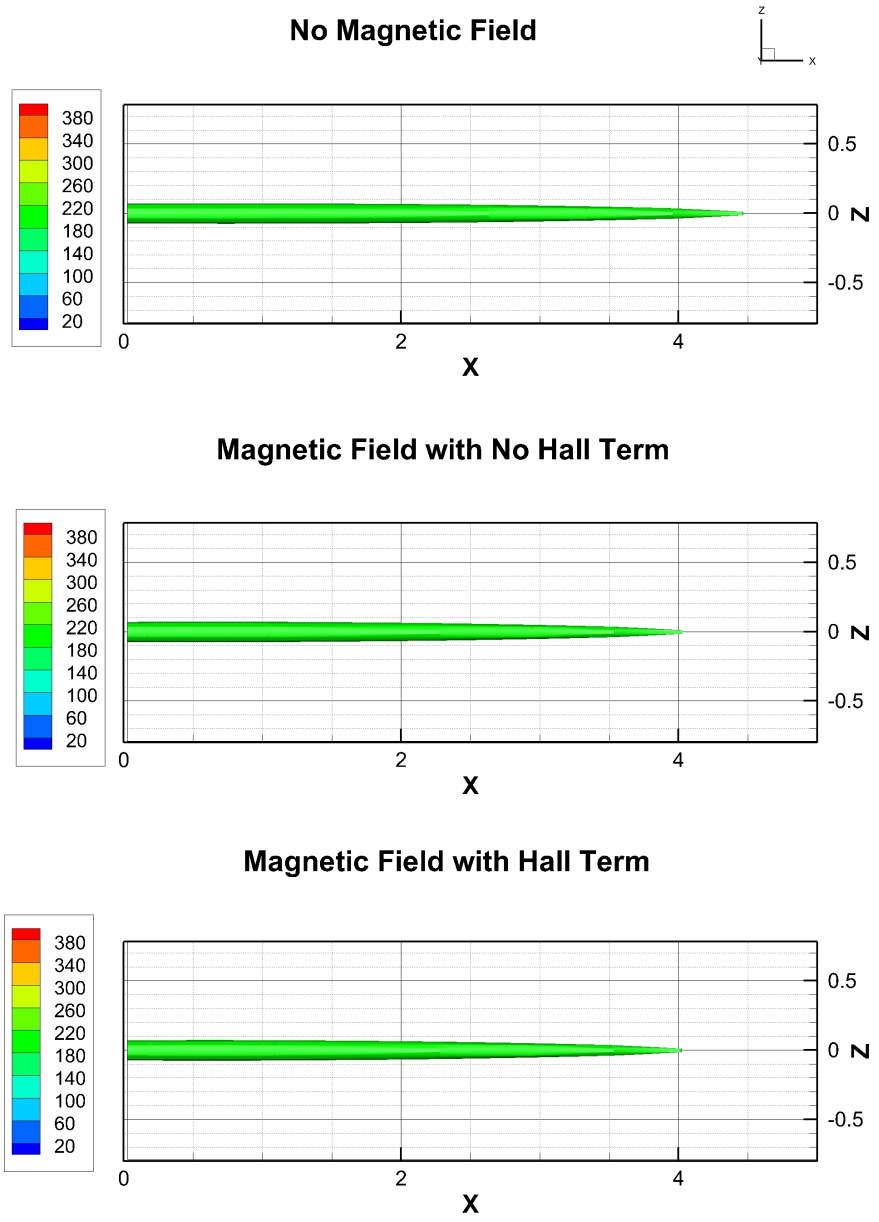

Figure 7.8: Velocity magnitude iso-surfaces for $U = 200\ m/s$

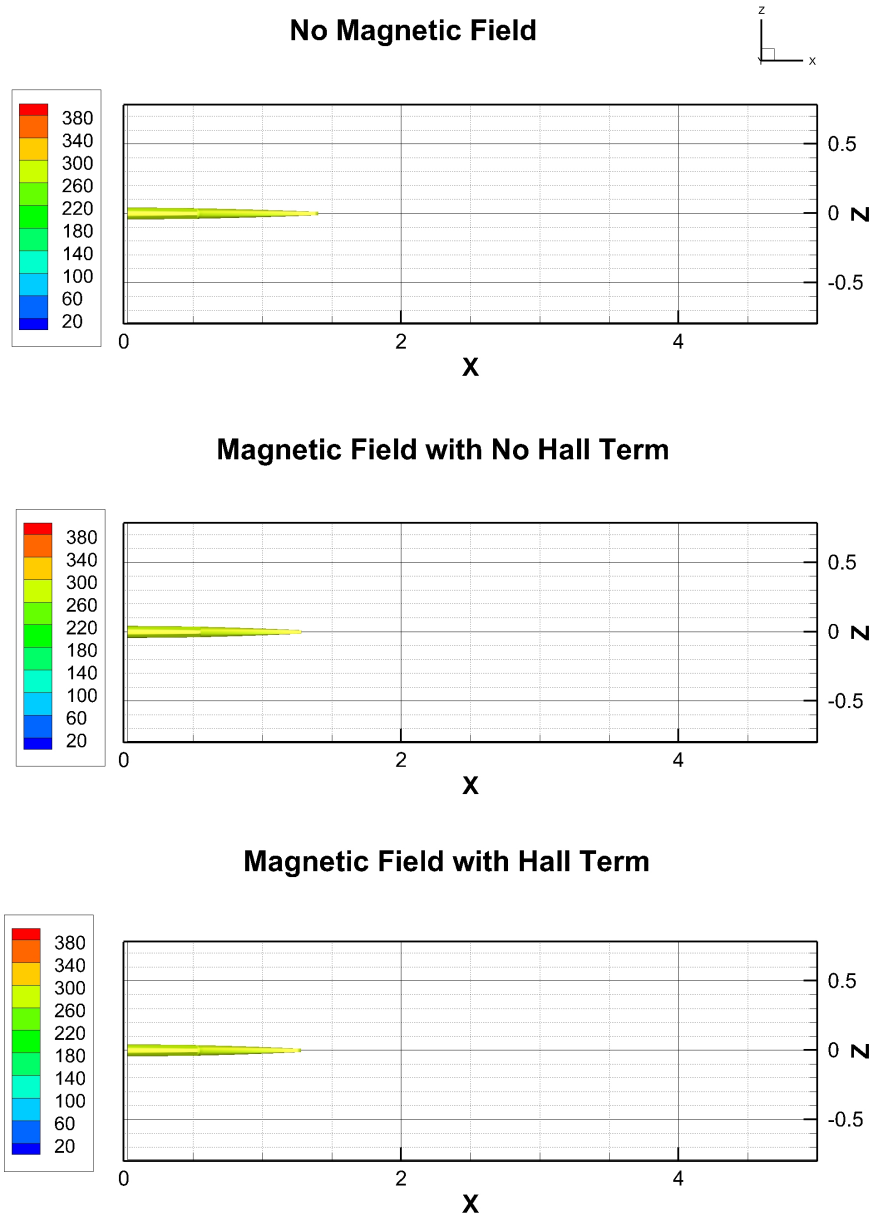

Figure 7.9: Velocity magnitude iso-surfaces for $U = 300\ m/s$.

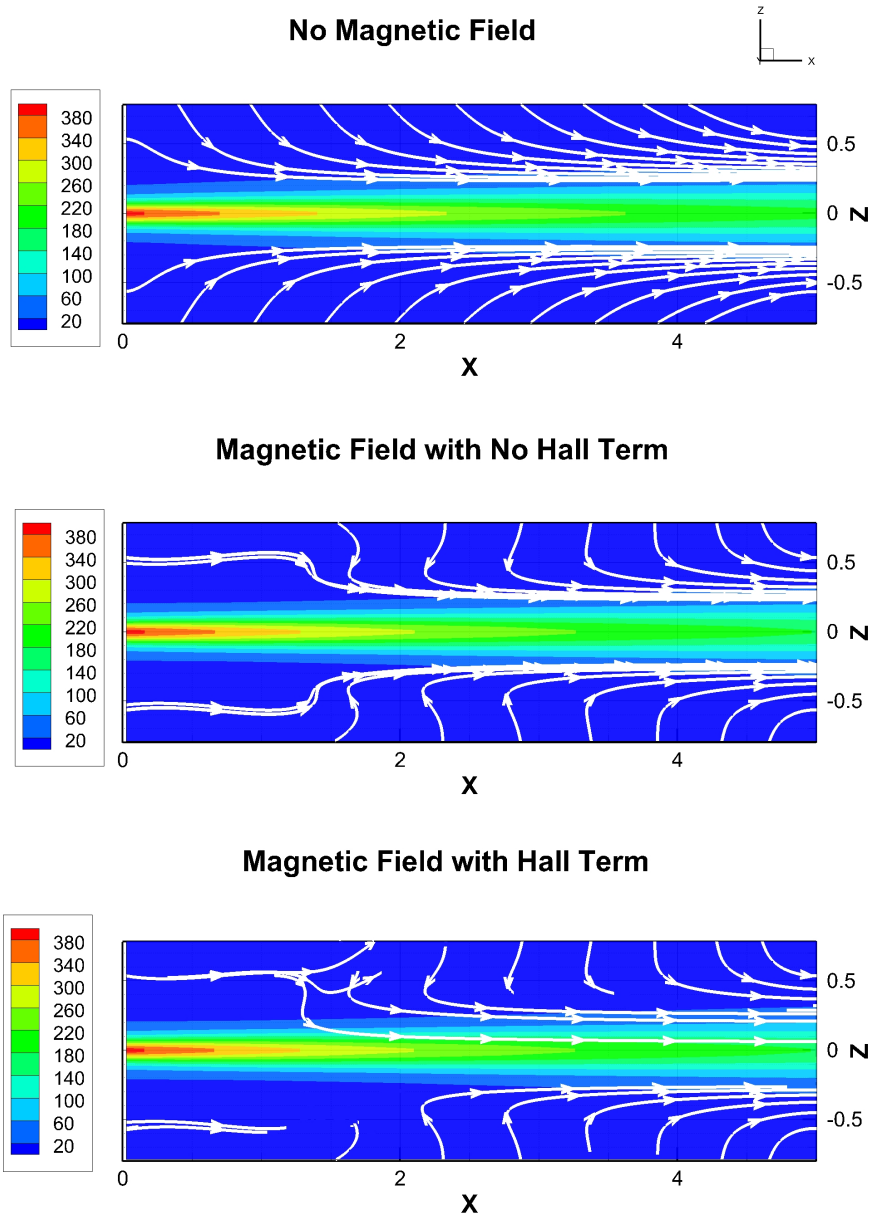

Figure 7.10: Velocity magnitude (m/s) contours on$\hat{y}$ mid-plane with velocity entrainment streamlines.

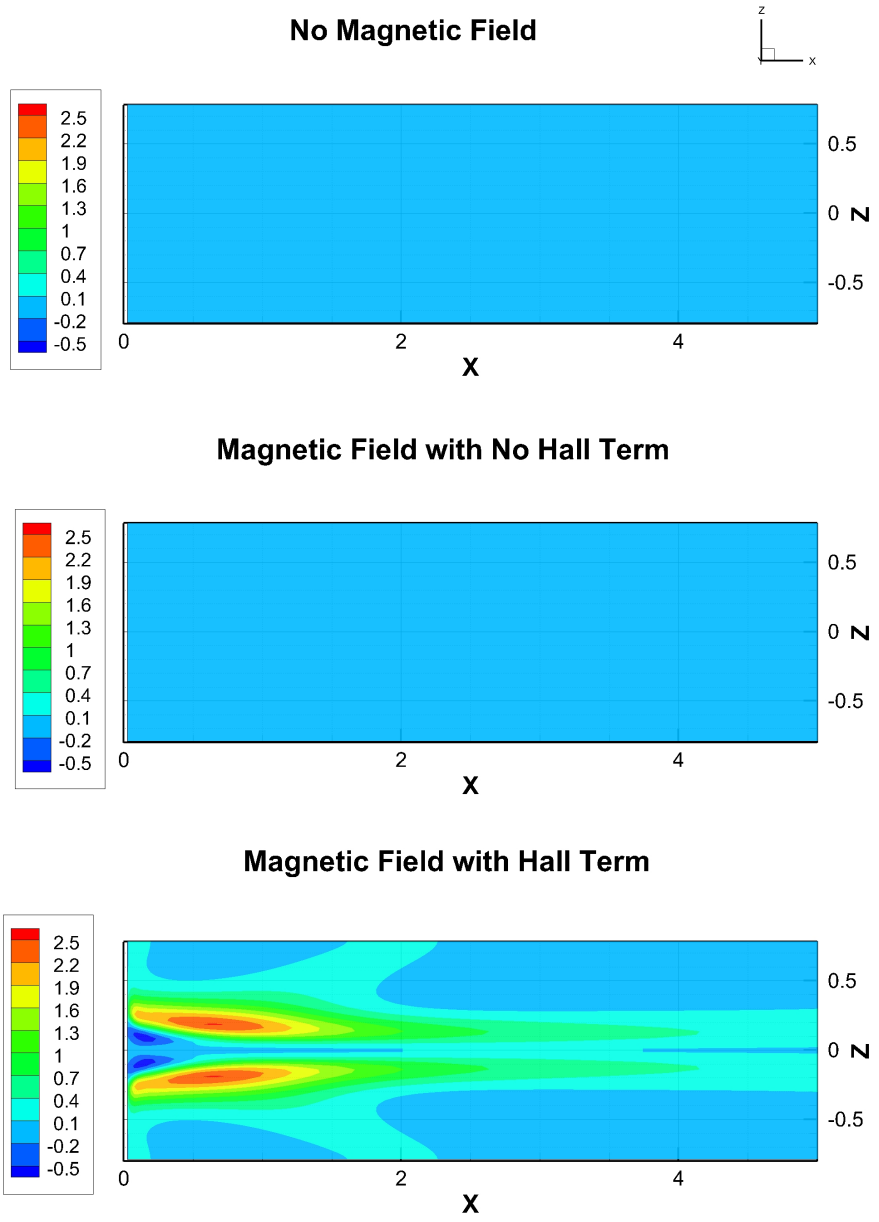

Figure 7.11: Azimuthal, $\hat{\theta}$, velocity (m/s) of the plasma jet

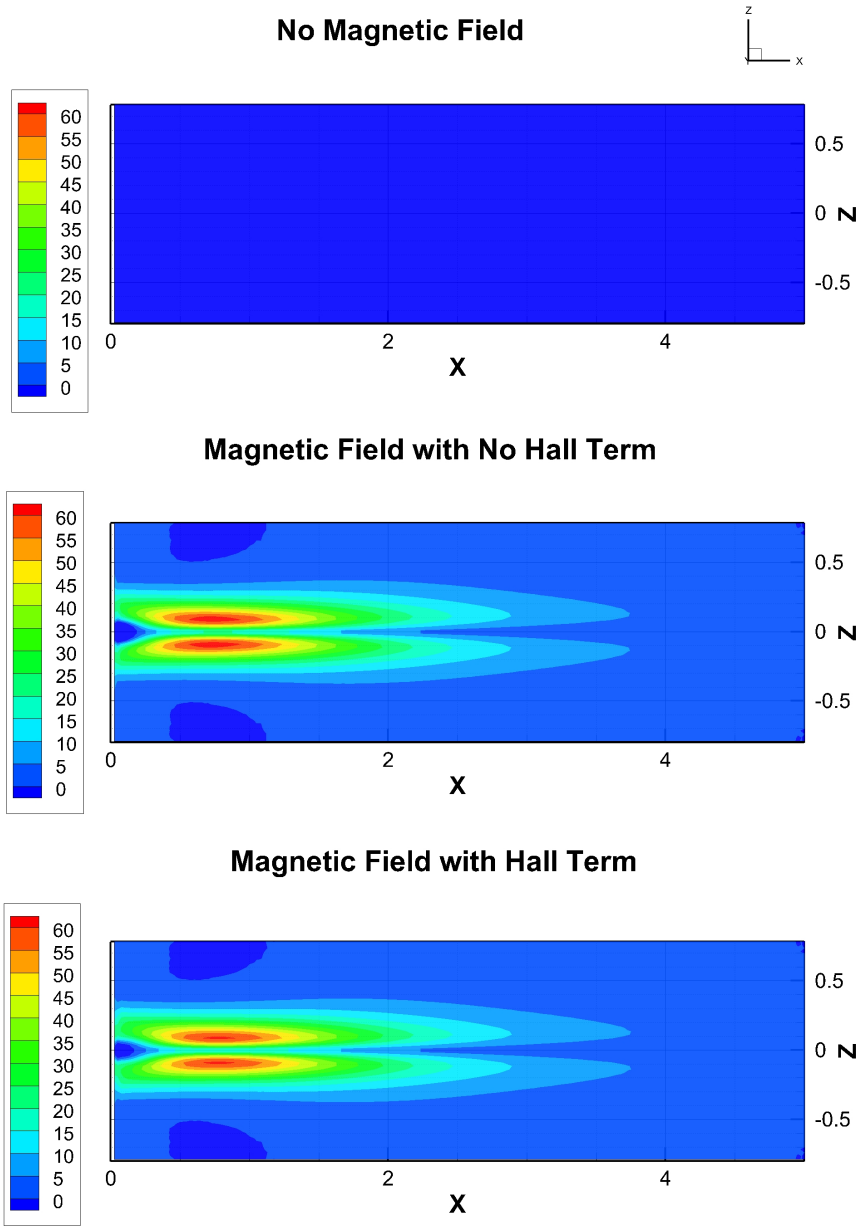

Figure 7.12: Azimuthal, $\hat{\theta}$, currents of the plasma jet

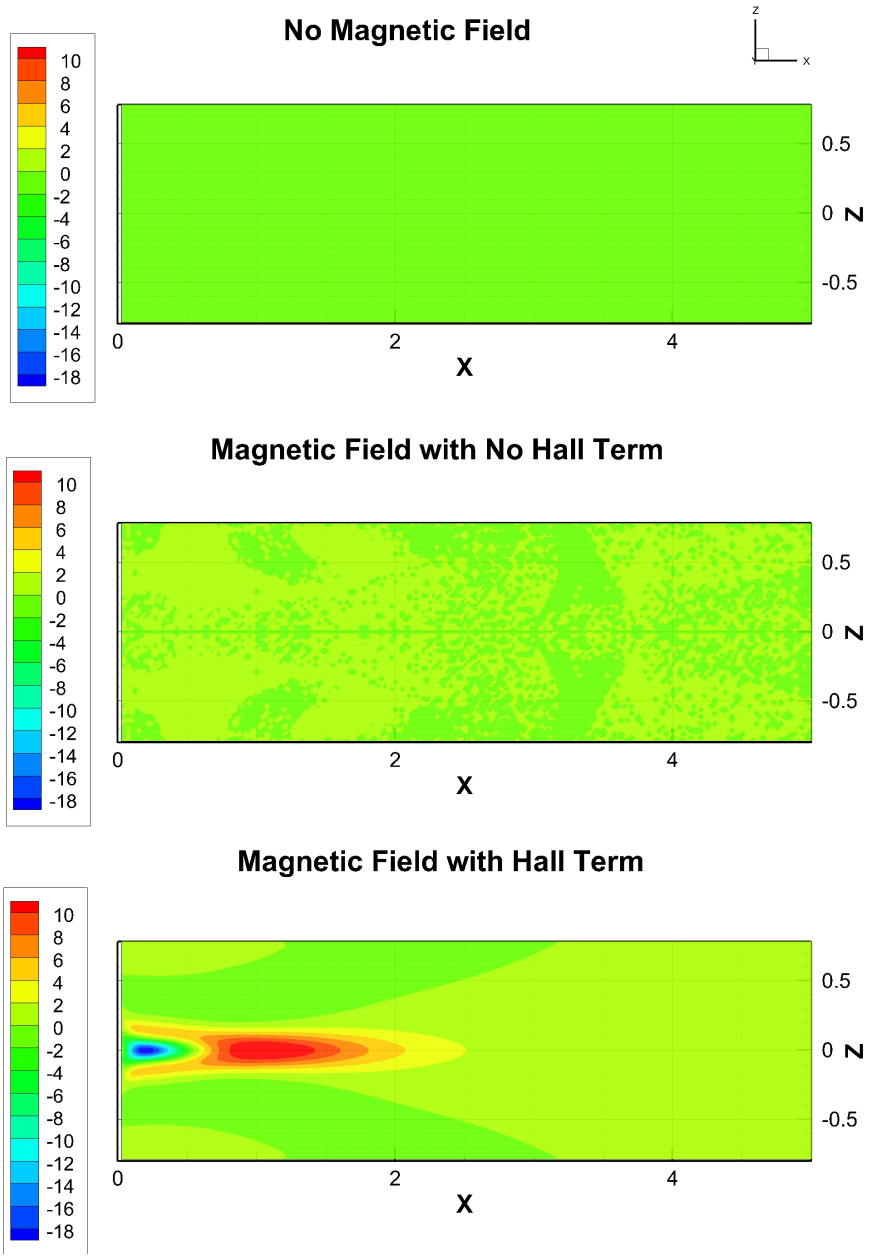

Figure 7.13: Axial, $\hat{x}$, currents of the plasma jet

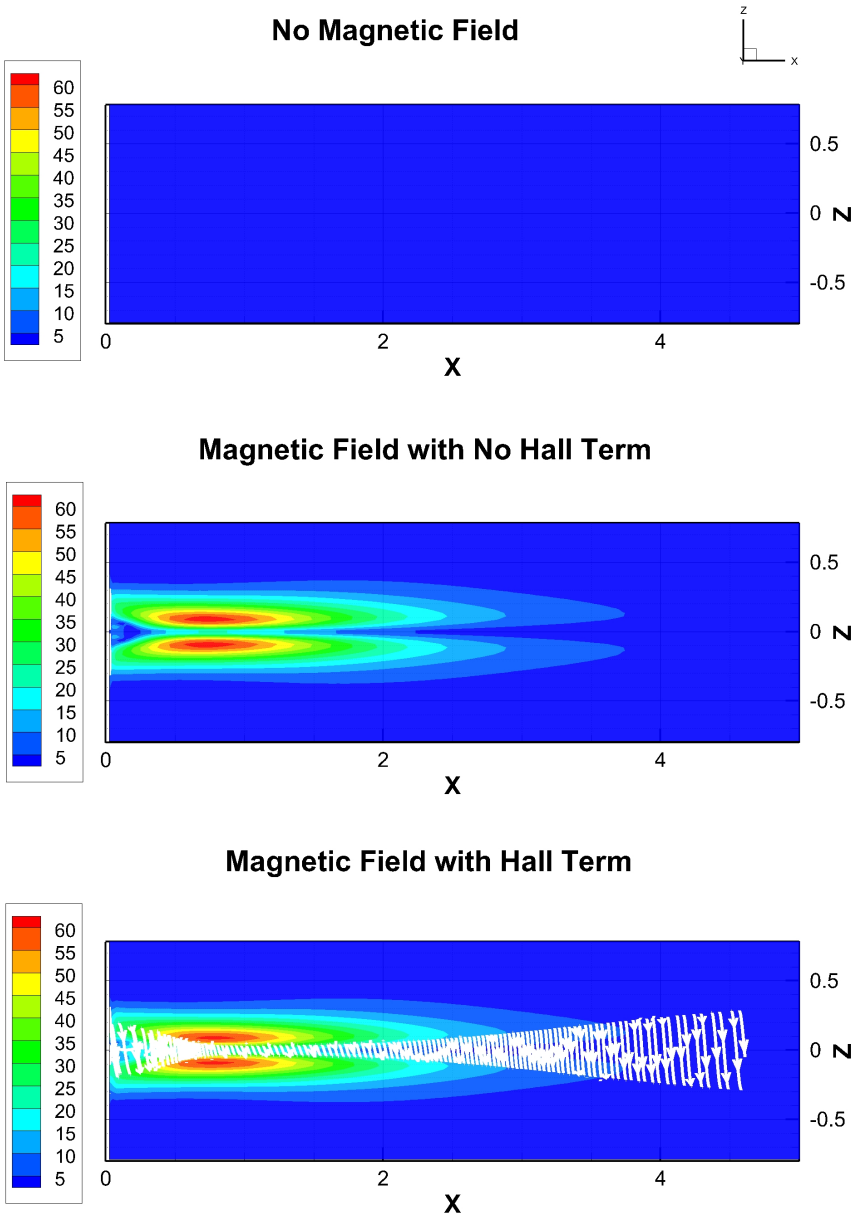

Figure 7.14: Induced current magnitude contours on $\hat{y}$ mid-plane with current stream lines

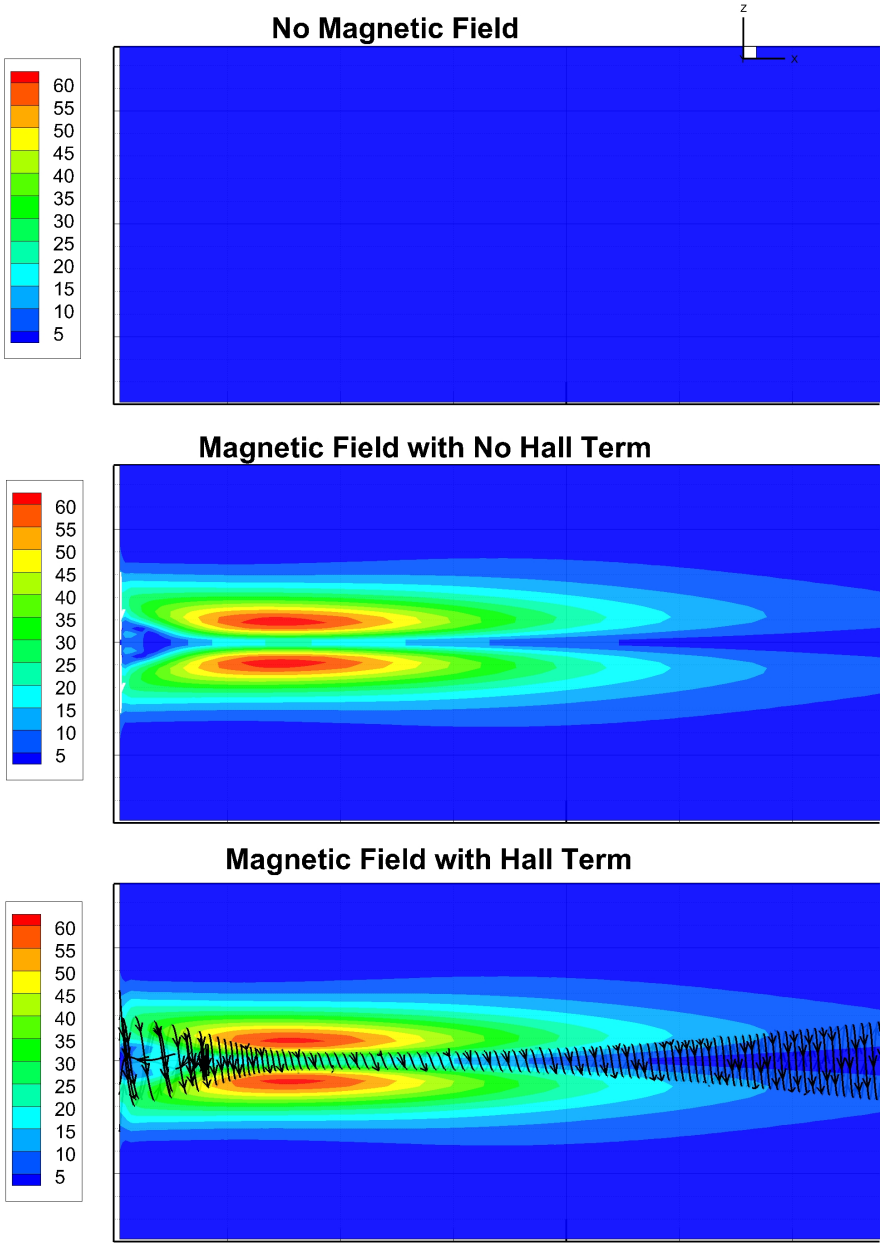

Figure 7.15: Zoom of induced current magnitude contours on $\hat{y}$ mid-plane with current stream lines

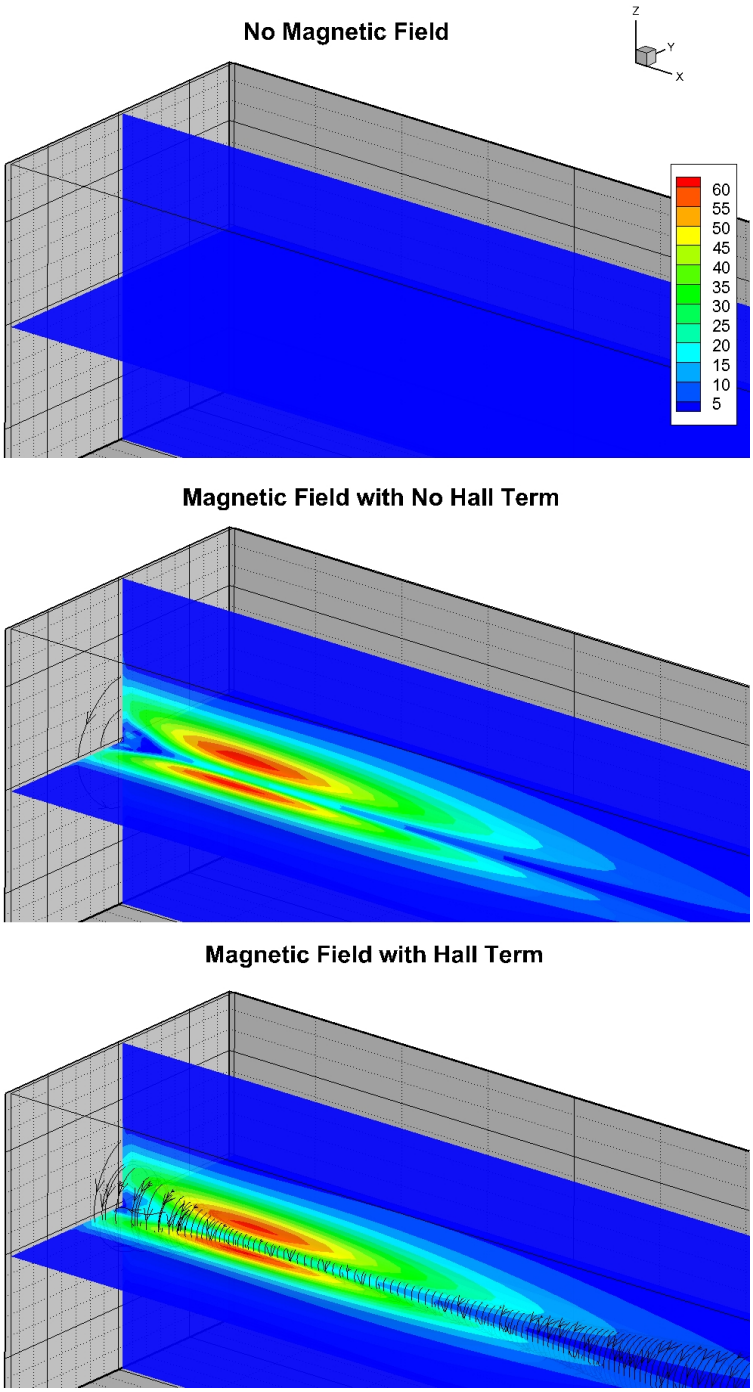

Figure 7.16: Zoomed 3D view of induced current magnitude contours with current stream lines

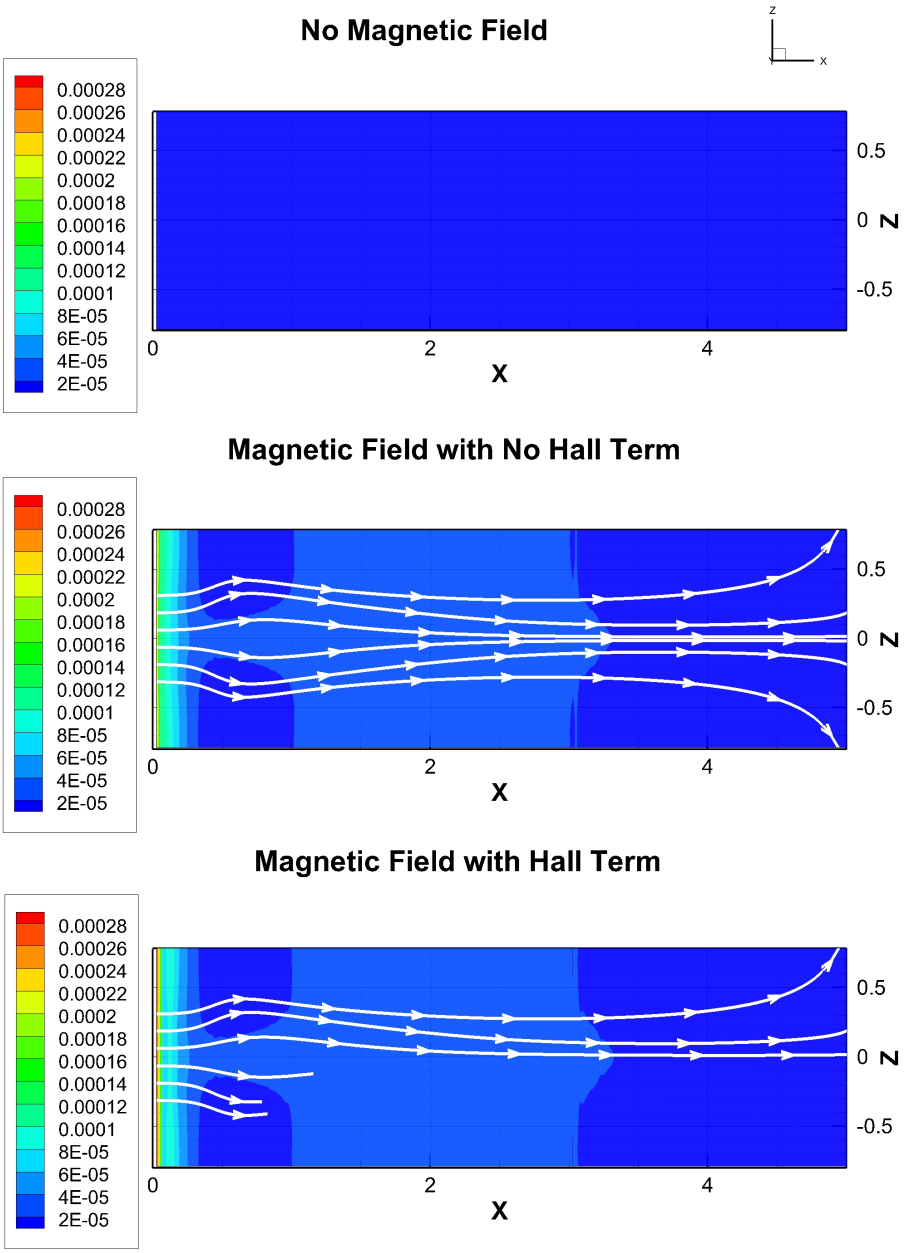

Figure 7.17: Magnitude of the induced magnetic field (T) contours with induced field streamlines.

7.5.1 Numerical Convergence and the Divergence of B

Grid convergence was completed when possible and qualitative behavior remained consistent as grids were refined. Small quantitative difference are measurable as the grids are refined, but computational restrictions did not enable finer grids and time steps to be run. A major computational limitation of the Hall term results from the Whistler wave characteristic time which goes as $1/\Delta x^2$. This severely limits further grid refinement. Computational effort goes as $1/\Delta x^3$ as the spatial dimension is refined, this also requires refinement of the time step, which with the Hall term results in a total computational effort increasing as $1/\Delta x^5$. Thus in the case of the Hall term, halving the grid size increases the total computational effort by 32 times.

Numerical errors in the $\nabla \cdot B$ were still present in the studied cases. These numerical errors were greatest at the inlet boundary as shown in Figure 7.18 and are likely caused by the boundary condition not explicitly satisfying $\nabla \cdot B$. In this figure the $\nabla \cdot B$ error is non-dimensionalized by the magnetic field strength and the domain length. Figure 7.19 shows that with finer time steps the error in $\nabla \cdot B$ decreases when test cases are run out to the same total time. The results shown are for the same grid-size as the previously presented results. Similar behavior is evident when refining the grid of the domain. This indicates that with finer grids and smaller time steps the error would decrease further, as it should. A concern however is shown in Figure 7.20 in which the $\nabla \cdot B$ increases in run time. We believe this is due to the numerical error at the boundary feeding into the domain and slowly increasing the total volume averaged error.

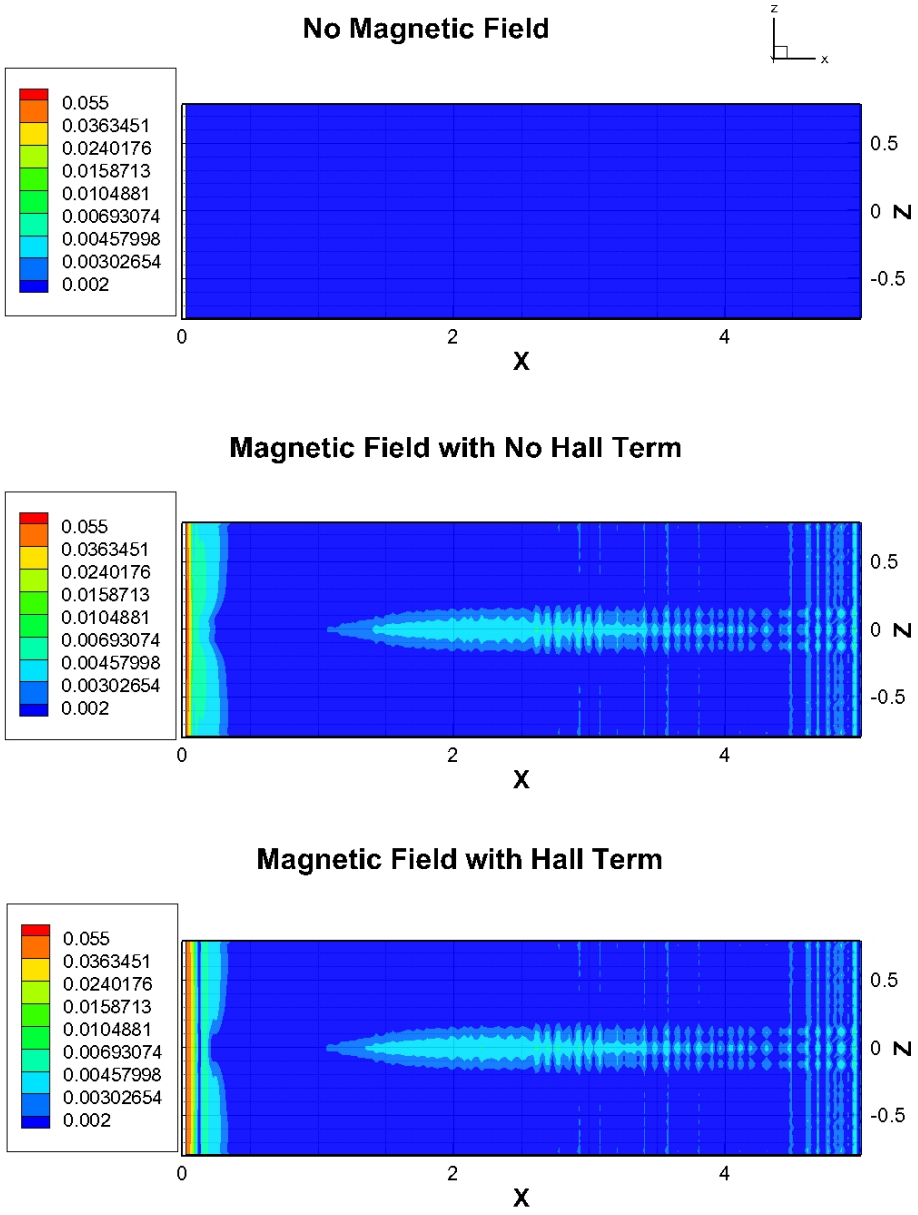

Figure 7.18: Contours of non-dimensionalized $\nabla \cdot B$ errors

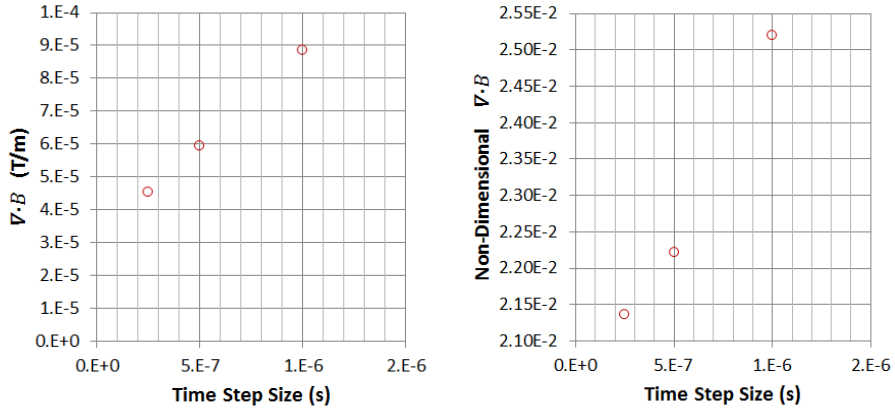

Figure 7.19: Left: Volume average $\nabla \cdot B$ with decreasing time step, Left: Volume average non-dimensional $\nabla \cdot B$ with decreasing time step

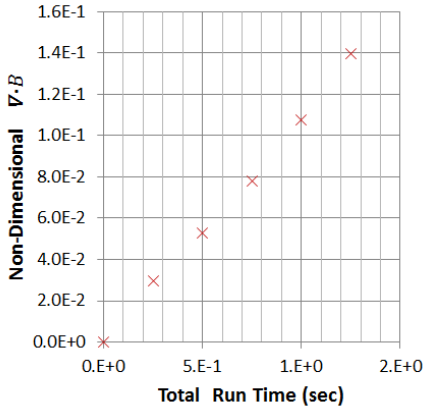

Figure 7.20: Volume average non-dimensional $\nabla \cdot B$ in time

7.5.2 Discussion

The Hall effect plasma jet results confirmed the hypothesis presented at the beginning of this section and showed azimuthal velocities due to the Hall effect in diverging magnetic field plasma jets. These azimuthal rotations are best explained by the additional induced axial currents and the resulting $J \times B$ forces. Radial cur-

rents were also found and may contribute significantly to rotational $J \times B$ forces. However, the structure of these radial currents was not as defined as that of the axial currents and conclusions are more difficult to make. Future cases should be run with finer meshes and times steps to refine quantitatively this physical behavior and reduce $\nabla \cdot B$ error. We have demonstrated qualitative agreement with mesh refinement but additional work remains to be done. Multiple cases were studied with different magnetic field strengths and inlet velocities showing consistent physical behavior. *We conclude that Hall effects in plasma jets with a diverging magnetic field produce helical structures in the velocity, magnetic, and current fields.*

Additional work should be done to characterize the magnitude of the induced azimuthal velocities as a function of the flow parameters. In a magnetic nozzle problem these induced azimuthal velocities may attribute to another loss mechanism for the directed kinetic energy. Enabling the cross field flow of ions may also help better describe the detachment phenomena. It is difficult to relate these numerical results to those of the magnetic nozzle experiments because the plasmadynamics will be significantly different in a super-sonic jet expansion. Further development of the solver is necessary to study these flows. The interaction of the supersonic jet expansion and the Hall effect may cause complex behavior which is difficult to predict as is evidenced by the Hall MHD shock-tube problem. The results from this study imply that the Hall effect should still generate some helical structures due to the diverging field.

8. CONCLUSIONS

This chapter briefly summarizes the work performed in this thesis. This work can be divided into contributions from: i) theoretical study, ii) solver development, and iii) numerical experiment results. Recommendations are made for future work in studying magnetic nozzle physics and MGKM solver development.

8.1 Contributions from Theoretical Study

The theoretical work of this thesis identified the crucial physics of magnetic nozzles and characterized the validity of magnetohydrodynamics to studying magnetic nozzle plasmas. We compiled a thorough and concise summary of the state of magnetic nozzle physics and identified that to advance the field further a joint approach of physical and numerical experiments is necessary to confirm or debunk current theories. We established that magnetic nozzles operate on the edge of the continuum regime and that magnetohydrodynamics can be used to study some of the current operating regimes of magnetic nozzles. More complex transport properties may be used to further extend the validity of MHD. We also showed that a generalized Ohm's law MHD solver is necessary to capture all the relevant physics in magnetic nozzles.

8.2 Contributions to Solver Development

The Magneto-Gas Kinetic Method was further developed by including Hall effects. Inclusion of Hall effects led to inclusion of a sub-cycling sub-routine which iterates separately over the Hall term. The primary reason for this is due to the very restrictive time step constraint of the Whistler Wave characteristic. The electron pressure term was also added to include the full generalized Ohm's law, but contributions due to this term have not been validated due to time constraints and

the difficulty in finding comparable results. Electron pressure effects were minimal in most cases ran due to either studying 1D and 2D problems or operating in incompressible regimes. In these regimes the electron pressure term is often negligible. Further solver development was inhibited by the inherent complexity of the Hall term computationally and physically.

The validation of MGKM in the compressible regime through the shock-tube flows and in the Hall effect regime through Hartmann flows further extends the operating regimes in which we are confident of MGKM results.

8.3 Contributions from Numerical Experiment Results

The primary original contribution of this research comes from the novel study of the effects of the Hall term in 1D, 2D, and 3D flows and the consistent behavior that it exhibits between these flows. Shock-tube flows with the Hall term have been previously studied with numerical experiments and our results showed good agreement with the relevant results in literature. Hartmann flows with the Hall term have been studied theoretically with semi-analytical solutions presented, but a lack of numerical studies is evident in literature. Our numerical study is unique in its scope and has confirmed the predicted analytical behavior with numerical results. MHD studies of magnetic nozzles have wholly neglected the effects of the Hall term. We have shown that this term may become important in our dimensional analysis and have characterized some of the effects of the Hall term through our numerical experiments. The novel numerical experiments performed in this research confirm theoretical predictions of the anticipated Hall effects in magnetic nozzle regimes and are an original contribution to the study of magnetic nozzle physics. It is our conclusion that in magnetic nozzles the Hall effect creates helical structures in the velocity, magnetic, and current fields.

8.4 Recommended Future Work

To conclude this thesis we would like to include a list of possible future work both in MGKM development and magnetic nozzle physics studies.

1. Rewrite "magnetic" portion of MGKM as a finite volume solver instead of a finite difference solver. This will enable better interaction between the "fluid" and "magnetic" portions of the code and will allow more consistent boundary conditions to be implemented. Finite volume implementation will also help with integrating non-uniform grids which will be necessary for future test cases. This may also help with numerical $\nabla \cdot B$ errors that occur at the boundary and will enable use of the WENO limiter for the magnetic field.

2. Development of MGKM for non-uniform grids. This will enable more complex problems to be studied while minimizing computational effort.

3. The $\nabla \cdot B$ errors should be further addressed and a thorough study of the appropriate boundary conditions which minimize numerical error should be done. Toth (2000) addresses this issue primarily for finite volume solvers and is a good resource for further development. [61]

4. Implementation of logarithmic variables for ρ and T as suggested by Shebalin [53] will enable jet expansion cases to be studied and eliminate numerical errors of negative densities and temperatures. These numerical errors were the primary reason why jet expansion cases could not be studied.

5. Increase numerical accuracy and functionality of "magnetic" portion of MGKM by including higher order time integration (ex. Runge-Kutta) or higher order spatial derivatives. Some preliminary work was done with second order time integration of the "magnetic" portion, but no definitive results are presented.

6. Utilize functions for discretization instead of hard-coding each, this will enable more efficient code writing and will allow for simple changes to go to higher order schemes.

7. Restructure the code in such a way that the entire code does not need to be compiled to perform runs, instead using external input files to select boundary conditions, initial conditions, and numerical solver options.

8. Possible physics extensions of the code include: multi-fluid solver, variable transport properties, and directional transport properties. Implementation of more complex transport properties requires re-derivation of some MHD equations, particularly the induction equation.

9. I believe the next step for MGKM would be to perform a plasma jet expansion problem. It will be computationally more feasible to first ignore Hall physics and focus on developing a solver which is able to handle super-sonic jet expansions.

REFERENCES

[1] E. Ahedo and M. Merino. Preliminary assessment of detachment in a plasma thruster magnetic nozzle. AIAA-2010-6613, Nashville, TN, July 2010.

[2] E. Ahedo and M. Merino. On plasma detachment in propulsive magnetic nozzles. *Physics of Plasmas*, 18:053504, 2011.

[3] D.B. Araya. Resistive mhd simulations of laminar round jets with applications to magnetic nozzle flows. Master's thesis, Texas A&M University, 2011.

[4] D.B. Araya, S.S. Girimaji, M.D. Carter, and C.S. Olsen. Parameterization of magnetic nozzle flow physics for an in-space propulsion application. AIAA-2011-4010, Honolulu, HI, June 2011.

[5] A.V. Arefiev and B.N. Breizman. Theoretical components of the vasimr plasma propulsion concept. *Physics of Plasmas*, 11:2942, 2004.

[6] A.V. Arefiev and B.N. Breizman. Magnetohydrodynamic scenario of plasma detachment in a magnetic nozzle. *Physics of Plasmas*, 12:043504, 2005.

[7] A.V. Arefiev and B.N. Breizman. Ambipolar acceleration of ions in a magnetic nozzle. *Physics of Plasmas*, 15:042109, 2008.

[8] P.M. Bellan. *Fundamentals of Plasma Physics*. Cambridge University Press, Cambridge, 2006.

[9] SI Braginskii. Transport processes in a plasma. *Reviews of Plasma Physics*, 1:205, 1965.

[10] BN Breizman, MR Tushentsov, and AV Arefiev. Magnetic nozzle and plasma detachment model for a steady-state flow. *Physics of Plasmas*, 15:057103, 2008.

[11] N. Brenning, T. Hurtig, and M.A. Raadu. Conditions for plasmoid penetration across abrupt magnetic barriers. *Physics of Plasmas*, 12:012309, 2005.

[12] M. Brio and C.C. Wu. An upwind differencing scheme for the equations of ideal magnetohydrodynamics. *Journal of Computational Physics*, 75(2):400–422, 1988.

[13] F.R. Chang-Diaz. The vasimr rocket. *Scientific American*, 283(5):90–97, 2000.

[14] F.F. Chen. *Introduction to Plasma Physics and Controlled Fusion*, volume 1. Plenum Press, New York, 1984.

[15] S.A. Cohen and M.A. Paluszek. The grand challenge- a new plasma thruster. *Launchspace*, 3(6):46, 1998.

[16] S.A. Cohen, NS Siefert, S. Stange, RF Boivin, EE Scime, and FM Levinton. Ion acceleration in plasmas emerging from a helicon-heated magnetic-mirror device. *Physics of Plasmas*, 10:2593, 2003.

[17] P.A. Davidson. *An Introduction to Magnetohydrodynamics*, volume 25. Cambridge University Press, Cambridge, 2001.

[18] C. Deline, G. Chavers, and B. Gilchrist. Physics of plasma detachment in a magnetic nozzle. AIAA-2006-4653, Sacramento, CA, July 2006.

[19] C. Deline, B. Gilchrist, R. Bengtson, J. Jones, G. Chavers, and C. Dobson. Simulation and measurement of high-beta plasma in a magnetic nozzle. AIAA-2007-5259, Cincinnati, OH, July 2007.

[20] C.A. Deline, R.D. Bengtson, B.N. Breizman, M.R. Tushentsov, J.E. Jones, D.G. Chavers, C.C. Dobson, and B.M. Schuettpelz. Plume detachment from a magnetic nozzle. *Physics of Plasmas*, 16:033502, 2009.

[21] GI Dimov and S.Y. Taskaev. Simulation of a supersonic plasma jet with recombination in a magnetic nozzle. 27th European Physical Society Conference on Controlled Fusion and Plasma Physics, Budapest, June 2000.

[22] F. Ebersohn, S.S. Sharath, D. Staack, and J. Shebalin. Towards computation of resistive magnetohydrodynamic magnetic nozzle plasma flow. AIAA-2012-3841, Atlanta, GA, July 2012.

[23] F. Ebersohn, S.S. Sharath, D. Staack, J. Shebalin, B. Longmier, and C. Olsen. Magnetic nozzle plasma plume: Review of crucial physical phenomena. AIAA-2012-4274, Atlanta, GA, July 2012.

[24] R.A. Gerwin, G.J. Marklin, A.G. Sgro, and A.H. Glasser. Characterization of plasma flow through magnetic nozzles. Technical report, DTIC Document, 1990.

[25] F.N. Gesto, B.D. Blackwell, C. Charles, and R.W. Boswell. Ion detachment in the helicon double-layer thruster exhaust beam. *Journal of Propulsion and Power*, 22(1):24–30, 2006.

[26] EB Hooper. Plasma detachment from a magnetic nozzle. *Journal of Propulsion and Power*, 9(5):757–763, 1993.

[27] R.P. Hoyt, J.T. Scheuer, K.F. Schoenberg, R.A. Gerwin, R.W. Moses Jr, and I. Henins. Magnetic nozzle design for coaxial plasma accelerators. *Plasma Science, IEEE Transactions on*, 23(3):481–494, 1995.

[28] J. Huba. Hall magnetohydrodynamics-a tutorial. *Space plasma simulation*, pages 166–192, 2003.

[29] J.D. Huba. Nrl: plasma formulary. Technical report, DTIC Document, 2004.

[30] A.V. Ilin, F.R. Chang Diaz, J.P. Squire, A.G. Tarditi, B.N. Breizman, and M.D. Carter. Simulations of plasma detachment in vasimr. AIAA-2002-0346, Reno, NV, January 2002.

[31] M. Inutake, A. Ando, K. Hattori, H. Tobari, and T. Yagai. Characteristics of a supersonic plasma flow in a magnetic nozzle. *J. Plasma Fusion Res.*, 78:1352–1360, 2002.

[32] M. Inutake, K. Hattori, A. Ando, F. Hori, T. Sugirnura, K. Fukushi, T. Ochiai, M. as aya Yamamoto, T. Yagai, A. Imasaki, et al. Supersonic plasma flow in a magnetic nozzle. Proc. of the 26th IEPC, 1999.

[33] R.G. Jahn and W. von Jaskowsky. *Physics of Electric Propulsion*, volume 288. McGraw-Hill, New York, 1968.

[34] DA Kaufman, DG Goodwin, and JC Sercel. Plasma separation from magnetic field lines in a magnetic nozzle. volume 1 of *31st AIAA Aerospace Sciences Meeting and Exhibit*, 1993.

[35] J. Kerimo and S.S. Girimaji. Boltzmann–bgk approach to simulating weakly compressible 3d turbulence: comparison between lattice boltzmann and gas kinetic methods. *Journal of Turbulence*, (8), 2007.

[36] RA Kopp and GW Pneuman. Magnetic reconnection in the corona and the loop prominence phenomenon. *Solar Physics*, 50(1):85–98, 1976.

[37] HG Kosmahl. Three-dimensional plasma acceleration through axissymmetric divergine magnetic fields based on dipole moment approximation. Technical report, National Aeronautics and Space Administration,Lewis Research Center, Cleveland, OH, 1967.

[38] K. Kuriki and O. Okada. Experimental study of a plasma flow in a magnetic nozzle. *Physics of Fluids*, 13:2262, 1970.

[39] J.M. Little and E.Y. Choueiri. Divergence of a propulsive plasma flow expanding through a magnetic nozzle. In *31st International Electric Propulsion Conference*, 2009.

[40] J.M. Little and E.Y. Choueiri. The influence of induced currents on magnetic nozzle acceleration and plasma detachment. AIAA-2010-6615, Nashville, TN, July 2010.

[41] J.M. Little and E.Y. Choueiri. Plasma detachment and momentum transfer in magnetic nozzles. AIAA-2011-6001, San Diego, CA, July 2011.

[42] B.W. Longmier, E.A. Bering, M.D. Carter, L.D. Cassady, W.J. Chancery, F.R.C. Díaz, T.W. Glover, N. Hershkowitz, A.V. Ilin, G.E. McCaskill, et al. Ambipolar ion acceleration in an expanding magnetic nozzle. *Plasma Sources Science and Technology*, 20:015007, 2011.

[43] B.W. Longmier, L.D. Cassady, M.G. Ballenger, M.D. Carter, F.R. Chang-Díaz, T.W. Glover, A.V. Ilin, G.E. McCaskill, C.S. Olsen, J.P. Squire, et al. Vx-200 magnetoplasma thruster performance results exceeding fifty-percent thruster efficiency. *Journal of Propulsion and Power*, 27(4):915, 2011.

[44] H. Lorzel and P.G. Mikellides. Three-dimensional modeling of magnetic nozzle processes. *AIAA Journal*, 48(7):1494–1503, 2010.

[45] M. Merino and E. Ahedo. Plasma detachment mechanisms in a magnetic nozzle. AIAA-2011-5999, July 2011.

[46] R.W. Moses Jr, R.A. Gerwin, and K.F. Schoenberg. Resistive plasma detachment in nozzle based coaxial thrusters. In *AIP Conference Proceedings*, volume 246, page 1293, 1992.

[47] M. Nagatomo. Plasma acceleration by high frequency electromagnetic wave in static magnetic field gradient. AIAA-67-660, Colorado Springs, CO, September 1976.

[48] H. Sato. The hall effect in the viscous flow of ionized gas between parallel plates under transverse magnetic field. *J. Phys. Soc. Japan*, 16(7):1427, 1961.

[49] H. Schlichting, K. Gersten, and K. Gersten. *Boundary-layer theory*. Springer Verlag, 2000.

[50] PF Schmit and NJ Fisch. Magnetic detachment and plume control in escaping magnetized plasma. *Journal of Plasma Physics*, 75(03):359–371, 2009.

[51] K. Schoenberg, R. Gerwin, C. Barnes, I. Henins, R. Mayo, and R. Moses. Coaxial plasma thrusters for high specific impulse propulsion. In *AIAA, NASA, and OAI, Conference on Advanced SEI Technologies, Cleveland, OH*, page 1991, 1991.

[52] J.C. Sercel. Simple model of plasma acceleration in a magnetic nozzle. In *AIAA, DGLR, and JSASS, 21st International Electric Propulsion Conference*, volume 1, 1990.

[53] J.V. Shebalin. Pseudospectral simulation of shock-turbulence interactions. *AIAA Journal*, 31(12):2378, 1993.

[54] J.V. Shebalin. Størmer regions for axisymmetric magnetic multipole fields. *Physics of Plasmas*, 11:3472, 2004.

[55] U. Shumlak and J. Loverich. Approximate riemann solver for the two-fluid plasma model. *Journal of Computational Physics*, 187(2):620–638, 2003.

[56] G.A. Sod. A survey of several finite difference methods for systems of nonlinear hyperbolic conservation laws. *Journal of Computational Physics*, 27(1):1–31, 1978.

[57] J.P. Squire, C.S. Olsen, F.R.C. Díaz, L.D. Cassady, B.W. Longmier, M.G. Ballenger, M.D. Carter, T.W. Glover, and G.E. McCaskill. Vasimr vx-200 operation at 200 kw and plume measurements: Future plans and an iss ep test platform. 2011.

[58] B. Srinivasan. Numerical methods for 3-dimensional magnetic confinement configurations using two-fluid plasma equations. Master's thesis, University of Washington: U.S.A., 2010.

[59] G.W. Sutton and A. Sherman. *Engineering Magnetohydrodynamics*. McGraw-Hill Book Company, New York, 1965.

[60] K. Terasaka, S. Yoshimura, K. Ogiwara, M. Aramaki, and MY Tanaka. Experimental studies on ion acceleration and stream line detachment in a diverging magnetic field. *Physics of Plasmas*, 17:072106, 2010.

[61] G. Tóth. The constraint in shock-capturing magnetohydrodynamics codes. *Journal of Computational Physics*, 161(2):605–652, 2000.

[62] P.J. Turchi, P.G. Mikellides, P. Gessini, and R.A. Gerwin. Numerical simulation of magnetic nozzle flow for nuclear fusion space propulsion. AIAA-99-2701, Los Angeles, CA, 1999.

[63] M.D. West, C. Charles, and R.W. Boswell. Testing a helicon double layer thruster immersed in a space-simulation chamber. *Journal of Propulsion and Power*, 24(1):134–141, 2008.

[64] R. Winglee, T. Ziemba, L. Giersch, J. Prager, J. Carscadden, and BR Roberson. Simulation and laboratory validation of magnetic nozzle effects for the high power helicon thruster. *Physics of Plasmas*, 14:063501, 2007.

[65] K. Xu, L. Martinelli, and A. Jameson. Gas-kinetic finite volume methods, flux-vector splitting, and artificial diffusion. *Journal of Computational Physics*, 120(1):48–65, 1995.

[66] T.M. York, P. Mikellides, and B.A. Jacoby. Plasma flow processes within magnetic nozzle configurations. AIAA-89-2711, Monterey,CA, 1989.

APPENDIX A. MAGNETIC NOZZLE EXPERIMENT REGIMES

	Experiments						
	VASIMR[4]	**VASIMR(DS)**	**HPH**[64]	**DDEX**[20]	**HDLT**[63]	**KAH**[38]	**MPDA**[31]
Inputs							
Number Density ($\#/cm^3$)	1.00E+13	1.00E+12	2.00E+13	1.00E+13	1.00E+11	6.00E+13	1.00E+14
Density (kg/m^3)	6.63E-07	6.62E-08	5.31E-07	6.64E-08	6.64E-09	3.98E-06	6.64E-07
T_i (eV)	5.00E+01	5.00E+00	6.58E+00	4.00E+00	2.00E-01	1.00E-01	1.50E+01
T_e (eV)	6.00E+00	5.00E+00	6.58E+00	4.00E+00	5.50E+00	5.00E-01	9.90E+00
Flow Velocity (m/s)	2.00E+04	2.00E+04	6.40E+03	1.00E+04	8.70E+03	1.70E+03	3.00E+04
Characteristic Length (m)	1.00E+00	1.00E+00	4.00E-01	5.00E-01	1.50E-02	4.00E-02	4.00E-02
B (Gauss)	5.50E+02	8.00E+01	2.00E+02	7.00E+02	1.38E+02	1.00E+03	1.00E+03
Plasma Parameters							
Debye Length (m)	5.76E-06	1.66E-05	4.26E-06	4.70E-06	5.51E-05	6.78E-07	2.34E-06
Particles in Debye Sphere (#)	1.91E+03	4.59E+03	1.55E+03	1.04E+03	1.67E+04	1.87E+01	1.28E+03
Plasma Criteria	5.76E-06	1.66E-05	1.07E-05	9.40E-06	3.67E-03	1.70E-05	5.84E-05
Velocities							
Ion Thermal (m/s)	1.10E+04	3.48E+03	6.30E+03	9.83E+03	6.95E+02	4.92E+02	1.90E+04
Electron Thermal (m/s)	1.03E+06	9.37E+05	1.07E+06	8.38E+05	9.83E+05	2.96E+05	1.32E+06
Alfvén (m/s)	6.02E+04	2.77E+04	2.45E+04	2.42E+05	1.51E+05	4.47E+04	1.09E+05
Ion Sound (m/s)	4.92E+03	4.49E+03	8.13E+03	1.27E+04	4.71E+03	1.42E+03	2.00E+04
Frequencies							
Ion Cyclotron ($1/s$)	1.32E+05	1.93E+04	1.20E+05	1.68E+06	3.32E+04	2.41E+05	2.41E+06
Electron Cyclotron ($1/s$)	9.68E+09	1.41E+09	3.52E+09	1.23E+10	2.43E+09	1.76E+10	1.76E+10
Ion Collision ($1/s$)	2.92E+03	7.68E+03	1.45E+05	2.94E+05	6.46E+04	4.83E+07	4.40E+05
Electron Collision ($1/s$)	2.12E+07	3.02E+06	3.63E+07	3.68E+07	2.91E+05	3.01E+09	9.50E+07
Times and Lengths							
Ion Collision Time (s)	3.43E-04	1.31E-04	6.91E-06	3.41E-06	1.55E-05	2.08E-08	2.28E-06
Electron Collision Time (s)	4.72E-08	3.32E-07	2.76E-08	2.72E-08	3.44E-06	3.32E-10	1.04E-08
Residence Time (s)	5.00E-05	5.00E-05	6.25E-05	5.00E-05	1.72E-06	2.35E-05	1.33E-06
Ion Mean Free Path (m)	3.77E+00	4.55E-01	4.35E-02	3.35E-02	1.08E-02	1.02E-05	4.34E-02
Electron Mean Free Path (m)	4.84E-02	3.11E-01	2.97E-02	2.28E-02	3.38E+00	9.85E-05	1.37E-02
Ion Larmor Radius (m)	8.30E-02	1.80E-01	5.24E-02	5.83E-03	2.09E-02	2.04E-03	7.91E-03
Electron Larmor Radius (m)	1.06E-04	6.66E-04	3.05E-04	6.80E-05	4.05E-04	1.68E-05	7.49E-05
Ion Braginskii Hybrid (m)	5.60E-01	2.86E-01	4.77E-02	1.40E-02	1.50E-02	1.44E-04	1.85E-02
Electron Braginskii Hybrid (m)	2.27E-03	1.44E-02	3.01E-03	1.25E-03	3.70E-02	4.07E-05	1.01E-03
Non-Dimensional Numbers							
Reynolds Number	5.03E-01	1.32E+01	9.74E+00	1.58E+01	1.81E+01	1.41E+04	1.52E+00
Magnetic Reynolds Number	6.54E+02	4.60E+02	9.79E+01	9.43E+01	3.11E+00	9.40E-02	8.63E+01
Alfvén Mach	3.32E-01	7.22E-01	2.62E-01	4.13E-02	5.76E-02	3.80E-02	2.74E-01
Mach	4.07E+00	4.45E+00	7.87E-01	7.88E-01	1.85E+00	1.20E+00	1.50E+00
Velocity Beta	5.76E-01	8.49E-01	5.11E-01	2.03E-01	2.40E-01	1.95E-01	5.24E-01
Pressure Beta	6.66E-02	3.15E-02	1.33E-01	3.29E-03	4.23E-05	2.42E-04	6.05E-02
Hall and Collision Numbers							
Ion Hall Collision	4.53E+01	2.51E+00	8.29E-01	5.73E+00	5.15E-01	4.99E-03	5.47E+00
Electron Hall Collision	4.56E+02	4.66E+02	9.70E+01	3.35E+02	8.35E+03	5.84E+00	1.85E+02
Ion Cyclotron/Residence Freq.	6.62E+00	9.65E-01	7.52E+00	8.42E+01	5.73E-02	5.67E+00	3.21E+00
Electron Cyclotron/Residence Freq.	4.84E+05	7.04E+04	2.20E+05	6.16E+05	4.19E+03	4.14E+05	2.35E+04
Ion Residence/Collision Freq.	6.84E+00	2.60E+00	1.10E-01	6.80E-02	8.99E+00	8.81E-04	1.71E+00
Electron Residence/Collision Freq.	9.42E-04	6.63E-03	4.41E-04	5.44E-04	1.99E+00	1.41E-05	7.89E-03
Knudsen Numbers							
Ion Knudsen #	3.77E+00	4.55E-01	1.09E-01	6.70E-02	7.20E-01	2.55E-04	1.09E+00
Electron Knudsen #	4.84E-02	3.11E-01	7.41E-02	4.56E-02	2.25E+02	2.46E-03	3.42E-01
Ion Braginskii	5.60E-01	2.86E-01	1.19E-01	2.80E-02	1.00E+00	3.61E-03	4.63E-01
Electron Braginskii	2.27E-03	1.44E-02	7.52E-03	2.49E-03	2.47E+00	1.02E-03	2.53E-02
Ion Strong Field	8.30E-02	1.80E-01	1.31E-01	1.17E-02	1.39E+00	5.10E-02	1.98E-01
Electron Strong Field	1.06E-04	6.66E-04	7.63E-04	1.36E-04	2.70E-02	4.21E-04	1.87E-03
Transport Properties							
Dynamic Viscosity ($kg/(ms)$)	2.64E-02	1.00E-04	1.40E-04	2.10E-05	4.77E-08	1.92E-08	5.26E-04
Dynamic Viscosity $\perp$ ($kg/(ms)$)	3.98E-06	4.93E-06	6.31E-05	1.98E-07	5.59E-08	2.39E-04	5.45E-06
Kinematic Viscosity (m^2/s)	3.97E+04	1.52E+03	2.63E+02	3.16E+02	7.20E+00	4.81E-03	7.92E+02
Electrical Conductivity (S/m)	2.60E+04	1.83E+04	3.04E+04	1.50E+04	1.90E+04	1.10E+03	5.73E+04
Thermal Conductivity ($W/(mK)$)	1.36E+00	7.60E-01	2.43E+01	3.06E-01	2.71E-03	2.91E+01	9.74E+00

Table A.1: Magnetic nozzle experiments